Precise Measurement of the Nuclear Dependence of Structure Functions in Light Nuclei

by

Jason Seely

Submitted to the Department of Physics
in partial fulfillment of the requirements for the degree of

Doctor of Philosophy in Physics

at the

MASSACHUSETTS INSTITUTE OF TECHNOLOGY

Sept 2006

Author .....
Department of Physics
June 20, 2006

Certified by .....
Haiyan Gao
Associate Professor of Physics
Thesis Supervisor

Accepted by .....
Thomas J. Greytak
Professor, Associate Department Head for Education

Precise Measurement of the Nuclear Dependence of Structure Functions in Light Nuclei

by

Jason Seely

Submitted to the Department of Physics
on June 20, 2006, in partial fulfillment of the
requirements for the degree of
Doctor of Philosophy in Physics

Abstract

The EMC effect has been with us for over 20 years. During this time, the nuclear dependence of the structure functions, and therefore the underlying quark distributions, has been studied with much success. However, the bulk of the experimental effort has been to measure the effect in heavy nuclei where it has the same x_{Bj} dependence and differs only in magnitude. Calculations predict large differences in both the magnitude and x_{Bj}-dependence of the EMC effect in ^{3}He and ^{4}He and precise measurements of the EMC effect in these nuclei could be used to distinguish between existing models. E03-103 measured the inclusive electron scattering cross-section on ^{1}H, ^{2}H, ^{3}He, and ^{4}He, as well as the heavier targets Be, C, Cu, and Au. This thesis describes the experiment in detail and presents results for ^{3}He, ^{4}He, and carbon. These data provide the first measurement of the EMC effect in ^{3}He above $x_{Bj} > 0.4$, and improve upon the existing measurement of the effect in ^{4}He.

Thesis Supervisor: Haiyan Gao
Title: Associate Professor of Physics

Acknowledgments

I have always had the good fortune to be surrounded by a variety of intelligent, talented and spirited individuals. My friends and family have always motivated me to work and play hard and I've always tried my best to follow their good examples. Any success I have had is owed in large part to these people, and I am happy to have an opportunity to thank a few of them here.

I would like to start by thanking my thesis advisor Haiyan Gao. Haiyan always has her students' best interests at heart and never hesitates to provide opportunities and support to help them succeed. In my case, this support has taken various forms at various times. In the beginning it meant providing quality research projects and the independence necessary to learn from them. Of course it also meant giving patient guidance when I made mistakes. Later it meant being supportive when I decided to change thesis topics after four years. Throughout this time, Haiyan was always looking for opportunities to help me grow as a student and as a researcher. She provided encouragement and support for travel to conferences around the world and countless trips to Jefferson Lab for analysis meetings. She provided a supportive environment where I was able to develop as a student and prepare for life after graduate school. I appreciate everything Haiyan has done and have enjoyed working with her during my time at MIT.

Next I would like to thank the members of my thesis committee, Bill Donnelly and Bob Redwine. Professor Donnelly has always been very generous with his time and I have appreciated our physics discussions, and his understanding when I changed thesis topics mid-stride. I am grateful to Professor Redwine for agreeing to sit on my committee at such short notice and for his careful reading of this manuscript and thoughtful comments.

I would like to thank John Arrington and Dave Gaskell for giving me the opportunity to work with them on the experiment presented here. Their enthusiasm for physics, and their enjoyment of the work helped put the fun back in physics. John was always extremely generous with his time and I appreciate all the detailed physics

discussions we had. I am especially grateful for the opportunity I had to travel to Argonne to work one-on-one with John on the analysis. By any measure, including sheer number of donuts consumed per shift, Dave is the best run-coordinator a shift crew could ever hope for. More importantly, however, work in Hall C would grind to a halt without him. All experiments performed in, and all students that come out of Hall C go through him first. His knowledge and expertise are rivaled only by his enthusiasm and his generosity. Dave somehow always had time to answer my questions and I always enjoyed talking about physics and analysis with him. I appreciate the encouragement he's given and the sense of responsibility he instilled in me during the two years we have known each other. By his own example, he made me want to work harder to get things right.

This experiment would not have been a success without the work of Nadia Fomin and Aji Daniel. Their work has been invaluable to the collaboration, and, at times, their patience with me has been amazing. Thank you both for all your help over the past two years. A special thanks to Nadia who has made this past two years a lot more fun. She reminded me that even if the day starts and ends with work, life does not. Our analysis also benefitted greatly from the help of Tanja Horn. Although she was deeply involved in her own analysis, Tanja was always available to answer our questions on software, analysis, physics, math, or whatever. Very often she would join in *our* analysis effort just for the fun of solving a problem. All of her help was greatly appreciated, as were all the free table-tennis lessons.

I would like to thank the LNS Staff, past and present. Strolling down the fifth floor hallway of building 26 was always a sure way to brighten my day. Thanks to Jack, Jerry, Billy, Ken, Sandy, Pierre, Elsye, and Steve for making the day-to-day (and night-to-night) grind a little more human. Special thanks to Sandy Tenorio, Sheela Hulsoor and Joanne Gregory who always went out of their way to take care of all the students.

Having worked at both Bates Laboratory and Jefferson Laboratory, I was continually amazed that physics could actually be done at these facilities. The number of systems that all have to work properly at the same time is ridiculous. The fact that

things work so well, and so regularly, is a testament to the skills and dedication of the people that make them work. I would like to acknowledge the hard work and dedication of the scientific, engineering, and technical staffs at both laboratories. In particular, I would like to thank Jim Kelsey, Ernie Ihloff and Karen Dow at Bates for their support on the various projects I worked on, as well as their advice and encouragement in and out of the lab. I would also like to thank Steve Wood at Jefferson Lab for his assistance with the Hall C software, especially the code used to produce ROOT trees so that I could do my analysis in `C++`. I would also like to thank the dozens of professors and students who took shifts or contributed in other ways to make E03-103 a success.

I am very fortunate to have an incredibly intelligent and caring family. Although they are scattered all over the country, I keep them with me always. I want to thank my brother, Nathan, who has always amazed me his natural intelligence. I want to thank my sister, Stacy, who has inspired me with her enormous heart. I look forward to the time when the three of us can be as close, geographically, as I feel we have grown over the past few years. I would like to thank my Dad, who has always been there with support and an encouraging word when I needed it. With a little luck, someday I'll beat him at chess again. I am humbled at the prospect of trying to thank my Mom for everything she has meant to me over the years. There is no way to adequately express my feelings. I keep her in my heart and in my thoughts at all times, and I everything I do in life is meant as a gift to her. I hope that someday I can repay her for all that she has done and that someday she will understand how important she is to me.

I would like to express my thanks to all my aunts, uncles, cousins and grandparents for their constant encouragement. In particular, I want to thank my Aunt Bev for being like a second mother to me. I would also like to give a special thanks to my Uncle Casey for his amazing spirit and sage advice over the past few years.

I feel extremely lucky to have been welcomed into my wife's family. Having a second set of parents, aunts, uncles and grandparents has been wonderful, and I thank all the Keatons and Konkels for their love and support. I am grateful to have

become so close with my second set of parents, Jeff and Julie Keaton, and I thank them for believing in me and supporting me as if I were one of their own.

I had the good fortune of working with some of the most interesting and intelligent students in the field on the BLAST project at Bates. Those years were special, and only those of us who were students at that time can probably appreciate just what it was like. I want to express my heartfelt thanks and best wishes to all the BLAST students for teaching me so much about physics and life outside of physics. I wish everyone the very best as they leave graduate school behind and move on to the next stages of their lives. Thanks to Tavi Filoti, Adrian Sindile, Yuan Xiao, Vitaliy Ziskin, Eugene Geis and Sean Stave (honorary BLAST student). Thanks to Aaron Maschinot for all the help on analysis, coding, homework, and for being the first to go through the job search. Thanks to Chi Xiang for always wearing a smile. Thanks to Adam DeGrush for Beckett, Ashbury, and the depth and breadth of our conversations. Thanks to Nikolas Meitanis for basketball, Bergman, Cassavetes, and all the talks about film, chess, and many other topics. Thanks to Pete Karpius for all the fun away from Bates, and for letting a little of your good spirits and enthusiasm rub off on those around you. Two other students, Chris Crawford and Ben Clasie, deserve special thanks. I considered Chris to be my unofficial mentor during my time at MIT. I quickly learned that he was the smartest, most patient and most generous person I have ever had the pleasure of working with. It took me a little longer to learn that he is always right, but I learned it eventually. I am grateful for everything he taught me about physics and programming, but more importantly, about life and family. I'm also grateful for all the late night church ball. I have worked with Ben for the duration of our six years at MIT. From BLAST and the BATs, to the Laser Driven Target, to Pion Color Transparency and the EMC Effect, I am grateful for all the time we have spent together. I learned from Ben's example that details *do* matter, and that sometimes 'good enough' is not good enough. I also learned the value of persistence, and what it means to finish the job. During the time I have known him, Ben has worked hard enough to have earned at least two Ph.D.'s, and it has been my pleasure to work with him.

Throughout my life, whatever friends I've had have been an extremely valuable source of inspiration and I would like to express my appreciation to a few of them here. Thanks and love to Mike Campbell and Matt Majers for all the skateboarding, the long conversations, and the inspiration over the years. Their lives and their achievements have always motivated me to work harder. Thanks to Jeff Reifenberger and Chris Goldman, both of whom I met at the University of Arizona. I learned so much about physics and real life from both of them. Thanks to Chris for letting me ride his coattails for so long. I'll always remember the potato cannon and EEPP lab fun. I'm happy to know that we will be coworkers again, and that this time there will be no Unistrut around. Next I'd like to thank the many friends who made my time in Cambridge more fun. Thanks to Brad Plaster for all the study sessions, talks, and food truck lunches during our time together. Thanks to Gianpaolo Carosi for all the movies I never went to, and all the parties I did. A huge thanks to Christophe Perez for getting me back on my skateboard even when I should have been working. And a very special thanks is owed to my Little Brother, Colain Nelson, for all the fun we've had over the past two years playing basketball and racing go-karts. His advice to me before my thesis defense was crucial and helped me stay focused and undaunted.

Next I want to try to express my love and gratitude to Micah Boyd and Karin Antoni. I have always been impressed by each of them as individuals, and by the two of them as a couple. It is an extremely rare thing to find two people who are so intelligent, gifted, and strong-willed, and who actually get along. It seems that they have each met their match. Jen and I feel so grateful to have had the opportunity to get to know them so well. It would be impossible to express what they have meant to us after all that we have shared. It has been wonderful to have two kindred spirits with whom we could struggle during these past few years. The regular dinners, and occasional weekends, and the constant laughs have put some normalcy and humanity back into the limbo of graduate school. We have all grown so close over the years, that it feels more like we're splitting up a family than moving away from friends. However, I take comfort knowing that we will meet again on the other side of the country; and I look forward to picking up, and throwing down, where we left off.

Finally, I would like to thank my wife, Jen, for her love and support during the past six years; and for challenging me, by her own example, to keep growing, learning and pushing myself. It is an interesting coincidence that I write these words on August 22nd, 2006. That makes it fifteen years, almost to the day, from the day that Jen and I first met. So the closing of this latest chapter marks the anniversary of that most important of days. This is fitting as it reminds me of two things. The first is that everything I do in my life starts and ends with Jen. The second is that nothing I have done, or will ever do, will ever be as important as the relationship that she and I have built. Graduate school has been difficult, but it is only one of many chapters in the amazing story of our life together. No words can express the love I have for her, nor the gratitude I feel for all that she has done over these fifteen years. All I can say is that my life began when we met, and that everything else was prologue. So, as humble as it is, I dedicate this thesis to my wife, Jen, as a thanks for the past, and as a gesture of hope for the future. We have come a long way together, but there is so much farther to go.

Contents

List of Figures

List of Tables

Chapter 1

Introduction

Nuclear and particle physics is the study of the fundamental nature of matter. More specifically, they are the study of the structure and dynamics of the fundamental constituents of atoms. At present, the most basic constituents are the quarks and gluons that comprise the hadrons (protons, neutrons, pions, etc.) in the nucleus, and the electrons that surround the nucleus to form atoms. The process of discovery often works in fits and starts. Some new phenomenon is discovered, and this is followed by a flurry of experiments to understand the phenomenon. As theory and technology improve, this flurry yields to a phase of precision measurements where the finer details of the phenomenon are mapped out. Occasionally the two phases meet and something new is discovered during the phase of precision measurement. This was the case with the discovery by the European Muon Collaboration (EMC) in 1983 that the structure of nucleons is modified by the nuclear medium [1]. The EMC collaboration had set out to make a precise measurement of nucleon structure, but instead found that the structure exhibited in iron was different than that found in deuterium. This effect was dubbed 'The EMC Effect' and tremendous experimental and theoretical efforts have since been expended in an effort to understand the effect. These efforts have paid off as the gross features the EMC effect are very well understood for heavy nuclei. However, data on the lightest nuclei have remained conspicuously scarce from the world dataset. Light nuclei, $A \leq 4$, provide a crucial link between the free nucleon structure and the structure of heavy nuclei. A measurement of the EMC

effect on these nuclei is, therefore, of utmost importance to complete the picture of the evolution of nuclear structure. It is in that spirit that we present a precision measurement of the ratio of structure functions in ^{3}He and ^{4}He.

This thesis describes a precise measurement of the EMC effect in ^{3}He and ^{4}He, which was made at Jefferson Laboratory in an effort to complete the picture of the evolution of the structure functions. Since the majority of nuclear or particle physics experiments involve scattering particles from one another, we begin with a technical discussion of inclusive scattering from nuclei. This discussion will illuminate the basic features necessary to understand the EMC effect and its importance in nuclear physics, and will include important concepts such as nuclear structure functions, their scaling behavior, and the EMC effect. This is followed in Chapter 2 by a historical overview of the work done to understand the EMC effect. We will then be prepared to discuss the details of the experiment and analysis of the work presented here.

1.1 Scattering

Over the course of the past century, physicists have worked diligently to uncover the details of the building blocks of matter. The history of atomic and nuclear physics is extremely rich and comprised of a great variety of personalities and experiments. A common thread running through that history is the use of particle scattering as a tool to probe the internal structure of atoms and nuclei. Most of what we know about nuclei is the result of scattering experiments.

A particularly famous example is the work of Rutherford, who scattered alpha particles (Helium nuclei) from a gold foil and discovered that the atom contains a hard, small, and positively charged core: the nucleus. Soon after, the neutron was discovered in scattering experiments and the basic picture of the atom, which holds to this day, was complete. We now know that the atom consists of a compact and massive nucleus, composed of protons and neutrons (collectively referred to as nucleons), surrounded by a cloud of electrons. The nature of the nucleon-nucleon interaction, as well as the shell structure of the nucleus, were illuminated in experiments scattering

protons and neutrons from nuclei.

Leptonic probes (electrons and muons) have been used to map out both the coarse features of nuclei and nucleons, such as their charge and magnetism distributions, and the finer details such as the spin and momentum distributions of the particles (partons) inside the nucleon. Electron scattering remains one of the most valuable techniques for studying the nucleus and its components. For example, new techniques use polarized beams and targets to access small amplitude processes. But unpolarized inclusive scattering remains the workhorse of electron scattering and still holds an important place in the field as more precise measurements are being made. We turn now to a discussion of inclusive scattering as part of the background for our study of the EMC effect.

1.1.1 Lepton Scattering from Hadrons

Leptons make ideal probes for studying nuclear structure. Since electrons and muons have no internal structure of their own, the extraction of the structure of the target particle from scattering data is less complicated than for hadronic probes (pions, nucleons, etc.) Furthermore, electrons and muons do not participate in strong interactions, and so the scattering can be treated via Quantum Electrodynamics (QED). The relatively weak coupling of leptons to the electromagnetic field is given by the fine-structure constant, $\alpha \approx 1/137$. Because α is small, the scattering process is well modeled by the exchange of a single virtual photon (the Born approximation), and can be treated perturbatively. In the Born picture, illustrated in Fig. 1-1, an electron and nucleus scatter from each other by exchanging a single virtual photon. We label the incoming electron's four-momentum K, the outgoing electron four-momentum K', the target nucleus' four-momentum P, the virtual photon's four-momentum $q = K - K'$. The four momentum, W, of the final hadronic state, called the invariant mass, is known from the electron and target four momenta: $W = P + q = P + K - K'$. To calculate the cross section for a given process, one must first calculate the probability for the process to occur. This probability is given by square of the Lorentz Invariant Matrix Element, which may be computed using the Feynman diagram for the process.

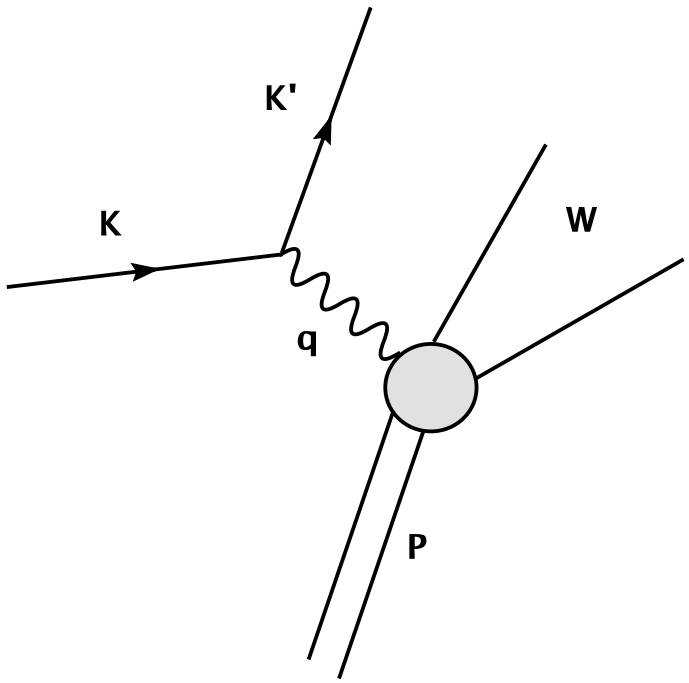

Figure 1-1: Feynman diagram for Inclusive electron scattering. The incoming electron has four-momentum K, the outgoing electron has four-momentum K', the target has four-momentum P and the final hadronic state (undetected) has four-momentum W.

When calculating the squared matrix element for a scattering process, one typically starts with the currents representing the target and probe particles. For example, the lepton tensor can be calculated from the lepton current using the four vectors of the incoming (K) and outgoing (K') electrons:

$$\eta_{\mu\nu} = \frac{1}{2m_e^2}\left(K_\mu K'_\nu + K'_\mu K_\nu - g_{\mu\nu}(K \cdot K' - m_e^2)\right), \tag{1.1}$$

where m_e is the electron mass (0.511 MeV), and we work in the basis where $g_{00} = 1$ and $g_{ij} = -1$ for $i, j = 1, 2, 3$. However, in inclusive scattering, the final hadronic state is undetermined and it is not possible to write down the hadronic current explicitly, so we must construct the hadronic tensor from the available 4-vectors.

To construct the hadron tensor, we use the fact that there are only two linearly independent 4-vectors available at the hadron-photon vertex. Any linearly independent combination of the three available 4-vectors will suffice. The three available vectors are the four-momentum of the virtual photon, q, and the target and scattered hadron

momenta, P_i and P_f, respectively. For convenience, we choose to build the hadron tensor using q and a new four-vector, V, which has the form, [2]

$$V^\mu \equiv \frac{1}{M}\left\{P_i^\mu - \left(\frac{q\cdot P_i}{q^2}\right)q^\mu\right\}. \tag{1.2}$$

Note that $q \cdot V = 0$, satisfying current-conservation. Using these two 4-vectors, the most general second-rank tensor that satisfies Lorentz covariance, current conservation and parity conservation has the form:

$$W^{\mu\nu} = -W_1\left(g^{\mu\nu} - \frac{q^\mu q^\nu}{q^2}\right) + W_2 V^\mu V^\nu. \tag{1.3}$$

Here W_1 and W_2 are the structure functions that depend on two kinematic variables, usually chosen to be $\nu = E - E'$ and $Q^2 = -q^2 \approx 4EE'\sin^2(\theta/2)$. These functions parameterize our ignorance of the underlying structure of the nucleon. The tensor above is applicable only for unpolarized, parity-conserving scattering. If the beam or target is polarized or parity-violating processes are relevant, then it is necessary to include other structure functions. The most general tensor that satisfies lorentz-invariance and current conservation consists of five independent structure functions.

The lepton and hadron tensors may now be used to form the Lorentz-Invariant Matrix Element for the inclusive scattering process. The squared matrix element is proportional to the contraction of the two tensors

$$|M|^2 \sim \eta_{\mu\nu}W^{\mu\nu}, \tag{1.4}$$

and the cross section is proportional to this squared matrix element. Upon contracting the tensors we may write the inclusive lepton-nucleus scattering cross section in the laboratory frame as

$$\frac{d^2\sigma}{d\Omega dE'} = \frac{4\alpha^2 E'^2}{Q^4}\left[2W_1(\nu,Q^2)\sin^2\frac{\theta}{2} + W_2(\nu,Q^2)\cos^2\frac{\theta}{2}\right], \tag{1.5}$$

where all terms of order $m_e^2/\vec{k}\cdot\vec{k}'$ have been neglected.

The shape of the structure functions, and therefore the cross section, depends on the kinematic regime in question. The nuclear cross section has a rich structure in energy and four-momentum transfer. At low energies, the photon scatters coherently from all nucleons in the nucleus (nuclear elastic scattering), or may raise the nucleus to an excited state (nuclear inelastic scattering). At moderate energy transfer the scattering is dominated by quasielastic scattering, where the photon scatters coherently from a single nucleon in the nucleus. As energy transfer is increased, the photon can excite resonances in the nucleon. However, at very high four-momentum transfers, the virtual photon begins to scatter from the individual quarks inside the nucleon. This is called Deep Inelastic Scattering (DIS) and is one of the most useful tools for studying the quark substructure of the nucleon. The most famous result from DIS is surely the confirmation, at SLAC [3, 4], that protons and neutrons are composed of more fundamental particles, now known to be quarks and gluons. Since that pioneering work, DIS has been used to study the momentum and spin distributions of quarks and gluons in great detail. The present work is a measurement of the nuclear dependence of the inclusive electron scattering structure functions in deep inelastic scattering. The fact that the structure functions are different in different nuclei is a relatively new and important chapter in the larger story of DIS. We will therefore spend the rest of this chapter examining some important properties of the DIS structure functions.

1.2 Björken Scaling

In this section we will explore one of the most important features of the DIS structure functions: Björken Scaling. This is the phenomenon that as the energy and four-momentum transfer are increased the two-dimensional structure functions evolve into functions of one kinematic variable only. This can be understood in a relatively simple picture. Recall that the scattering of a point particle from another point particle is

described by the Mott cross section

$$\frac{d\sigma(\theta)}{d\Omega} = \frac{(\mathrm{Z}\alpha)^2 \cos^2 \frac{\theta}{2}}{4E^2 \sin^4 \frac{\theta}{2}}, \tag{1.6}$$

where E is the energy of the incoming particle, and Ze is the charge of the target particle (we have assumed that the incoming particle has charge e). The cross section is completely determined by the incoming energies of the particles and the angle of the scattered particle. In DIS we scatter electrons from the quarks in the nucleon. Since electrons and quarks are both point-like particles, in the limit of scattering from a single free quark, the scattering must depend only on one kinematic variable. The complication, of course, is that quarks are *not* free, nor are they at rest in the nucleon. However, at high enough energies, the quarks can be regarded as quasi-free, and the scattering process will be determined by one kinematic variable. Since the quarks move around in the nucleon, the cross section at a given angle will not take a single value as in Eq. 1.6, but will have a distribution of energies which represents the way in which the momentum is distributed among the quarks inside the nucleon. In a sense, the total cross section is a sum over many Mott-like cross sections corresponding to different initial momenta of the target quarks. The distribution in energy indicates the momentum distribution. Therefore we can write the final cross section at a given scattering angle in terms of this momentum distribution. With this picture in mind, we turn now to deriving the result of Björken scaling and express the cross section in terms of a new variable as described above. Note of course that this simple picture breaks down as Q^2 decreases. The scattering takes place via a virtual photon, which has a finite resolving power that goes as $1/|\vec{q}|$. As Q^2 decreases the virtual photon scatters from a larger area inside the nucleon and therefore off groups of quarks, rather than individual quarks. This picture will be useful when we talk about violations to Björken Scaling that occur at low Q^2.

We start by considering the general form of the cross section for scattering an

electron off a structureless spin-$\frac{1}{2}$ particle (of charge e):

$$\frac{d^2\sigma}{d\Omega dE'} = \frac{4\alpha^2 E'^2}{Q^4}\left[\frac{Q^2}{2m^2}\sin^2\frac{\theta}{2} + \cos^2\frac{\theta}{2}\right]\delta(\nu - \frac{Q^2}{2m^2}), \tag{1.7}$$

where m is the mass of the point-like particle. This equation reduces to the Mott cross section in Eq. 1.6. Using the identity $\delta(ax) = \delta(x)/|a|$, the cross section can be rewritten

$$\frac{d^2\sigma}{d\Omega dE'} = \frac{4\alpha^2 E'^2}{Q^4}\left[\frac{Q^2}{2m^2\nu}\sin^2\frac{\theta}{2} + \frac{1}{\nu}\cos^2\frac{\theta}{2}\right]\delta(1 - \frac{Q^2}{2m\nu}). \tag{1.8}$$

If the nucleon is indeed composed of spin-$\frac{1}{2}$ particles, then as we increase the energy and four-momentum transfer, the measured scattering cross section should eventually take this form. Comparing this to Eq. 4.1, we note that this statement is the same as saying that the nuclear structure functions will evolve from W_1 and W_2 to the functions

$$mW_1^{point}(\nu, Q^2) \to \frac{Q^2}{2m\nu}\delta\left(1 - \frac{Q^2}{2m\nu}\right), \tag{1.9}$$

and

$$\nu W_2^{point}(\nu, Q^2) \to \delta\left(1 - \frac{Q^2}{2m\nu}\right). \tag{1.10}$$

It is important to make the connection with the Mott cross section here. Although the cross section in Eq. 1.8 depends on two independent kinematic variables (θ and E'), the dependence is fundamentally different from the dependence in Eq. 4.1. In the point-like scattering, the E' distribution at a particular angle is due to the distribution of initial energies of the quarks in the nucleon. So the DIS structure functions represent the distribution of quark momenta inside the nucleon. This description is further enhanced by noting that the point-like version of the structure functions do not dependent on ν and Q^2 independently, but instead, depend on the combination $Q^2/2m\nu$. Since the quarks in the nucleon are confined, their masses are poorly known, and so the combination is normally rescaled to the familiar form $x_{Bj} = Q^2/2M\nu$. In the infinite momentum frame, where the quarks are free, x_{Bj} is the fraction of the nucleon's momentum carried by the struck quark. The phenomenon that the cross section is independent of Q^2 is called 'Björken Scaling' and the observation of Björken

Scaling is how the experimenters at SLAC [3, 4] confirmed the existence of quarks.

The structure functions are often replaced with the functions

$$MW_1^{point}(\nu, Q^2) = F_1(x, Q^2), \tag{1.11}$$

and

$$\nu W_2^{point}(\nu, Q^2) = F_2(x, Q^2), \tag{1.12}$$

which will exhibit the same scaling properties as W_1 and W_2. Writing the cross section in terms of these new structure functions gives

$$\frac{d^2\sigma}{d\Omega dE'} = \frac{4\alpha^2 E'^2}{Q^4}\left[2\frac{F_1}{M}\sin^2\frac{\theta}{2} + \frac{F_2}{\nu}\cos^2\frac{\theta}{2}\right]. \tag{1.13}$$

The structure function F_2 is shown as a function of x_{Bj} and Q^2 in Fig. 1-2. At moderate values of x_{Bj}, the structure function is very flat as a function of Q^2. At large values of x_{Bj} there are significant scaling violations due to resonance scattering. The smaller scaling violations are consistent with the logarithmic violations expected from QCD. Note also that scaling appears to set in at Q^2 values of a few (GeV/c)^2 for the range $0.05 < x_{Bj} < 0.5$, but at large values of x_{Bj}, scaling sets in later, typically around Q^2 of 10 (GeV/c)^2.

1.3 Scaling at Low Q^2 and Bloom-Gilman Duality

Björken Scaling holds exactly in the infinite momentum frame. Björken scaling begins to break down as the energy and four-momentum transfer are reduced. Since one cannot do measurements in the infinite momentum frame, it is important to know how well scaling holds at the finite Q^2 at which a given measurement is made. Since the quasielastic peak and nucleon resonances typically dominate the cross section at moderate Q^2, it is common to choose kinematics such that the invariant mass of the hadronic final state is larger than the masses of the most prominent nucleon resonances. At large W^2 the resonances are washed out and DIS is the dominant

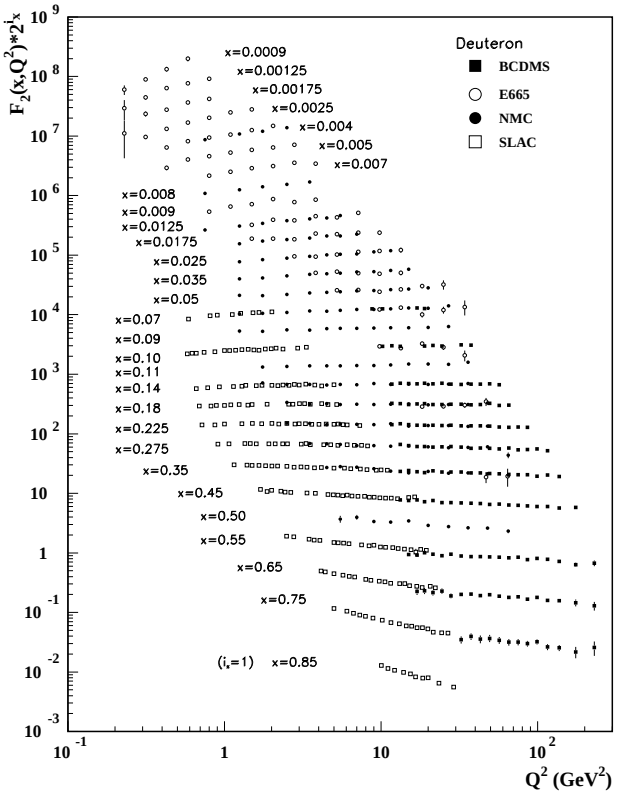

Figure 1-2: Björken Scaling in the inclusive scattering structure function F_2. As Q^2 increases, the structure function section becomes independent of Q^2 for a given value of x_{Bj}. Courtesy of [5].

process. The cuts commonly used to define DIS kinematics are $W^2 > 4(\mathrm{GeV})^2$ and $Q^2 > 4(\mathrm{GeV/c})^2$. This region is safely above the most prominent nucleon resonances and so the cross section is dominated by the DIS cross section. Although it may be that a cut at larger W^2 is necessary as there may still be oscillations about the scaling curve, as described in [6] for pion photoproduction, we will take the cuts above as our working definition for the DIS region in this work. In circumstances where the invariant mass and/or four-momentum transfer are below this value, as in some of the data presented here, care must be taken. Björken scaling is not expected to hold in the resonance region, where the DIS cross section overlaps with the nucleon resonant processes, so the structure functions measured in that region will not be the point-like structure functions of DIS.

However, the inclusive cross section exhibits a remarkable property in the reso-

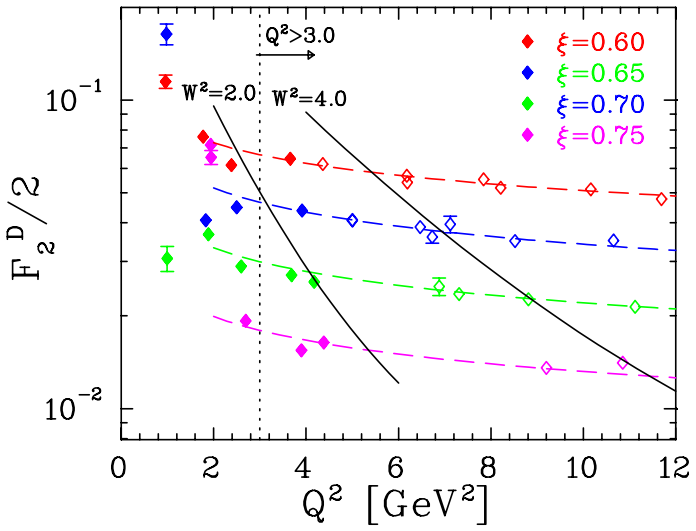

Figure 1-3: $F_2^D/2$ vs. Q^2 at various values of ξ, from [7]. The scaling behavior of the structure function extends well below $W^2 = 4(\mathrm{GeV})^2$ and $Q^2 = 4(\mathrm{GeV/c})^2$.

nance region that makes it possible to observe the DIS cross section. This feature is called Bloom-Gilman duality. Bloom and Gilman observed [8] that the Q^2-averaged value of the structure function in the resonance region is a good approximation to the structure function in DIS kinematics. An excellent conceptual discussion of duality can be found in [9]. Since Björken scaling is only expected in the limit $\nu \to \infty$ and $Q^2 \to \infty$, we do not expect to observe scaling in x_{Bj} at finite Q^2. We are therefore free to examine scaling and duality in any other variable that approaches x_{Bj} in the Björken limit. It was shown by [10] that local duality can be expected from perturbative QCD when the structure functions are examined in terms of variable, ξ, first introduced by Nachtmann [11]

$$\xi = \frac{2x_{Bj}}{1 + \sqrt{1 + \frac{4M^2 x_{Bj}^2}{Q^2}}}. \tag{1.14}$$

It is clear that $\xi \to x_{Bj}$ as $Q^2 \to \infty$ and so the structure functions will exhibit scaling in this variable in DIS kinematics. It is useful to examine scaling in ξ at finite values of Q^2. In fact, the structure functions exhibit scaling in ξ to lower values of Q^2 and W^2 than they do in x_{Bj}. This can be seen in Fig. 1-3 and is, in part, a consequence that ξ partially accounts for the mass effects present at finite Q^2 that are negligible

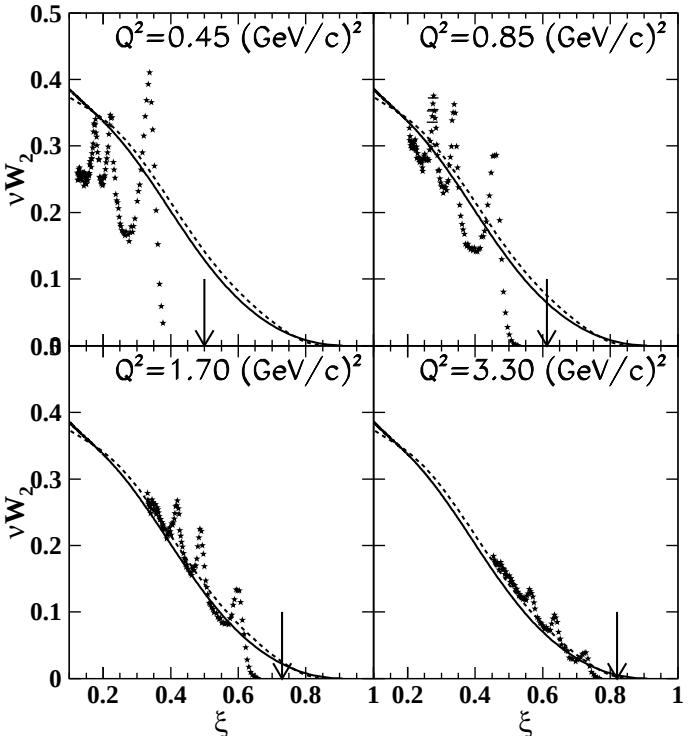

Figure 1-4: The F_2 structure function for the proton as a function of ξ [12]. The stars are the measured cross section on hydrogen, the solid (dashed) line is the NMC fit [13] of the deep inelastic structure function at $Q^2 = 5$ (GeV/c)^2($Q^2 = 5$ (GeV/c)^2). The arrow indicates the location of the elastic peak. The resonance region cross section approaches the DIS cross section at $Q^2 = 1.7$(GeV/c)^2, well below the traditional DIS cutoff.

in the infinite momentum frame. The scaling violations are small even at values of Q^2 and W^2 well below the traditional DIS cutoffs as illustrated in Fig. 1-3. The curves in the figure indicate the logarithmic scaling violations expected from QCD as a consequence of the finite resolution of the probe. It is only below $Q^2 \approx 3$(GeV/c)^2 that the structure function begins to deviate from this logarithmic dependence.

Fig. 1-4 shows cross section data on hydrogen in the resonance region compared to the DIS cross sections. The stars are data on hydrogen and the solid line is a fit to the deep inelastic structure function data at $Q^2 = 5$(GeV/c)^2 from NMC [13]. The resonance structure is clearly visible, and the cross section is very different from the DIS fit (solid line). However, when the cross section data are averaged over Q^2, the resulting cross section should approach the DIS value. Fig. 1-5 shows the resonance cross section and DIS cross sections on hydrogen, deuterium and iron. The most

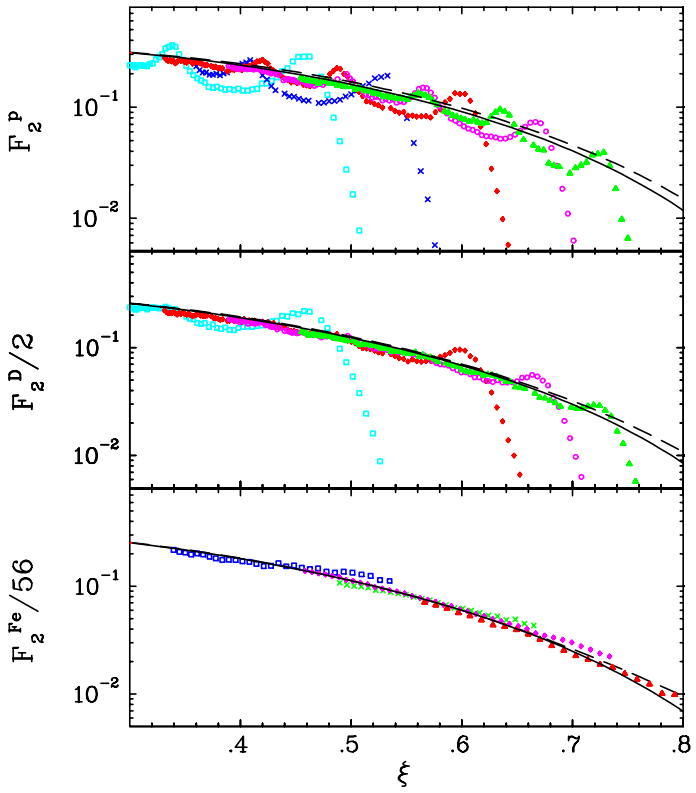

Figure 1-5: Resonance region data and DIS cross sections from [7]. By averaging over Q^2, the DIS limit cross sections can be extracted from the resonance region data.

notable feature here is that as the number of target nucleons increases, the resonance structure gets more washed out. Thus, the cross section is a better approximation to the DIS value for heavy targets than for light targets. This can be understood as an averaging over the cross section performed by the Fermi motion of the nucleons. Duality is an important phenomenon and can be exploited to measure properties of the DIS structure of nucleons when working in non-DIS kinematics. This is the case for some of the data in the present work, and part of the work is to test how well ξ Scaling holds in our non-DIS kinematics.

With the cross section and structure functions in hand, and a basic understanding of Björken- and ξ-Scaling and Duality, we are now prepared to discuss the EMC effect. The next chapter will start with a discussion of how the structure functions for different nuclei can be compared using the nuclear inelastic cross sections. This will be followed by a discussion about the EMC Effect, including the experimental and theoretical efforts that have been expended to understand the effect. This discussion

will serve to motivate the present experiment to measure the EMC effect in ^{3}He and ^{4}He, which is the subject of the remainder of this thesis.

Chapter 2

The EMC Effect

Now that the details of inclusive scattering are understood, we can move on to a detailed discussion of what the EMC effect is and why quality measurements of the structure functions for light nuclei are necessary. This chapter is organized as follows. First we discuss the effect in the context of the scattering results from the last chapter. This discussion is followed by the story of the discovery of the effect and the subsequent experiments performed to elucidate the details of the effect. Next, some important theoretical points are discussed, focusing on the importance of few-body nuclei. These sections provide motivation for making a dedicated measurement of the EMC effect in light nuclei. At that point, we will be adequately prepared to discuss the details of the present experiment.

2.1 Ratio of Nuclear Cross Sections

In the previous chapter, we outlined the inclusive cross section and the nuclear structure functions. In this section we will consider the ratio of cross sections from different nuclei. The cross section per nucleon for a nucleus A is given by Eq. 1.13:

$$\sigma_{\mathrm{A}} = \frac{4\alpha^2 E'^2}{Q^4}\left[2\frac{F_1^{\mathrm{A}}}{M}\sin^2\frac{\theta}{2} + \frac{F_2^{\mathrm{A}}}{\nu}\cos^2\frac{\theta}{2}\right]. \tag{2.1}$$

Then the ratio of the cross section per nucleon for two different nuclei, A_1 and A_2, is:

$$\frac{\sigma_{A_2}}{\sigma_{A_1}} = \frac{F_2^{A_2}}{F_2^{A_1}} \frac{\left[1 + 2\frac{\nu F_1^{A_2}}{M F_2^{A_2}} \tan^2\frac{\theta}{2}\right]}{\left[1 + 2\frac{\nu F_1^{A_1}}{M F_2^{A_1}} \tan^2\frac{\theta}{2}\right]}. \tag{2.2}$$

We can simplify this equation by writing the ratio F_1/F_2 in terms of the ratio, R, of the longitudinal and transverse cross sections

$$R = \frac{\sigma_L}{\sigma_T} = \left(1 + \frac{\nu^2}{Q^2}\right) \frac{M F_2}{\nu F_1} - 1. \tag{2.3}$$

Solving for the ratio of the structure functions gives

$$\frac{\nu F_1}{M F_2} = \frac{1 + \frac{\nu^2}{Q^2}}{R - 1}. \tag{2.4}$$

So the ratio of the structure function depends only on the kinematics under study, and the value of R. Extensive effort has been made to measure R for various nuclei and it has been demonstrated that R is independent of A at the few percent level [1]. Assuming that R is independent of A, the ratio of cross sections reduces to:

$$\frac{\sigma_{A_2}}{\sigma_{A_1}} = \frac{F_2^{A_2}}{F_2^{A_1}}. \tag{2.5}$$

So a measurement of the ratio of the inclusive cross sections on two different nuclei gives the ratio of the F_2 structure functions.

Before the discovery of the EMC effect, it was assumed that the internal structure of the nucleon would be the same for a bound or free nucleon. Thus, it was expected that the ratio in Eq. 2.5 would be equal to one after correcting for "traditional" nuclear effects that were expected to change the cross section. For example, the Fermi motion of the nucleons, pion excess, and nuclear binding all modify the ratio above. In fact, the ratio was very different from one, and showed structure that could not be accounted for by standard nuclear physics effects.

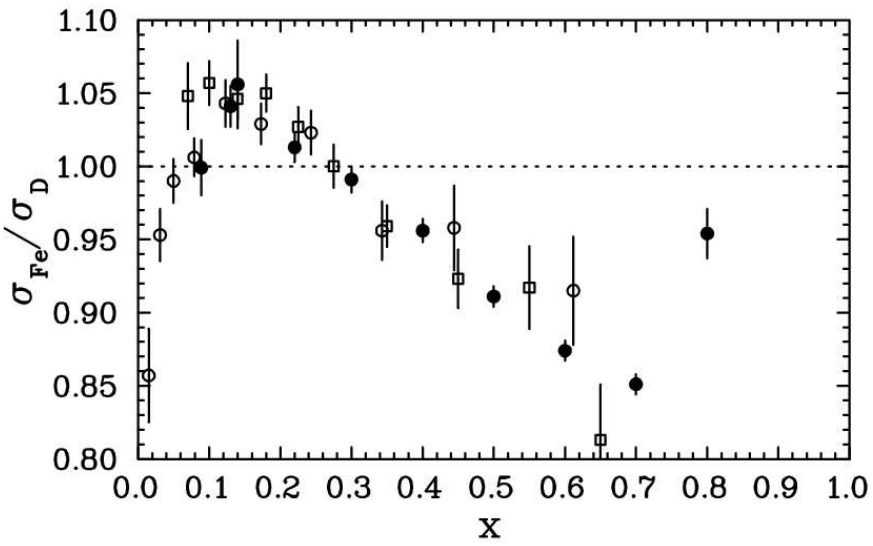

Figure 2-1: Ratio of Fe cross section to that of deuterium, as a function of x_{Bj}. Hollow circles are the EMC [14] data on Copper, solid circles are SLAC [15] data, and squares are BCDMS [16] data. All data have been averaged over Q^2 and corrected for neutron excess.

2.2 History of the EMC Effect

The discovery of the EMC effect is interesting from an historical point of view, since it resulted from technological challenges in DIS experiments at higher and higher energies. The original goal of the EMC collaboration was to measure the DIS lepton-nucleon cross section at large Q^2. The effort to study nucleon structure at for Q^2 led to the use of muons instead of electrons as the probe. This was because the accelerator at CERN was a synchrotron that accelerated protons and energy loss due to radiation is crippling when trying to accelerate electrons to high energies in synchrotrons. The proton beam was used to produce a low intensity secondary beam of muons. The cross sections for muon and electron scattering are identical except for the difference in their mass, which is negligible for both particles in these kinematics. The low particle flux of the muon beam necessitated the use of a denser target material to achieve higher luminosity. Thus, the choice was made to use iron, which made it possible to achieve the desired statistical precision in a reasonable amount of time.

It was expected that the per-nucleon cross section measured on iron would be the

same as that measured on deuterium since the energy scales were much larger than nucleon-nucleon interaction energies. However, when the European Muon Collaboration (EMC) [1] compared their cross section on iron to that of deuterium, they found that the ratio exhibited a striking kinematic dependence, as shown in figure 2-1.

The structure shown in this ratio differed dramatically from what was expected from calculations at the time that included the Fermi-motion of the nucleons inside the nucleus, and was therefore a great surprise. The shape of the ratio has the same general features in all nuclei measured to date. The reduction at moderate x_{Bj} and the enhancement at large x_{Bj} are understood in terms of the Fermi motion of the nucleons and binding energy effects. The reduction at very low x_{Bj} is due to shadowing [17] of the inner partons by outer partons. Although these effects can account for parts of the EMC effect, the entire effect seems to be intractable by standard nuclear physics alone. This observation therefore may stand as the first evidence of a possible modification of the internal structure of nucleons due to the nuclear medium.

2.3 Experimental Overview

Since the discovery of the EMC effect, many dedicated experiments have been performed to map out the precise structure of the nuclear dependence of the structure functions. These experiments were performed around the world over the course of the past twenty years. An overview covering several of the experiments is given below in order to set the stage and motivate the experiment discussed herein. For more detail, the interested reader can see two excellent review articles [18, 19].

2.3.1 EMC Collaboration

The original EMC results [1] from CERN showed that the structure functions have an unexpected kinematic dependence. The original measurement showed a large enhancement between $x_{Bj} \sim 0.1$ (now known as the anti-shadowing region) and $x_{Bj} \sim 0.2$, and a depletion at $x_{Bj} > 0.6$. The EMC collaboration performed subsequent

experiments [14, 20], published in 1988, to study the details of the structure function ratio at low x_{Bj} and low Q^2. They measured the lepton-nucleus inclusive scattering cross section using a muon beam incident on C, Cu, Sn, and deuterium targets in the kinematic range $5 < Q^2 < 35$ (GeV/c)^2, $0.03 < x_{Bj} < 0.7$. They found, for the first time, that there is a depletion of the structure function ratio below $x_{Bj} \approx 0.08$, and that the enhancement between $0.08 < x_{Bj} < 0.2$ was much reduced from the original experiment. These features can be understood as shadowing in the depleted region and anti-shadowing in the enhancement region. One notable detail is that the shadowing was observed at $Q^2 > 5$ (GeV/c)^2. This is an indication that the shadowing is due to the parton distributions, rather than a shadowing of the inner nucleons by the surface nucleons, which is important at $Q^2 < 1$ (GeV/c)^2.

2.3.2 NMC Collaboration

The New Muon Collaboration (NMC) at CERN followed the work of the EMC collaboration with a detailed measurement of the deuterium to proton structure function ratio [21]. They used the CERN muon beam to measure the inclusive cross sections on deuterium and protons. This ratio was used to extract the ratio of the neutron to proton F_2 structure functions F_2^n/F_2^p. Their data covered a broad kinematic range from $0.001 < x_{Bj} < 0.8$, and $0.1 < Q^2 < 145$ (GeV/c)^2. The systematic uncertainty in these measurements was very good: typically 0.5%. No Q^2 dependence was observed in the ratio (beyond the dependence that is compatible with QCD), and there was no apparent shadowing present at low x_{Bj}. The high quality of the data, and the broad kinematic coverage, make this a very important result. Specifically, the ratio F_2^n/F_2^p is an essential piece in forming the isoscalar ratio when comparing non-isoscalar nuclei to deuterium.

2.3.3 SLAC

SLAC set the standard for high precision absolute cross section measurements in lepton scattering. Data from SLAC have been important throughout the history of

the EMC effect, starting soon after the EMC collaboration's first publication, and continuing into the 1990's with their comprehensive study [15] over a large kinematic range for several different targets. The experiments [22] at SLAC benefited from an intense electron beam ($10^{14}e^{-}$/s) with a well-measured energy, and highly-efficient, small-acceptance magnetic spectrometers. The high luminosity and easily variable beam energy allowed for multiple measurements of the same points and thus good control of systematic errors.

Two early experiments [22, 23] at SLAC extracted the ratio of the structure functions on iron and aluminum to deuterium over a kinematic range of $0.075 < x_{Bj} < 0.9$, and $2 < Q^2 < 21$ (GeV/c)^2 from previous measurements of the inclusive cross sections. Their results were consistent with the results from the EMC collaboration which were taken at much higher Q^2. Also, the low-x_{Bj} data were consistent with earlier photoproduction data from [24].

A subsequent experiment [15] made a dedicated measurement of the A dependence of the structure function ratio for several targets (D, ^{4}He, Be, C, Al, Ca, Fe, Ag, and Au) in the kinematic range $0.09 < x_{Bj} < 0.9$, $2 < Q^2 < 12$ (GeV/c)^2. The data from all targets showed the same general shape as earlier data. The range in A that the data covered allowed for a fit to the variation of the structure function ratio as a function of ln(A) at fixed values of x_{Bj}. They fit their data at two x_{Bj} values: $x_{Bj} = 0.3$ and $x_{Bj} = 0.6$. In both cases the data fit well to a straight line, indicating an exponential dependence on the nuclear weight, A. One notable point is that the measurement for ^{4}He deviated the most for the high x_{Bj} fit. This indicates a notable difference between ^{4}He and heavier nuclei.

Another experiment [25] performed a dedicated measurement of the A dependence of the ratio of longitudinal to transverse cross sections, commonly known as $R = \sigma_L/\sigma_T$. They measured cross sections on D, Fe, and Au, and found no dependence of R on A. This is significant since any variation in R with A would cause some A dependence in the cross section ratio and make it impossible to equate the ratio of cross sections with the ratio of the F_2 structure functions. Their cross section ratios were consistent with earlier data.

2.3.4 BCDMS

Another experiment at CERN by the BCDMS collaboration [16] used a muon beam to measure the cross sections on D, N, and Fe. Their data spanned a range of $0.08 < x_{Bj} < 0.7$, and $46 < Q^2 < 200$ $(\mathrm{GeV/c})^2$. Their results for the structure function ratio on iron were consistent with those of the EMC collaboration on Copper, and their measurement on nitrogen, the first in 1985, was consistent with the SLAC measurement on carbon. They noted that the ratio for nitrogen showed similar, but less pronounced, features to the ratio for iron. Their data showed no significant Q^2 dependence of the ratio.

2.3.5 HERMES

The HERMES collaboration [26] measured the cross sections on D, ^{3}He, N, and Kr at $0.01 < x_{Bj} < 0.65$ and $0.5 < Q^2 < 15$ $(\mathrm{GeV/c})^2$. This was the first measurement of the EMC effect in ^{3}He, and their data for the ratio were consistent with one in the shadowing and anti-shadowing region. Their highest x_{Bj} point (at $x_{Bj} = 0.6$) is also consistent with 1, but has a very large uncertainty. The neutron excess correction was also large (on the order of 5%). The data on N and Kr were consistent with previous data from SLAC and NMC. The HERMES collaboration also performed a detailed study of the Q^2 and A dependence of $R = \sigma_L/\sigma_T$. No significant Q^2 dependence was observed.

2.3.6 Jefferson Laboratory

An extraction [7] of the structure function ratio was performed at Jefferson Laboratory using data from an earlier experiment [27]. These data provided an interesting measurement of the EMC ratio in the resonance region ($Q^2 \approx 4(\mathrm{GeV/c})^2$, $1.2 < W^2 < 3(\mathrm{GeV/c})^2$) for carbon, iron, and gold. Their data were consistent with previous DIS measurements when plotted as a function of the Nachtmann variable ξ instead of x_{Bj}. This was an important result as it showed that it is possible to extract information about the deep inelastic structure functions from resonance

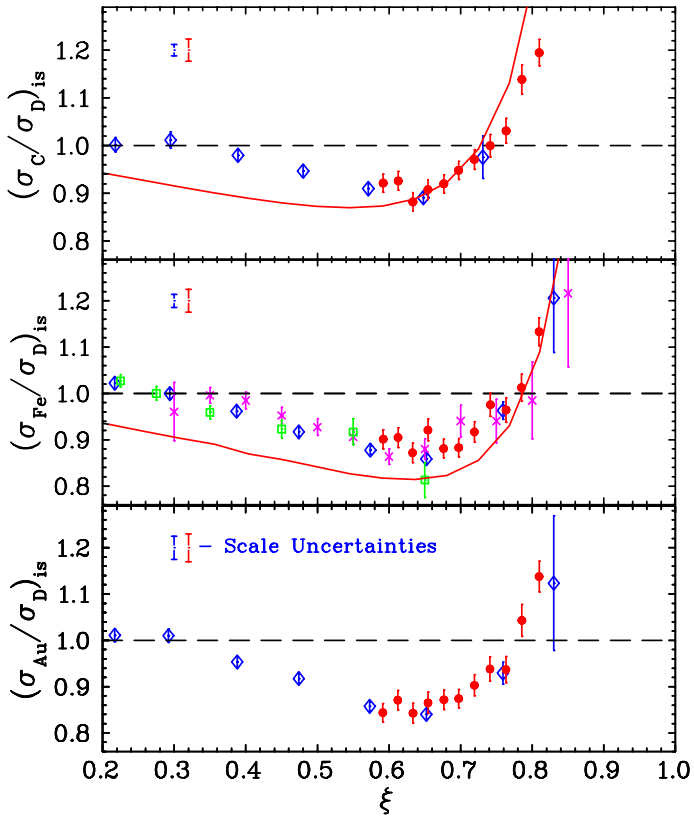

Figure 2-2: EMC Effect measured at Jefferson Lab from e89-008 [7], compared with data from SLAC e139. The JLab data were taken in the resonance region ($1.2 < W^2 < 3.0(\mathrm{GeV})^2$, $Q^2 \approx 4(\mathrm{GeV/c})^2$), but still show good agreement with the SLAC DIS data.

region data.

2.3.7 BEBC and E665

The measurement described in this thesis is focused on the EMC region and high x_{Bj}. However, there have also been more detailed studies of the structure function ratios in the shadowing region. The BEBC collaboration measured the neutrino scattering cross section on Neon and deuterium [28]. The E665 collaboration [29] measured two-jet production on Xenon and deuterium as a measure of the QCD corrections related to the structure functions.

2.4 Theoretical Considerations

There are many models that attempt to describe the EMC effect. Hadronic models attempt to better describe the EMC effect using effects relevant among nucleons and mesons. For each type of model, there are many different calculations. An exhaustive description of all these models is beyond the scope of the thesis. However, it is important to outline a few important results that are most relevant to light nuclei in the high x_{Bj} region. The interested reader can find more details in the review articles [18, 19]

In 1994, Benhar, Pandharipande, and Sick [30] used all of the existing data (350 data points at the time) to study the effect that the binding between the nucleons has on the cross section ratio. They calculated the nuclear cross section (for infinite nuclear matter) using an off-shell hadronic tensor. They were able to show that most, if not all, of the EMC effect at $x_{Bj} > 0.6$ could be explained by correctly taking into account the binding among nucleons. When they added in the effect of pion excess in nuclei, their calculation fit the data down to $x_{Bj} \approx 0.2$.

Smirnov [31] developed a simple parameterization that could be used to calculate the ratio of the F_2 structure functions over the x_{Bj} range $0 \leq x_{Bj} \leq 0.7$. He used all available data which covered a large range in A (A=4 to A=208), and Q^2 ($0.5 < Q^2 < 200(\mathrm{GeV/c})^2$). This parameterization has three parameters to be fit from data. They describe shadowing and anti-shadowing regions (the depletion and enhancement, respectively, seen at low x_{Bj}), and the EMC effect region. Most notable here are the positions of the cross-over points as a function of A. There are three cross-over points (where the ratio is equal to 1) and the position of these points is remarkably similar for each nucleus. The third cross-over point is at $x_{Bj} = 0.84 \pm 0.01$. Smirnov points out that the effects of nuclear forces are saturated at A= 3, and that binding effects are anomalously strong in ^{4}He. Therefore, one can expect that nuclei with A= 3 will have a ratio consistent with the pattern observed in heavy nuclei, but that ^{4}He may be quite different. This, of course, motivates further experiments to measure the ratio of structure functions in light nuclei.

Afnan *et al.* [32] discuss the importance of 3-body nuclei. They are concerned with extracting the free neutron structure function, F_2^n, from DIS on 3-body nuclei. They show that the ratio of EMC ratios for ^{3}He to ^{3}H is free of nuclear effects to the level of 1-2%. This uncertainty is of the same order as the experimental uncertainties associated with such a measurement, and so gives a nearly model-independent method of extracting the free neutron structure function.

A more recent work by Clöet, Bentz and Thomas [33] gives results for the ratio of the nuclear matter spin-structure function, g_1^A, to the spin-structure function of the proton, g_1^p. This ratio, the "polarized EMC effect", has never been measured. They predict that the ratio will show an even stronger x_{Bj} dependence than the unpolarized EMC effect.

2.5 Importance of Light Nuclei

There are very few data on the lightest nuclei. SLAC and NMC have studied ^{4}He over a large range in x_{Bj}, and HERMES has measured the ratio on ^{3}He at low x_{Bj}. There are no data on the EMC effect in ^{3}H. But now that the gross features of the effect are understood for heavy nuclei, it is the light nuclei which are of prime importance. The effect is expected to be smaller in ^{3}He and ^{4}He and so precision measurements on these nuclei are very difficult. The SLAC data, which cover the EMC region, have fairly large uncertainties due to the relatively thin target. The HERMES data on ^{3}He have been normalized to agree with the ^{4}He data from NMC. This makes sense if the EMC effect is the same in ^{3}He and ^{4}He. However, there is reason to expect that the effect is different in the two nuclei. ^{4}He is, of course, an anomalously tightly bound nucleus and may show a very different effect from the heavier nuclei. By contrast, A=3 nuclei are the lightest 'real' nuclei. That is, A=3 is the lightest nucleus subject to all of the usual forces that bind the heavier nuclei. Since the forces saturate at A=3, a 3-body nucleus is more like a heavy nucleus than ^{4}He. A precise measurement of the effect on ^{3}He is therefore crucial to our understanding of the models used to explain the effect for heavier nuclei. A precise measurement of the ratio on ^{3}He will

show whether the pattern seen in heavy nuclei holds, or whether there are other effects present. Furthermore, it will serve as an important test for existing models for which exact calculations are possible.

2.6 E03-103

The motivation for measuring the structure function ratio for light nuclei is strong. A measurement of this ratio on ^{3}He and ^{4}He was proposed and run at the Thomas Jefferson National Laboratory during the second half of 2004. The goal of the experiment was to perform a high statistics measurement of the inclusive electron scattering cross sections of various nuclei with low systematic error. This goal was achieved and this thesis describes the details of that experiment. From here, the discussion will proceed as follows. We will start with a detailed description of the experimental apparatus. That is followed by a discussion of how the cross section is extracted from scattering data. Finally we present the extracted cross sections and cross section ratios.

Chapter 3

Experimental Apparatus

This experiment was a measurement of the inclusive electron scattering cross section, $d\sigma/dE'd\Omega$, from nuclei. The inclusive cross section is the scattering cross section that includes all hadronic final states, so it is only necessary to measure the electron's energy and angular distribution. Electrons were detected using Hall C's High Momentum Spectrometer (HMS). This chapter describes the details of the beam and target and the HMS and its detector package.

The beam electrons impinged on the target in a scattering chamber. After the scattered electron left the target chamber, it entered the spectrometer arm. First it passed through a collimator which partially defined the acceptance of the spectrometer, and then traversed the magnet system. Quadrupole magnets focused the scattered electrons, and dipole magnets dispersed electrons of different momenta. The HMS had three quadrupole magnets and one dispersive dipole element with an effective momentum acceptance of $\pm 8\%$ about the central momentum.

After the magnets, the particles entered the detector hut. Two sets of drift chambers provided tracking of the particle in order to determine the position and angle at the focal plane between the two chambers. Then the particles traversed two planes of hodoscopes used for triggering and timing. Next was a gas Čerenkov detector used for particle identification. Then two more planes of hodoscopes. Finally, the particle entered a lead-glass calorimeter which provided additional particle identification information by measuring the kinetic energy of the particle. Detailed descriptions of the

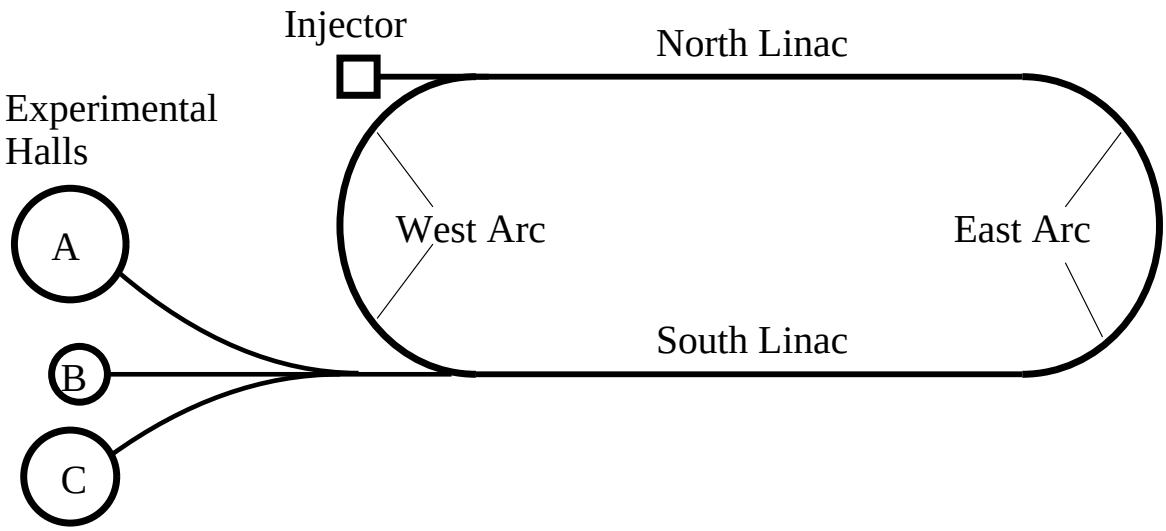

Figure 3-1: Schematic of the CEBAF Accelerator.

individual components are given in the sections below. For additional information on the Hall C spectrometers, the interested reader is encouraged to consult the seminal documents [34],[35].

3.1 Beamline

3.1.1 Accelerator

The electron beam used in E03-103 was produced by the Continuous Electron Beam Accelerator Facility (CEBAF) at Jefferson Laboratory. The electrons in CEBAF were injected into the accelerator tunnel at 0.064 GeV. They were then accelerated by the North Linac, steered through the East Arc, and then accelerated again in the South Linac. The electrons could be passed through the ring several times to achieve the desired beam energy. In E03-103 the beam was passed through the ring 5 times before being steered to the Hall. The corresponding beam energy was 5.766 GeV. Fig. 3-1 shows a schematic view of the CEBAF accelerator.

The beam energy was measured several times throughout the course of the experiment. The energy was measured by using the Hall C arc as a spectrometer [36]. During this procedure, all focusing elements were turned off and degaussed, and only

the dipole magnets were used to bend the beam into the hall. The position and direction of the beam were measured before the Hall C arc using a pair of wire scanners (harps) separated by 2.5 m. The position and direction of the beam were then measured again as the beam exited the arc. The current in the dipole magnets were varied such that the beam traveled along the central axis of the magnets. The momentum of the beam particles was then determined as

$$p = \frac{e}{\theta} \int B dl, \tag{3.1}$$

where θ is the total deflection angle of the beam (34.3 degrees in Hall C). The measurement depends on a precise knowledge of the magnetic field. One of the dipoles in the arc has been extensively field-mapped as a function of current. The precision of the field map allowed the beam energy to be measured to a precision of one part in 10^3.

Following the measurement, the focusing elements and steering coil were re-energized for running. It was assumed that this procedure did not disturb the beam energy. During normal running, the beam position monitors were used to monitor the beam energy. However, these monitors were not as accurate as the super harps used during the energy measurement, and were mostly used to detect relative shifts in the beam energy from run to run.

3.1.2 Beam Position Monitors

The horizontal and vertical positions of the beam were monitored using several beam position monitors (BPMs). These monitors were resonating cavities whose fundamental frequencies had harmonics at the beam pulse frequency (1497 MHz) and the Hall C pulse frequency (499 MHz). Four antennae picked up a signal at the resonant frequency and the displacement of the beam from the antenna could be directly related to the strength of the signal. The four antennae were rotated by 45° from the horizontal/vertical in order to avoid damage from synchrotron radiation produced from steering the beam. The machine operators used the beam position monitors to

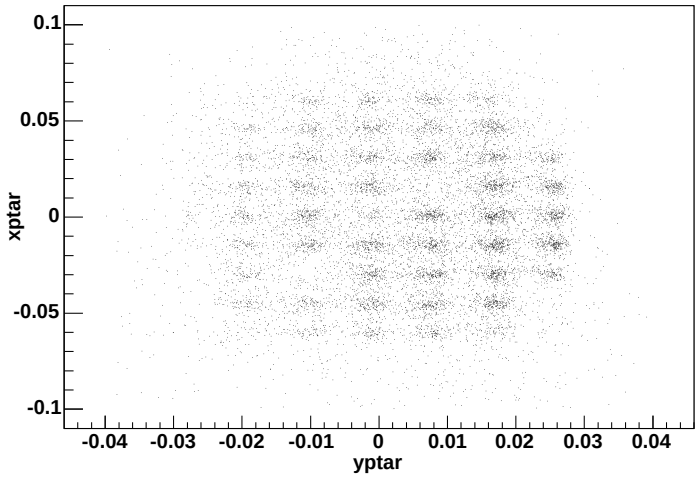

Figure 3-2: Sieve slit pattern. This plot shows the angular distribution of events at the target. *yptar* and *xptar* are approximately the in-plane and out-of-plane scattering angles. The beam position was adjusted until the pattern above was centered about the smaller hole at $xptar = 0, yptar = 0$. The two empty regions at $\pm 0.01, \pm 0.03$ are the filled holes in the sieve slit used to orient pattern.

steer the beam into the Hall. Additionally, three other sets of monitors (H00Ax/y, H00Bx/y, and H00Cx/y) were used by the shift crew to ensure that the beam impinged on the target at a consistent position over the course of the run. The nominal position was stable to 0.1mm. The nominal beam positions are shown in Tab. 3.1. The third BPM (H00C) was present in the data, but was not used. The nominal positions were determined by adjusting the beam position until the beam axis and HMS axis intersected. This was determined using a sieve slit aperture as shown in Fig. 3-2. The sieve slit has a grid of holes that allow particles to pass through. The hole at the center of the aperture is smaller than the other holes, and two of the holes are filled in order to orient the pattern. When the pattern is centered about the smaller central hole, the beam axis and spectrometer axis were aligned.

BPM	Nom. x Pos. (mm)	Nom. y Pos. (mm)
H00A	0.80	-1.83
H00B	0.48	-1.50
H00C	0.48	-1.48

Table 3.1: Nominal beam positions for E03-103.

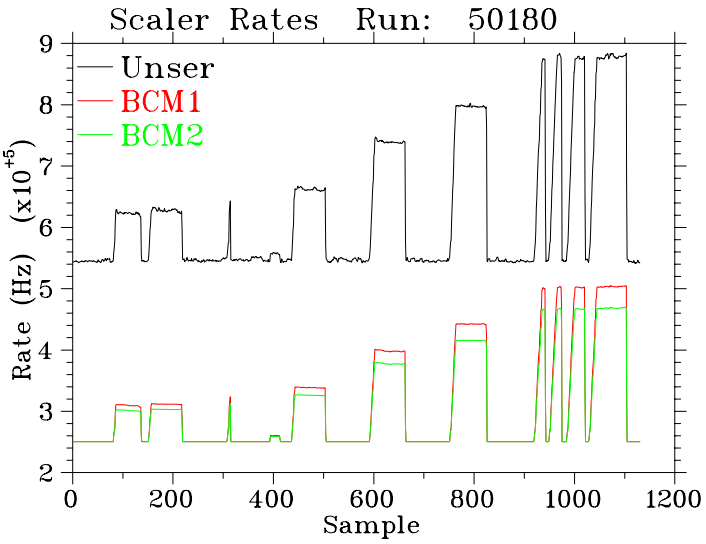

Figure 3-3: Example of a BCM Calibration run. The beam current was ramped up with alternating on and off periods. The current was averaged over the two minute on and off periods. The beam current was set to zero between on periods in order to account for any drift in the Unser offset over the course of the run.

3.1.3 Beam Current Monitors

The particle yield measured in the experiment was proportional to the charge delivered to the target, which was equal to the time integral of the beam current. Therefore, the quality of the measurement of the beam current was of utmost importance in making a precise measurement of the cross section. The beam current was continuously monitored using two microwave cavity Beam Current Monitors (BCMs) and a parametric DC current transformer (Unser monitor).

The geometry of the BCM cavities was chosen such that their natural frequencies had harmonics at the pulse frequencies of the accelerator pulse rate (1497 MHz) and at the Hall C pulse rate (499 MHz). The signals from these cavities were picked up by antennae, whose signals were integrated and read out every 2 seconds. The Unser zero-offset could drift due to temperature fluctuations, but its gain was very stable and precisely measured. The BCMs were calibrated several times throughout the run. During a calibration run, the current was ramped up with alternating beam-on and beam-off periods of about 2 minutes as shown in Fig. 3-3. The zero-offset for the Unser was then measured at each of the beam-off regions, and the gain was fit to the

beam-on regions. The gain and offset for the BCMs were determined by comparison to the Unser. Several BCM calibrations were made over the course of the data-taking period. A global calibration was performed using all of the calibration runs and this global calibration was used to compute the charge for all runs. The residuals from the calibrations, relative to the global calibration, are shown in Fig. 3-4. The scatter in the calibrations relative to the global calibration, shown in Fig. 3-4, gives an overall uncertainty in the measured beam current of 0.25 μA. The charge was computed by integrating the current over two second intervals after excluding the times when the beam was off.

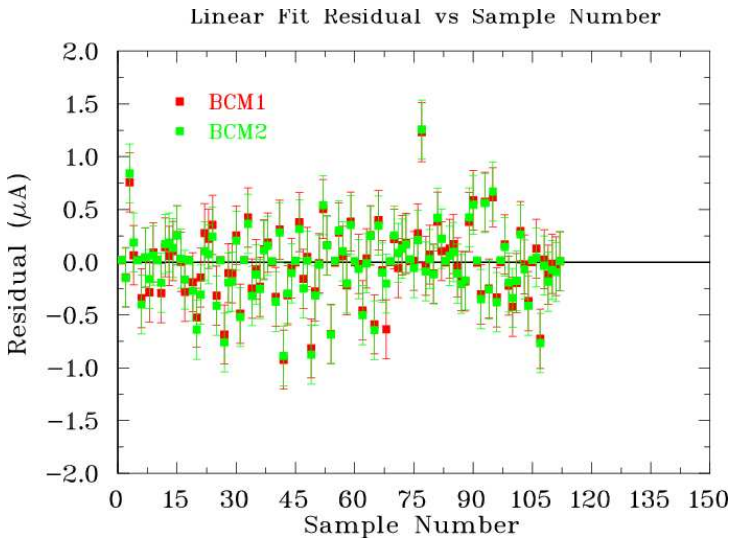

Figure 3-4: BCM calibrations over the course of the measurements. This plot shows the residuals from each calibration, relative to the global fit.

3.1.4 Raster

The beam current delivered to the target was typically between 10 and 100μA. This current was delivered in a beam with a small transverse size of $\pm$200μm (FWHM). The amount of power in this small of an area could cause local boiling in the cryotargets, or cause the solid targets to melt. To avoid overheating, therefore, the beam was rastered on the target so that the high power was distributed over a larger area. Two sets of magnets, about 20 m upstream of the target, oscillated the beam vertically

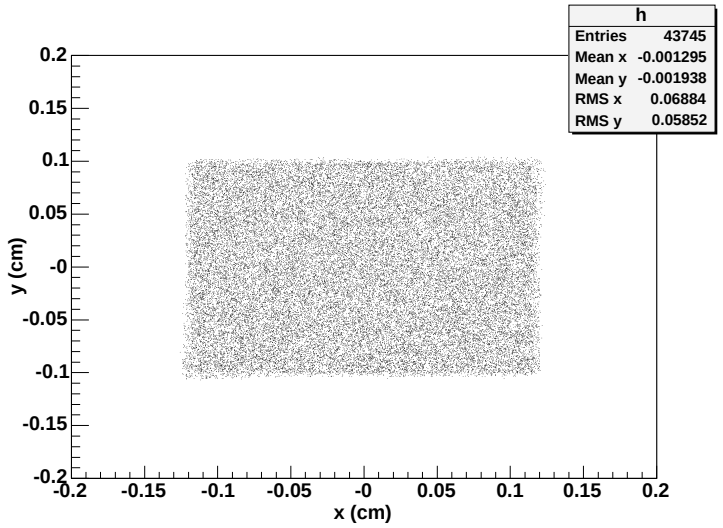

Figure 3-5: Beam Raster Pattern. The beam was rastered horizontally and vertically in order to prevent local boiling or melting of the target. Two triangular waveforms of different frequencies were used to more uniformly fill the rectangular raster region.

and horizontally through a triangular waveform. Different oscillating frequencies were used for the vertical and horizontal magnets to prevent the beam path from assuming a stable Lissajous configuration, and more uniform coverage of the rectangle determined by the extent of the raster magnets. The raster pattern is shown in Fig. 3-5. Uniform coverage over the raster pattern reduced the risk of local boiling and ensured that the measured yield did not depend on the horizontal or vertical position of the interaction point.

3.2 Targets

The target system consisted of a target ladder within the scattering chamber, which held all solid targets and three different loops for cryogenic targets. Two cryo-loops were used during each running period and one cryo loop was left empty as a spare. Data were taken in two different periods, the first with ^{3}He and ^{4}He, and the second with liquid hydrogen and liquid deuterium in the loops. Since the target chamber and the beamline shared a common vacuum, there was no entrance window to the scattering chamber. The various targets are arranged on a target ladder so that

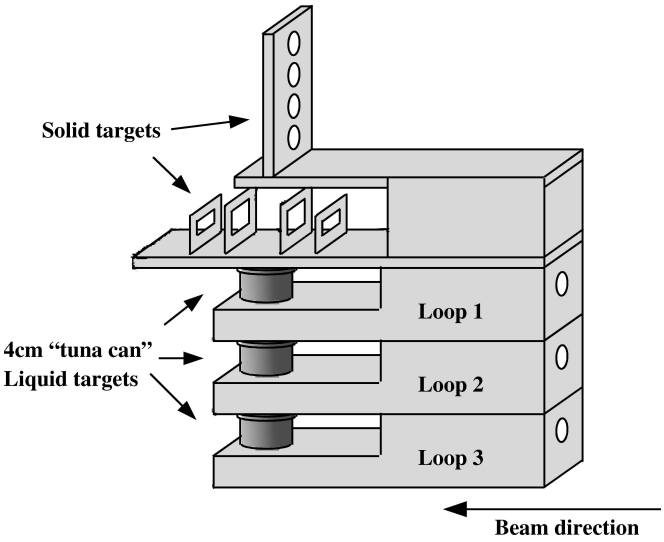

Figure 3-6: Schematic of the Hall C target ladder. The solid targets and two cryotargets were installed during each running period. One cryo-loop was left empty as a spare. The target-ladder arrangement allowed for different targets to be changed in a matter of minutes without breaking vacuum.

targets could be exchanged in a matter of minutes. The target ladder is shown in Fig. 3-6.

The thicknesses of the cryogenic targets were computed from the target density, which was computed from the pressure and temperature of the cryogen. The pressure and temperature of the cryogenic targets were monitored continuously throughout the experiment. The uncertainty of the target thickness depends on the absolute measurements of pressure and temperature, but also on their stability over time. The temperature in each loop was determined by a resistance measurement from two Lakeshore Cernox resistors and was measured to a precision of ~ 100 mK. The temperatures of the deuterium and hydrogen targets were maintained at 22 K and 19 K respectively, with an uncertainty of 0.5% on the absolute temperature measurement. The temperatures of the ^{3}He and ^{4}He targets were maintained at nominal values of 5.8 K and 6.2 K respectively. The uncertainty in the temperature and pressure give the uncertainty in the density measurement via the equation of state, and was dominated by the temperature dependence. The hydrogen targets' densities were stable, within uncertainties, throughout the course of the run, and so a single density was used for each target. The densities of the helium targets, however, varied enough over

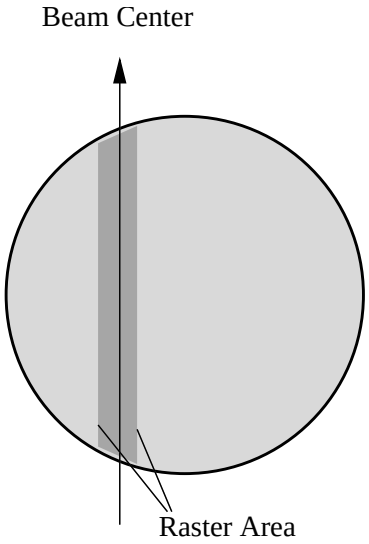

Figure 3-7: Schematic of the cryo-target. The beam is shown passing through the target off center. The dark shading indicates the width of the raster pattern. Both the offset of the beam center and the averaging of the target thickness over the raster pattern are described in section 3.2.1.

the course of the run that it was necessary to compute a density for each run. The relative uncertainty for the density of the cryogen was 0.5% for the hydrogen targets and 1.4% and 0.8% for ^{3}He and ^{4}He, respectively. To compute the total cryotarget thickness, the density was combined with the carefully computed target length as outlined in the next section.

3.2.1 Cryo-Target Thicknesses

Each cryogenic target was composed of a cylindrical, thin-walled aluminum cell, commonly referred to as a "tuna-can". The axis of the can was oriented vertically in the hall, so the target thickness seen by the beam depended on the horizontal position of the beam relative to the cell center. This section outlines the details of computing the cryo-target thicknesses used to compute the cross sections.

There were several factors that had to be taken into account when computing the thickness. First, the geometry of the target cell (diameter of the can, thickness of the walls, etc.) was measured at room temperature, so there was a thermal contraction that had to be taken into account. In addition, there were several components that

Loop	OD(mm)	wall 1(mm)	wall 2(mm)	ID_{warm}(cm)	f	ID_{cold}(cm)
1	40.13(8)	0.1384(13)	0.1270(13)	3.986(8)	0.996	3.969(8)
2	40.18(8)	0.1219(13)	0.1219(13)	3.994(8)	0.996	3.977(8)
3	40.16(8)	0.1232(13)	0.1194(13)	3.992(8)	0.996	3.975(8)

Table 3.2: Cryo-target loop geometry. The outer diameter (OD) includes the cell walls. Taking the difference between the OD and the cell walls gives the inner diameter (ID), which gives the dimensions of the cryogenic material in the beamline. This number had to be corrected for thermal contraction. The cold value of the ID is given in the last column of the table.

could move relative to one another. The target ladder was known to move slightly as the system was cooled, the cells themselves could shift relative to the target ladder, and finally, the beam position could shift relative to the center-beam line.

The parameters of the three cells are shown in Tab. 3.2 and were taken from[37]. The thermal contraction of the cell was given by the final temperature of the Loops and the contraction of Aluminum. The expansion coefficient f for Aluminum becomes non-linear at very low temperatures. In particular, the total length contraction factor becomes relatively independent of temperature below 25 K. All the cryotargets were operated in this range and the contraction factor was determined to be 0.996 by [38] for each of the three loops.

The values in Tab. 3.2 represent the nominal length of the cryogenic targets. In practice, however, the beam could be offset from the center of the cell due to position shifts in both the beam and target. These shifts had to be properly accounted for in order to compute the correct target thickness (see Fig. 3-7). The nominal beam position was determined to be 1.0 mm to the left of the beam axis. Also, the target ladder was shifted 2.5 mm to the right of the beam axis. Finally, the target cell positions within the target ladder were surveyed during the running period and were found to be offset from their nominal positions on the target ladder. The offsets for the three cryo-target loops are shown in Tab. 3.3.

The target length seen by the beam is given by the length of the chord that the beam traverses. If the target cell has a radius r, and the beam crosses the target in

Target	Loop	offset(mm)	y(cm)	$\bar{y}$(cm)	$\rho(gm/cm^3)$	τ(gm/cm^2)
LH2	2	-0.03(20)	3.914(25)	3.911(26)	0.0723	0.2828(23)
LD2	3	-0.10(20)	3.909(26)	3.907(26)	0.167	0.6525(52)
He3	2	-0.03(20)	3.914(25)	3.911(26)	0.0708	0.2769(42)
He4	1	+0.31(20)	3.917(24)	3.915(26)	0.135	0.5285(53)

Table 3.3: Cryo-target loop cell offsets and final target thicknesses. The table lists the offsets of the cells from the target-ladder center. A minus sign indicates an offset towards beam-right. The target length at the beam center, and the raster-averaged beam length are shown. The final target thickness in the last column is a product of the raster-averaged target length, $\bar{y}$, and the nominal target density. (Note that the target densities shown for the helium targets are approximate values shown for reference only. The actual densities for these targets were computed for each run based on the measured temperature and pressure.) An uncertainty has been applied to the target thickness representing the uncertainty in the total target length due to the uncertainty in the offset and the uncertainty on the target density added in quadrature.

a line offset from the diameter by a distance x, then the length is

$$y = \sqrt{r^2 - x^2}. \tag{3.2}$$

The relative position of the beam and target cell centers was given by the sum of all the offsets. In addition, since the beam was rastered over a small area, it was necessary to average the expression above over the width of the raster pattern to find the average target thickness. The raster-averaged target thickness was found by multiplying the target material density by the raster-averaged target length,

$$\bar{y} = \frac{\int_{x_0-w}^{x_0+w} \sqrt{r^2 - x^2} dx}{\Delta x}. \tag{3.3}$$

The limits on the integral are defined by the edges of the raster pattern. In this case the limits were $\pm w = 1.2$mm about the beam center, x_0. The nominal target thicknesses and the raster-averaged thickness are shown in Tab. 3.3. The raster-averaged target thickness was chosen as the best estimate of the target thickness for the data presented here. A summary showing all target thicknesses is given in Tab. 3.4

Target	Thickness (g/cm^2)	% rad. length
^{1}H	0.2828(23)	0.463
^{2}H	0.6525(52)	0.535
^{3}He*	0.2769(42)	0.429
^{4}He*	0.5285(53)	0.476
^{9}Be	1.8703(93)	2.87
^{12}C	0.6667(33)	1.561
^{63}Cu	0.7986(40)	6.21
^{197}Au	0.3795(19)	5.875
Al dummy foil 1	0.2626(13)	1.10
Al dummy foil 2	0.2633(13)	1.09

Table 3.4: Hall C target thicknesses. *Note that the thicknesses for the helium targets were calculated for each run, so the numbers for those targets are approximate. Also, note that the radiation lengths shown for the cryotargets are for the cryogen only and do not include the radiation length due to the cell walls.

3.3 HMS Spectrometer

We now move on to discuss the Hall C High Momentum Spectrometer (HMS), shown in Fig. 3-8. The spectrometer includes all materials and detectors that the particle traverses after leaving the target. The spectrometer consists of a set of focusing quadrupole magnets, a dipole magnet to select momentum and the detector package used to count the particles and measure their energies. This section discuses each of these pieces in detail, starting with the magnets and ending with the detector package.

3.3.1 Magnets

The HMS had three focusing quadrupole elements and a dispersive dipole element. The quadrupoles were superconducting magnets and were tuned so that particles originating from the same point in the target with the same momentum would end up at the same point in the focal plane. The first and third quadrupoles focused particles in the dispersive direction, and the second one focused particles in the non-dispersive direction, providing a large momentum bite and target acceptance. The fields in the quadrupoles were set by setting the currents according to a routine that gave the

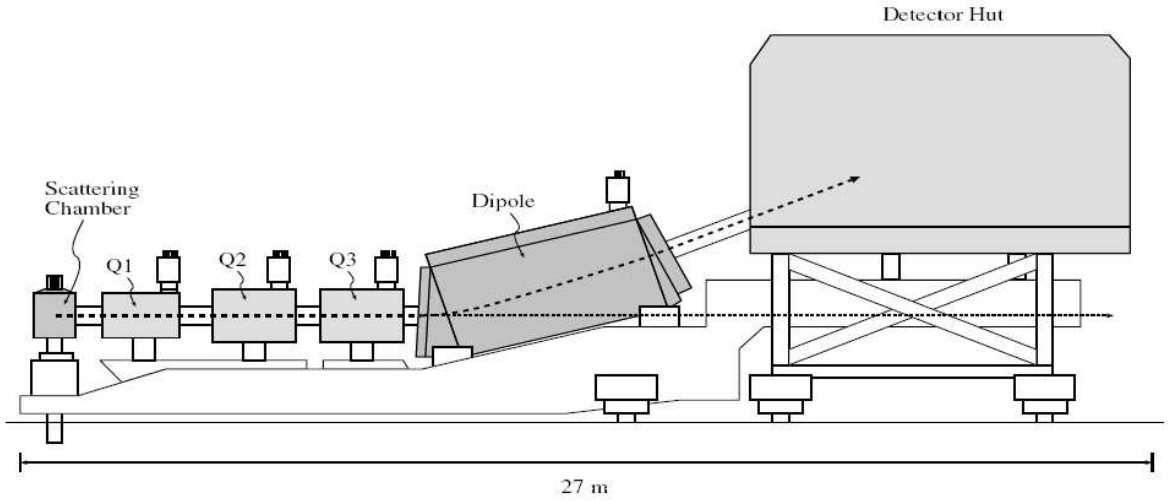

Figure 3-8: HMS Spectrometer showing the three focusing quadrupole magnets and the dispersive dipole element.

current for each magnet given the desired momentum. All of the magnets in the HMS were superconducting, and therefore the effects of hysteresis were known to be small (at the level of 10^{-3}[35]), however, in order to further minimize any hysteresis, the following procedure was followed. For a given angle, the largest momentum setting data were taken first, and then the momentum settings were stepped down through the desired settings. When ramping up to the highest momentum setting, the current was first set $\sim$ 200A above the desired set point, and then ramped down to the set point. Hall probes were used to monitor the fields during running. The field in the quadrupoles was found to be reproducible to the 10^{-4} level. The dipole was ramped up to the desired field using a feedback loop with an NMR probe inside the magnet. The central momentum of the spectrometer was determined by the setting of the dipole field, which bent particle trajectories 25° into the detector hut. The spectrometer had a total momentum bite of approximately $\pm$10%. However, since the acceptance was limited by the quality of the tracking at the edges of this momentum bite, the effective acceptance was limited to $\pm$8%.

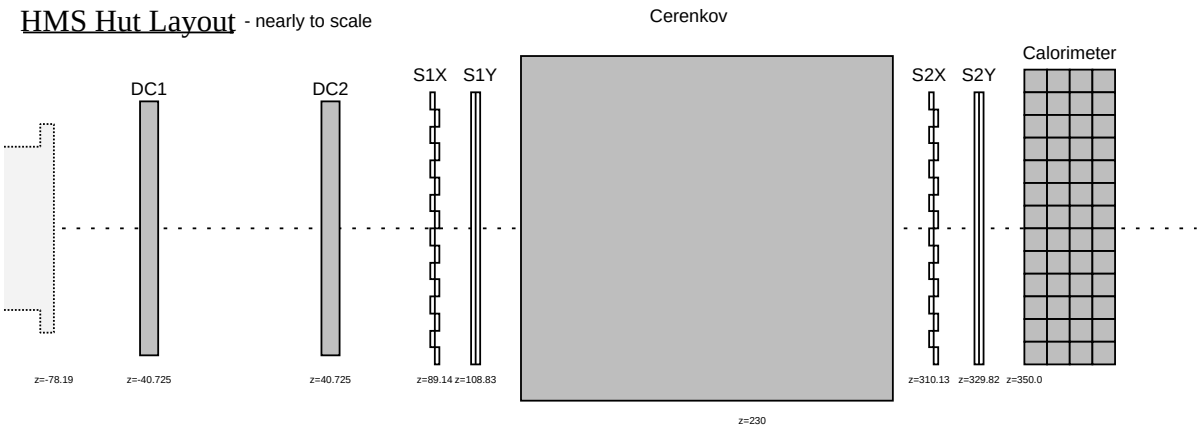

Figure 3-9: A schematic view of the major elements of the HMS Detector Package.

3.4 Detector Package

After the scattered particles passed through the magnet system, they arrived at the detector hut. The HMS detector package, shown schematically in Fig. 3-9, included detectors used for triggering the passage of the particle, detectors for computing the trajectory of the particle, and detectors used to determine what type of particle it was. This section gives detailed description of each of the detector types and how they were used.

3.4.1 Triggering: Hodoscopes

The HMS contained four planes of scintillator counters. The two "x" planes were segmented in the dispersive direction and the two "y" planes were segmented in the non-dispersive direction. In the HMS there were 10 scintillator counters in the dispersive planes and 16 in the non-dispersive planes. Each counter, or paddle, consisted of scintillating material (BC404) instrumented with phototubes (Philips XP2282B) on each end. The scintillator was coupled to the phototubes by UVT lucite light guides. When a charged particle passed through the scintillating material it would deposit a small amount of energy which was converted to light. The light propagated through the scintillator paddle in both directions and produced signals in both phototubes. The scintillator paddles were one cm thick and eight cm wide, and adjacent paddles

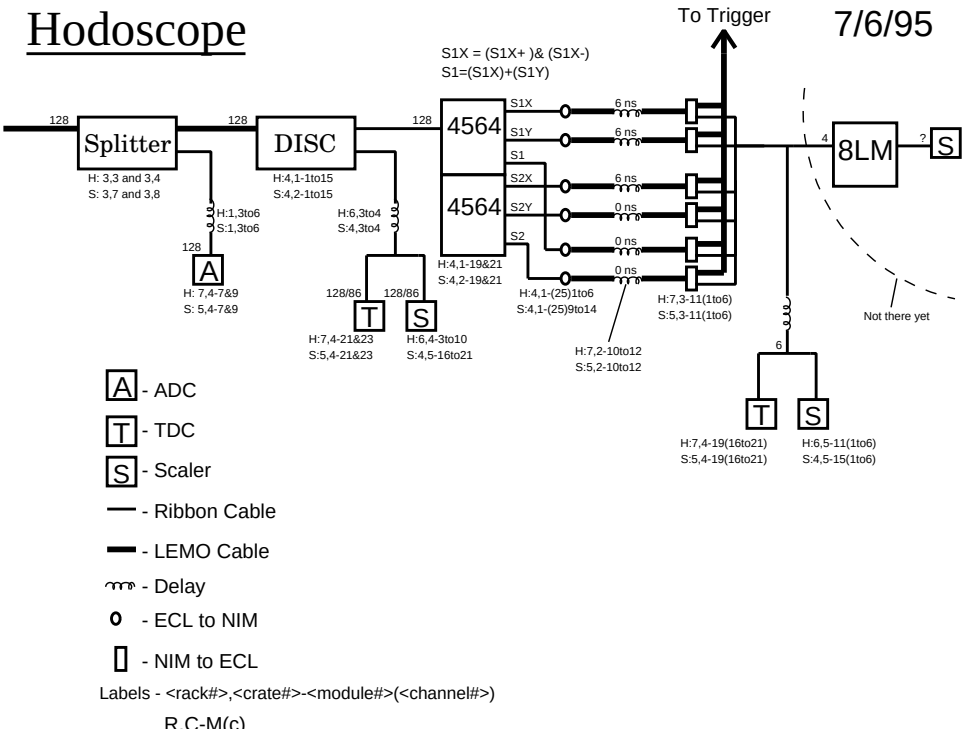

Figure 3-10: HMS Scintillator electronics. The signal for each tube is sent to a TDC, ADC, and a scaler. The signals from tubes on the same paddle or plane are combined to form the basic trigger.

in the same plane were staggered such that there was a 0.5 cm overlap to prevent any particles missing a plane by passing through the space between paddles.

The signals from the phototubes were sent to ADCs and TDCs, as well as scalers and logic modules for triggering. The scintillator planes form the basis of the HMS trigger. All tubes from one end of a plane were `OR`'d together, and all tubes from the other end were `OR`'d together. These `OR`s were then `AND`ed together. If there was at least one hit from each end of the plane (meaning that at least one tube on each end produced a signal larger than a pre-set discriminator) then the plane satisfied the `AND`. The `AND`s from the four planes were used together and in combination with signals from other detectors to form various trigger types as outlined in section 3.6.1. Fig. 3-10 shows the electronics chain for the scintillator planes.

Timing information from the phototubes was corrected for pulse height and timing offsets in each element. The discriminators in the electronics were constant threshold discriminators, which turned on once the received pulse reached the level set at the

discriminator. This biased the timing for different particles since the rise time for the pulses for different particles would be the same. Particles which deposited a lot of energy (protons, for example) would reach the threshold at an earlier point on the leading edge than particles that deposited less energy (minimum ionizing pions for example). (A constant fraction discriminator, on the other hand, starts the logic pulse at a constant point along the rising edge.) This effect and the timing offsets were corrected for each channel using an offline calibration routine originally developed for SLAC experiment NE18 that has been modified for use in Hall C. For details on these procedures, see [39].

3.4.2 Tracking: Drift Chambers

Drift Chambers were used to find the position and directions of the particle at the focal plane. This information was required in order to reconstruct the position and momentum at the target. The tracking system was comprised of two sets of drift chambers, one in front of and one behind the focal plane. Drift chambers produce a signal from the ionization trail that charged particles leave as they pass through the gas in the chamber. The liberated electrons are collected at the wires in the chamber, and the timing of the signals at the hit wires are used to reconstruct a track for the particle that passed through the chamber. The chambers in the HMS were filled with a mixture of equal parts argon and methane which was maintained and fed to the chambers from a hut above the hall.

Each drift chamber in the HMS had six sets of sense wires: the x and x' planes measured the dispersive direction, y and y' planes measure in the non-dispersive direction, and the u and v planes were rotated by $\pm 15^{\circ}$ from the x and x' planes. The planes were spaced 1.8 cm apart. The orientation of the wires in the HMS drift chambers is illustrated in Fig. 3-11. Each wire in the chamber was read out by a TDC. The timing signals from the wires, relative to the trigger start, were converted to position coordinates and combined to form a stub (a short track formed from the hits in a single chamber) in each chamber. The stubs from the two chambers were combined to form the final track. This track was used to find the position and

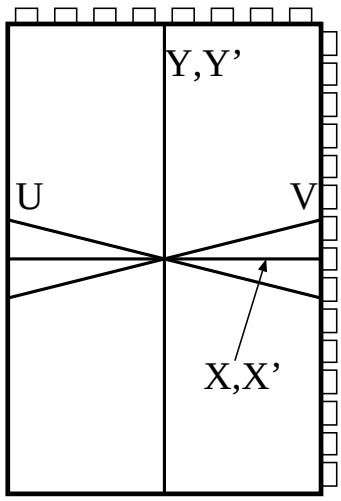

Figure 3-11: Wire orientations in the HMS Drift Chambers, as seen from the point of view of an incoming electron.

direction of the particle at the focal plane, and then at the target. The wires in a given plane were arranged as follows. There were alternating field and sense wires. The field wires were maintained at a large negative potential ($\sim$ 2000 Volts) relative to the sense wires. The spacing between the sense wires was $\sim$ 1 cm. In addition to the field and sense wires, there were guard wires which directed the field lines to lie more uniformly in the drift plane.

The positions of the hit wires gave some information on the position of the particle in the plane. Using the timing signals from all six planes in a plane, however, allowed for a much more precise determination. The timing signal of each wire is used to determine the distance from the wire that the particle passed through the plane. By comparing the wires hit in different planes it was possible to determine on which side of a given wire the particle passed. If there were hits in two planes where the wires were parallel, then the particle was assumed to have passed between the two wires. The wires in these two planes were offset from each other by 0.5 cm so there was no ambiguity. In cases that were ambiguous (hits in the u and v planes, which did not have matching parallel planes, or when there were not six hits in a chamber), the side was determined by forming all possible combinations and choosing the stub with the lowest χ^2. The track information from the two chambers was combined to

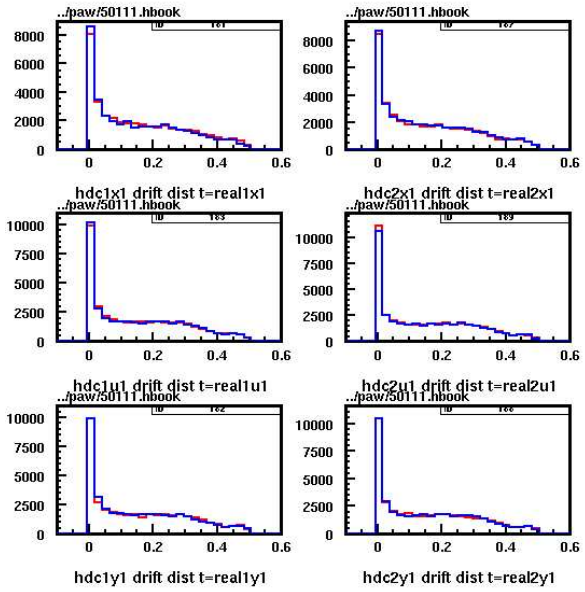

Figure 3-12: Drift distance spectrum before fitting.

form a single track, which gave the position at the focal plane. With the focal plane quantities known, the particle's trajectory at the target could be determined using the optics matrix (see section 3.4.3).

The TDC information from the wires was converted to positions using a driftmap. A driftmap gives the calculated distance from the wire that an event occurred, based on the time between the stop and start for the event. Since the wires were spaced very close together, the distribution of events about the wire should be flat. The time-to-distance coefficients for each wire were adjusted until the driftmap spectra appeared flat. Examples of the driftmap before fitting and after fitting is shown in Figs. 3-12 and 3-13.

3.4.3 Matrix Elements

Once the tracks were fit and the particle's position and direction at the focal plane were known, it was possible to reconstruct the initial position and momentum at the target. This was done by transforming the focal plane quantities to target quantities using a mapping matrix.

The four quantities known at the focal plane were the particle's position in the

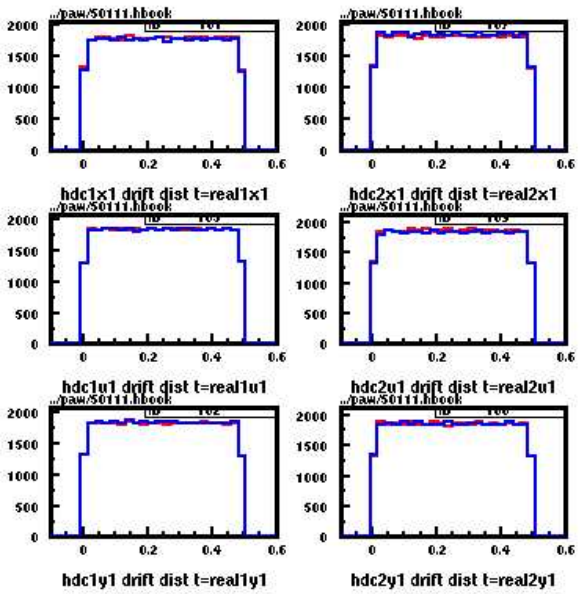

Figure 3-13: Drift distance spectrum after fitting.

focal plane, x_{fp}, y_{fp}, and the particle's direction at the focal plane, x'_{fp}, y'_{fp}. These directions were really the slope of the track in x and y directions ($x'_{fp} = dx/dz, y'_{fp} = dy/dz$ where z is the direction along the axis of the spectrometer. Note that the x direction was parallel to the dispersive direction of the spectrometer and also to the out-of-plane scattering angle direction, and the y direction was parallel to the non-dispersive direction and corresponded to the in-plane scattering angle. The four corresponding quantities of interest at the target were the position of the interaction point, y_{tar}, the slopes at the interaction point, x'_{tar}, y'_{tar}, and the fractional deviation from the central momentum, δ. Note that x_{tar} was not given by the transformation, and was assumed to be equal to zero. The matrix that maps to the target variables has the form

$$x^i_{tar} = \sum M^i_{j,k,l,m} (x_{fp})^j (y_{fp})^k (x'_{fp})^l (x'_{fp})^m. \tag{3.4}$$

The sum over j,k,l,m is constrained such that

$$j + k + l + m \leq N, \tag{3.5}$$

where N is the order of the transformation. The matrix used for the HMS tracking

went up to fifth order. The matrix elements were determined in an iterative fitting procedure. The first step was to determine a starting matrix using monte carlo data with a model of the HMS magnetic optics. Then the target variables were fit using data that were taken especially for the fitting procedure. The angles x' and y' were found using a point target and the sieve slit located just before the first quadrupole. The sieve pattern made it possible to determine which hole a particle went through on it's way through the spectrometer. The position y_{tar} was determined using an optics target which has various point targets spaced along the beam line, giving a discrete distribution of y_{tar} values. Finally, δ was fit by performing scans in which the magnetic field was adjusted to move the elastic peak across the acceptance. Since the momentum of the particles in the peak are known, and the central momentum of the spectrometer is also known at each setting, the δ value could be determined and the matrix elements fit. The matrix fitting procedure is detailed in [40].

3.5 Particle Identification

The basic scintillator trigger accepted triggers from any of the various charged particles that arrived at the spectrometer. At some kinematics in E03-103 the rate for pions was much greater than the rate for electrons. It was therefore necessary to have ways to distinguish the the signal electrons from pions and other background sources. The HMS had two detectors used for particle identification, a threshold gas Čerenkov counter and a lead-glass calorimeter. Both detectors were used at the trigger level to preselect electrons, and at the software level for more careful signal selection and background suppression. The next two sections outline these two detectors and their use in the analysis.

3.5.1 Čerenkov

A Čerenkov detector relies on the Čerenkov effect to detect the passage of charged particles. When the velocity, β, of a charged particle exceeds the speed of light in the medium, $1/n$, the particle will emit a small number of photons at a fixed angle

given by $\cos\theta = 1/\beta n$. This effect makes it possible to distinguish between particles of different masses by selecting a material for which the particle of interest will be above the threshold velocity. The Čerenkov detector in the HMS was arranged so that electrons over the entire momentum range would be above the threshold, but heavier particles, like pions, would not.

The HMS Čerenkov detector was composed of a large gas volume instrumented with two mirrors which focused the Čerenkov light onto two photomultiplier tubes. The gas used in the detector was C_4F_{10} at a pressure of 5.15 psi ($\sim$ 0.35 atmosphere). The index of refraction of 1.0005 gave a threshold momentum of $\sim$ 16 MeV for electrons, and $\sim$ 4.5 GeV for pions. The momentum range for this experiment went from about 800 MeV to 5.6 GeV, so at the highest momentum settings the Čerenkov was not as effective at distinguishing electrons from pions.

The Gas Čerenkov was calibrated by finding the minimum response that each photomultiplier tube could produce. The minimum signal a tube can produce was the signal that results from a single photo-electron being ejected from the photocathode by the incident light produced by the charged particle. The amount of current produced in the photomultiplier tube by a single photoelectron is, in principle, a feature of the tube itself, and should have no sensitivity to the type or the momentum of the particle that produced the light in the detector. However, the signal could depend on the rate at which the tube fired. A kinematic setting with very high particle rates would have a higher single photoelectron peak due to an effective dark current in the tube, than a setting with very low rates. For this reason, it was necessary to calibrate the tubes using particle types and rates that corresponded to the settings used in the experiment, rather than low-rate cosmic rays, for example.

The calibration proceeded by locating the position of the single photo-electron peak in the ADC spectrum for each tube. A sample ADC spectrum is shown in Fig. 3-14. The most prominent features of the spectrum are the sharp peak at zero (the pedestal), corresponding to no signal; the single photoelectron (SPE) peak slightly above zero; and then the continuum regime, corresponding to more than one photoelectron. A Gaussian fit was performed to find the SPE peak in ADC channels. This

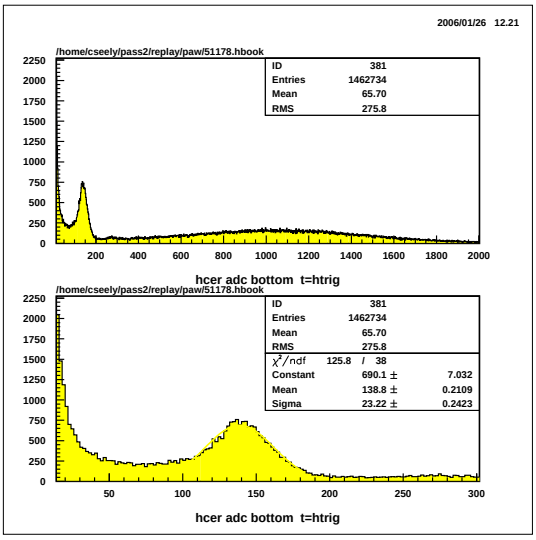

Figure 3-14: HMS Čerenkov ADC spectrum. The top panel shows the pedestal, single photo-electron peak, and the continuum. The bottom panel shows a close-up of the single photo-electron peak including the Gaussian fit. The peak position of the Gaussian is used to compute the total number of photo-electrons from the ADC value.

value was then used in the analysis code to calculate the number of photo-electrons produced during a given event from the value of the ADC for that event. This procedure was repeated for both photomultiplier tubes in the detector. The number of photoelectrons for an event was defined as the sum of the number of photoelectrons in the two photomultiplier tubes. In this analysis, events were accepted if there were > 1.5 photo-electrons detected. The tube calibrations were checked over the course of the run and found to be stable at the 5-10% level. The width of the single photo-electron peak was about 15%. Since the shifting of the peak centroid was smaller than the width of the peaks, a single set of calibration constants were used throughout the experiment.

Note that pions should not have produced Čerenkov light in the gas volume, but it was still possible for pions to produce large signals in the Čerenkov and thus pass the cuts described above. This happened when knock-on electrons were produced in the Aluminum entrance window to the Čerenkov and passed into the gas volume. These events resulted in a set of background events that could not be eliminated with the Čerenkov alone, so it was necessary to have a second detector with which to eliminate

these events.

3.5.2 Calorimeter

As described in the previous section, some pion events could pass the Čerenkov cut. In order to remove these events another detector that can distinguish different particle types is needed. A calorimeter measures energy deposited by charged particles. The HMS calorimeter was composed of four layers of lead-glass blocks whose long axis was parallel to the non-dispersive direction. Each layer had 13 blocks of dimensions $10 \times 10 \times 70$ cm^3. In the first two layers (as seen by the incoming particle) both ends of each block were instrumented with phototubes, and in the second layer only one end of each block was instrumented.

As charged particles pass through lead glass they lose energy via ionization or Bremsstrahlung. The photons produced by these mechanisms go on to produce electron positron pairs which continue to lose energy in the material. The light produced in this way is transported along the blocks and detected by the phototubes. Electrons lose energy rapidly through Bremsstrahlung radiation. The calorimeter was about 18 radiation lengths so electrons were almost completely absorbed. Pions, on the other hand, are nearly minimum ionizing particles at the energies in this experiment and so deposited only a fraction of their kinetic energy in the calorimeter. Fig. 3-15 shows the normalized deposited-energy spectrum (E_{dep}/E_{track}). There are clear peaks corresponding to electrons (near $E_{dep}/E_{track} = 1$) and pions ($E_{dep}/E_{track} = 0.25$). However, the pion peak has a long high energy tail that bleeds into the electron peak. So it is not possible to use the calorimeter alone to distinguish electrons from pions. Once the Čerenkov cut has been applied, however, it is clear that the electrons and pions are quite well separated as shown in Fig. 3-16, and then a simple cut on the energy deposited in the calorimeter served to eliminate any pion events that may have passed the Čerenkov cut. Note that, since the energy deposited by pions is roughly independent of the particle momentum, the pion peak in the E_{dep}/E_{track} spectrum moves to lower E_{dep}/E_{track} for higher particle momenta; and that the resolution of the calorimeter was proportional to $1/\sqrt{p}$. This gave a larger separation between the

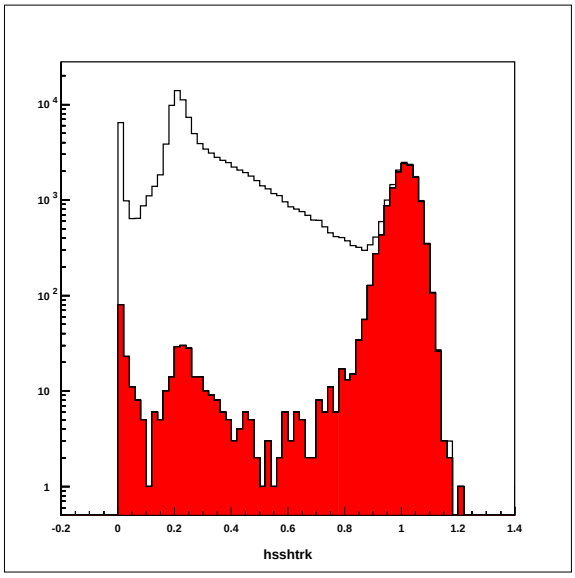

Figure 3-15: Ratio of energy deposited in the calorimeter to the track's momentum. The shaded region is the ratio after a cut has been placed on the number (> 1.5) of photo-electrons in the Čerenkov detector.

electron and pion peaks.

The ADC for each phototube in the calorimeter had a corresponding coefficient which was used to convert the ADC signal into a deposited energy. The coefficients were calibrated such that the energy deposition peak (where the deposited energy is normalized to the particle momentum as determined by the tracking system) for electrons is centered at one. The coefficients were determined using a high-statistics run, with cuts placed on the Čerenkov to give a clean electron sample. The coefficients start with an initial value, then were varied one at a time. Each time a coefficient is varied the χ^2 for the event sample is computed. This process continues until the χ^2 value is close to one and has stopped changing.

It was discovered after the data were taken that there was a problem with the Calorimeter ADCs. The ADCs exhibited a shifting gain that was present throughout the run. This problem is discussed in Sec. A.3. The shift led to an artificial, but still acceptable, increase in resolution. Due to the difficulty associated with correcting each run for these shifts, no correction was made. Instead, the effect was accounted for in the systematic error associated with the cut on the `HSSHSUM` peak. The increase in the uncertainty is small, about 0.1%.

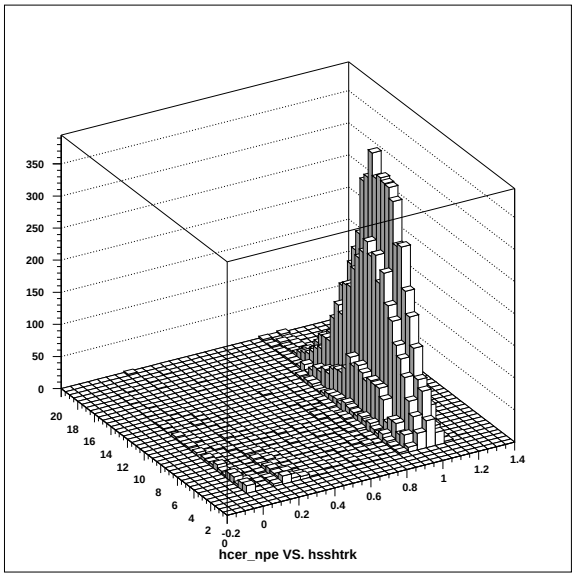

Figure 3-16: Calorimeter energy vs. the number of photo-electrons in the Čerenkov detector. The electrons are clearly visible as the large peak around hsshtrk= 1.

3.6 Electronics

3.6.1 Trigger

In most scattering experiments, the process of interest is only one of many possible types of events that can fire the detectors. Besides the inefficiency of recording data that are not of interest in the experiment at hand, there is often a more practical reason not to record all events, and that is because the deadtime increases with the event rate. Deadtime is the period during which the data acquisition system is unable to accept new events because it is busy recording the previous event. It is desirable to minimize deadtime so that the correction factor is not too large in order to minimize the uncertainty due to the correction (see section 4.1.2 for a detailed discussion on computer and electronic deadtimes). In this experiment the data acquisition system was limited to ≈ 3 kHz when the deadtime was kept $< 20\%$ using a prescale factor. To keep the event rate as low as possible, it was necessary to distinguish those events that are good from those that are bad before writing the event to storage. This was done by forming a combination of logic signals that indicated when a particular set of detectors fired, and using that combination to decide whether or not to record

the event. It was necessary to optimize a given trigger for rejection and efficiency. A trigger that was too loose would allow too many background events, resulting in unnecessary dead-time due to writing events that would eventually be thrown away. A trigger that was too strict would reject some events from the process in question. This section outlines the structure and use of the HMS trigger.

The HMS trigger system can be considered in two components, one coming from the hodoscopes, and one from the combination of signals from the Čerenkov and the calorimeter. The '`SCIN`' trigger (also known as '`3/4`') from the hodoscopes was the most basic trigger used in the experiment. This trigger was satisfied if there was a hit in three of the four planes of hodoscopes, and therefore could be satisfied by any charged particle. A plane was declared hit if at least one tube on each end of the plane fired. Fig. 3-17 shows a schematic view of the HMS trigger used in E03-103.

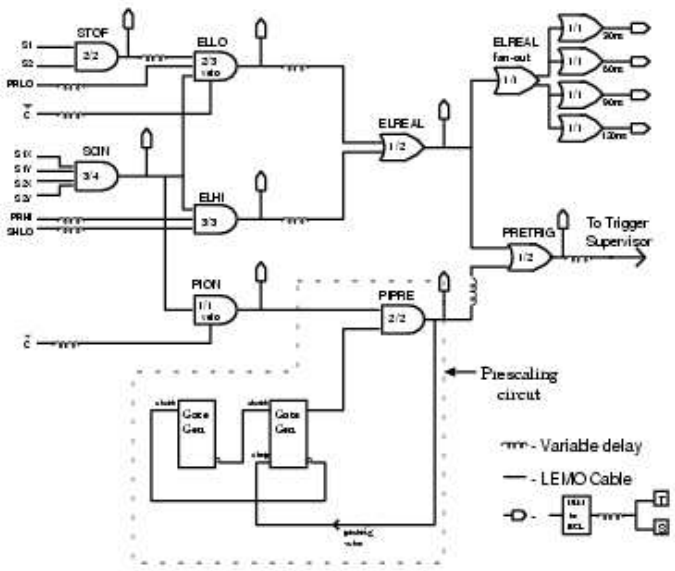

Figure 3-17: The HMS Trigger.

Two other triggers were formed to reject hadrons. To maintain efficiency, a hit in either the Čerenkov or the calorimeter was sufficient for the event to be recorded. `ELREAL` required that three of four scintillator planes fire, and that there was a sufficiently large signal in either the Čerenkov or the calorimeter. There were two different branches to `ELREAL`, one dominated by hits in the Čerenkov and one dominated by

hits in the calorimeter. The ELLO branch of the trigger requires SCIN and a hit in the Čerenkov. In detail, it requires both a hit in the a Čerenkov and a 2/3 coincidence among the SCIN, STOF and PRLO signals. STOF is a requirement that at least one scintillator plane in the front and one plane in the back fired, and is satisfied any time SCIN is satisfied. PRLO is a requirement that some energy (low threshold) was deposited in the first layer of the calorimeter. The ELHI branch requires good hits in the scintillator planes and the calorimeter. It is satisfied with a threefold coincidence among SCIN, PRHI and SHLO. PRHI is a requirement that some energy was deposited in the first layer of the calorimeter (high threshold), and SHLO is a cut on the total energy deposited in the calorimeter.

If either ELLO or ELHI is satisfied, then the event is labeled as an "ELREAL" event. These are events which are most likely good electrons. By pre-selecting events at the hardware level, we reduce the dead-time that would result from recording many non-electron events.

In addition to the ELREAL events, a small sample of events requiring only a SCIN trigger were also recorded. These triggers were then pre-scaled by a dynamical pre-scaling circuit so that only a few of these events were recorded as compared to the ELREAL events. These triggers constitute a sample of events unbiased by particle identification requirements and were useful for studying electron efficiency and pion rejection in both the Čerenkov and the calorimeter. Each trigger signal was fed to a TDC and read out by the data acquisition system. This made it possible to select a given trigger type by cutting on the TDC for that branch. In addition, the number of pre-triggers for each trigger type were recorded. This made it possible to calculate the computer dead-time for each trigger branch.

3.6.2 Data Acquisition System

Both online run-control and the readout of data were performed by the CEBAF Online Data Acquisition (CODA) software. Three distinct types of data were recorded for each run: the TDCs and ADCs for the various detectors are recorded on an event-by-event basis; scalers for beam position, charge, etc. were read out every two seconds;

and EPICS data from the slow controls were read out every 30 seconds. The ADCs, TDCs and scalers were located in FASTBUS and VME crates which had their own Read Out Controller (ROC) CPUs. The data from the ROCs were read out over a fiber-optic network.

The ADCs and TDCs were read out for each event in the data stream. The ADCs and TDCs are sparsified (only non-zero signals are recorded), which not only saves data storage space, but also shortens the time required to write the data for the event. The ADCs are sparsified by requiring that the signal be larger than some threshold. The threshold was typically set about 15 channels above each channel's pedestal. The pedestals were measured by recording 1000 pedestal events at the beginning of each run. These pedestal events were used during online replay to detect fluctuating pedestals and to change the threshold when necessary. TDC channels that did not receive a STOP were not recorded.

Chapter 4

Data Analysis

We now have a clear motivation for measuring the EMC effect in light nuclei. We also have the details of the detectors and equipment necessary to measure the inclusive cross section. It is now necessary to discuss how a physical observable, like the cross section, is extracted from scattering data. There are several steps in this process, and this chapter will cover the steps in detail with emphasis on the particular challenges faced in this analysis.

The process of extracting the cross section begins with counting particles for some period of time and converting the number of counts into a meaningful number by applying the necessary correction factors and normalization. Therefore we begin with a discussion of how events are filtered and the number of counts corrected to form the normalized data yield. We then move on to explain how this normalized yield is corrected for lost events from detector and trigger inefficiencies, and for background events. Finally, we will show how the data yield is converted to a cross section. This process involves forming a simulated yield that is analogous to the data yield and is used to account for the acceptance of the detector, and to incorporate corrections for physics effects like the change in the cross section due to the Coulomb field of the nucleus and radiative corrections. Each of these steps will be described in detail in the sections below.

There are three main pieces that go into the cross section. The first is the data yield, Y_{data}, which is the number of counts, properly normalized and corrected for

efficiencies and deadtimes in the spectrometer. The second is a measure of the phase space volume subtended by the detector. In this analysis, this quantity is measured using a Monte Carlo simulation of the detector. The third piece is a cross section model which is used to make corrections to the data, including the variation of the cross section over the acceptance, Coulomb and radiative corrections. The simulation and model are used together to form a simulated yield, Y_{sim}. The inclusive electron scattering cross section at E' and θ is extracted by combining these three pieces:

$$\frac{d\sigma(E',\theta)}{dE'd\Omega} = \frac{Y_{data}}{Y_{sim}} \cdot \frac{d\sigma^*(E',\theta)}{dE'd\Omega}, \tag{4.1}$$

where the asterisk indicates the model cross section. The simulated yield includes the features of the detector acceptance and the model radiated cross section. It serves as a normalization to the data yield, which is an integral over an E',θ bin, relative to the value of the cross section at the center of the bin. The next few sections describe the details of how these factors are formed, followed by a discussion of how the cross section is corrected for effects arising from the electron's interaction with the Coulomb field of the nucleus. Finally, the details of extracting the ratio of structure functions from the ratio of cross sections is discussed. Note that everywhere in this chapter, the shorthand $\sigma(E',\theta)$ will be used to denote the differential cross section $d\sigma(E',\theta)/dE'd\Omega$.

Before launching into the discussion, it is worth discussing the kinematic range covered in the experiment. Fig. 4-1 shows the range in x_{Bj} and Q^2 covered by E03-103. The DIS region is commonly defined as $W^2 > 4(\mathrm{GeV})^2$ and $Q^2 > 4(\mathrm{GeV/c})^2$. In this regime the scattering cross section is directly related to the quark distributions via the structure functions F_2^A. However, many of the data in the present experiment were taken at kinematics below these traditional cut-offs and lie in the resonance and quasielastic scattering regime. This feature poses some interesting challenges when comparing our data to higher energy experiments, but it also provides a unique opportunity to study the EMC effect in these regions. In particular, it is an opportunity to examine the scaling of the structure functions, and the scaling of the structure of

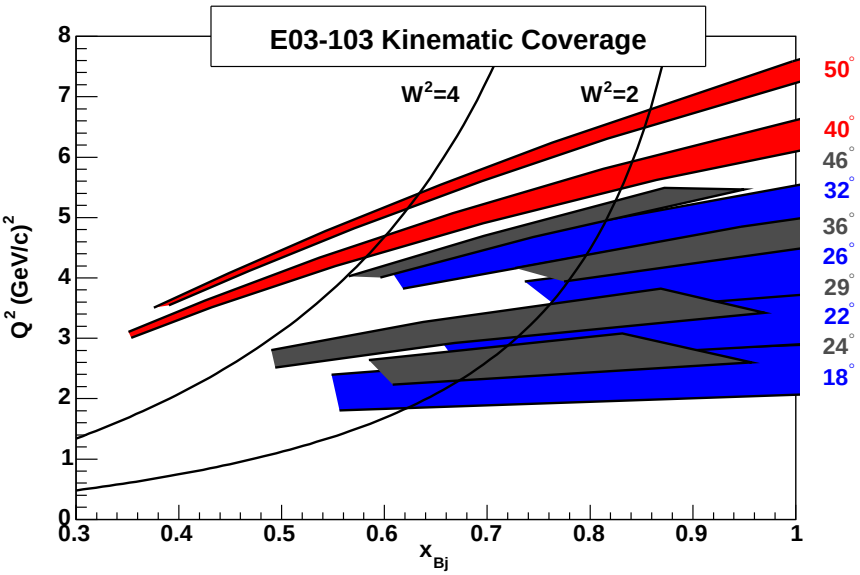

Figure 4-1: Kinematic coverage of E03-103. The red bands show the two angle settings that were used for the extraction of the cross section ratios presented in Ch. 5 The blue and gray settings are used to study the x_{Bj} and ξ-scaling of the structure functions in Q^2. The blue bands were taken at a beam energy of 5.77 GeV, and the gray settings were taken at a beam energy of 5.01 GeV. Contours of constant invariant mass squared are shown for $W^2 = 2$ and 4 $(\mathrm{GeV})^2$(Note that the units on $W^2$are suppressed in the figure for clarity. Also, data were only taken on deuterium and carbon at the settings shown in gray.)

the structure function ratios of different nuclei in the resonance region. Some details of the different challenges posed by these kinematic regions will be discussed in the final section of this chapter.

4.1 Data Yield

The properly normalized data yield represents the integral of the physics cross section over the available phase space volume:

$$Y_{data} = \int dE' d\Omega \left(\frac{d^3\sigma}{dE' d\Omega} \right) A^2(E', \theta), \tag{4.2}$$

where the acceptance function, A^2, accounts for the non-uniform response due to the geometric apertures in the experiment. This equation illustrates the basic goal of a

scattering experiment. It is to use some number of particle counts, Y_{data}, detected over some finite region of phasespace, to extract the differential cross section at a particular point within that phasespace volume. The yield is formed from the raw number of electrons counted in the detector, corrected for various detector effects, and normalized to the integrated luminosity. It can be written schematically as

$$Y_{data} = \frac{NC}{L}, \tag{4.3}$$

where N is the total number of particles counted, C is a correction factor that includes all deadtimes, detector efficiencies and other effects, and L is integrated luminosity. The next three subsections describe how each of the factors in Eq. 4.3 are formed.

4.1.1 Counting Particles

The primary measurement in a scattering experiment is the total number of particles detected for the process under study. Acquiring this number means finding all good events and and rejecting all unwanted events from background sources. N is the number of recorded events which pass all the cuts we place on the data. The cuts are chosen so that they select, as well as possible, only electrons and reject all other particles. The number of events was pre-filtered by the trigger as discussed in Sec. 3.6.1. Here we discuss the various cuts made at the software level. These cuts include selections based on trigger type, the geometrical acceptance of the detector stack, particle identification, and kinematic quantities.

Cuts are placed on the spectrometer quantities δ, y'_{tar}, and x'_{tar}. These cuts limit the acceptance of the spectrometer to ensure that only particles that originated from the target region are accepted, and to limit the acceptance to the region where the optics matrix elements are well-fit. The acceptance cuts are also used to define the acceptance in the Monte Carlo simulation. Since we take ratios of the data yield to the simulated yield to extract the cross section, it is crucial that the acceptance cuts pass the same fraction of events in both the analysis and simulation. Figs. 4-2 through 4-4 show the distribution of events for the data compared with the distribu-

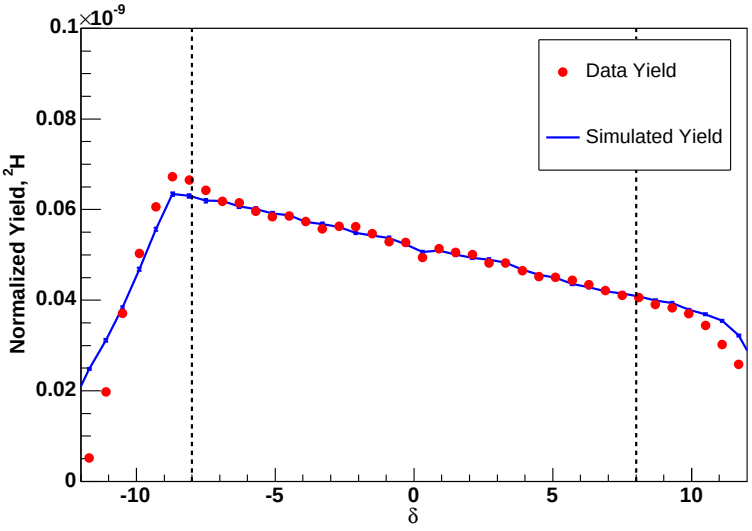

Figure 4-2: Data to Simulated yield comparison for δ for an extended target. δ is the relative deviation from the central momentum of the HMS in percent.

tion in the simulated yield for an extended target (deuterium). Note that no relative normalization has been applied to the two data sets. The behavior at large values of $\pm\delta$ is due to the limitation of the fitting matrix in that region. There is a slight dip at $\delta = 0$ due to and inefficiency in the central region of the Čerenkov where the edges of the two mirrors overlap. This feature is corrected for in the cross section by building it into the simulation as shown. The excess events in y'_{tar} and x'_{tar} are from events that scatter into the acceptance when scraping the edge of the collimator and are removed with the cuts. The cuts used are shown in table 4.3. The momentum acceptance of the HMS is well known only between $\delta = \pm 8\%$. Beyond this range, there are few events and the optics matrix elements are not well-fit. The in-plane angle (y'_{tar}) covers a range of ± 35 mrad and the out-of-plane angle (x'_{tar}) covers a range of ± 75 mrad. This angular acceptance is larger than the collimator, and therefore allows the collimator to define the acceptance.

A second set of cuts is placed on the particle identification information discussed in sections 3.5.1 and 3.5.2. The cuts are placed at 1.5 photoelectrons in the Čerenkov, and $E_{dep}/E_{track} = 0.7$ in the calorimeter. The quality of these cuts is discussed in detail in section 3.5.1. Finally, a cut is made on the trigger type. During the exper-

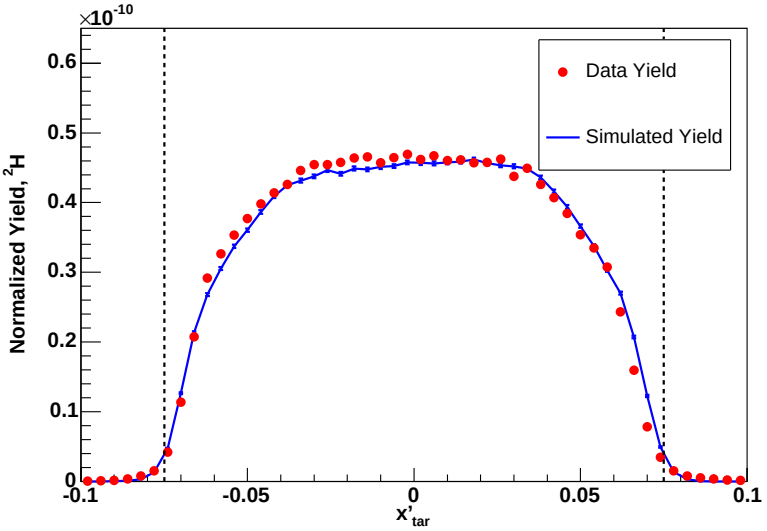

Figure 4-3: Data to Simulated yield comparison for x'_{tar} for an extended target.

Acceptance cuts
$-8 < \delta < 8$
$-0.075 < x'_{tar} < 0.075$
$-0.035 < y'_{tar} < 0.035$

Table 4.1: Acceptance Cuts. δ is the relative deviation from the central momentum of the HMS in percent, x'_{tar} is the out-of-plane angle and y'_{tar} is the in-plane angle.

iment there were two trigger types recorded. The main trigger used for analysis is called `ELREAL` and includes the `3/4` trigger and some additional particle identification information from the Čerenkov and the calorimeter. The other trigger is a prescaled version of the `3/4` trigger. The `3/4` triggers were recorded in order to acquire unbiased information on the pion rejection and electron efficiency of the Čerenkov and the calorimeter. Since the computer deadtime depends on the trigger type, the deadtimes were calculated explicitly for each trigger type by counting the number of recorded compared to the number of pretriggers. In order to ensure that the proper deadtime was used to correct the data, a cut was placed on the trigger type. The trigger signal was fed into a TDC channel, and a cut was placed on that channel, so that only `ELREAL` events were used in the extraction of the cross section.

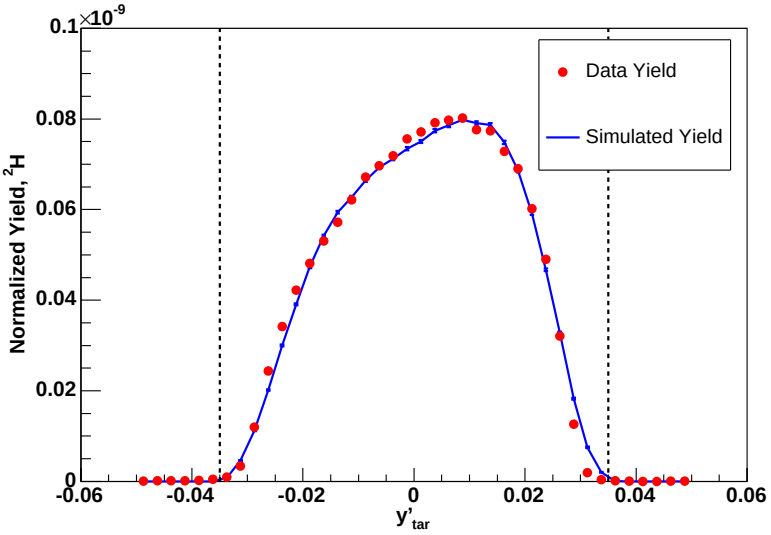

Figure 4-4: Data to Simulated yield comparison for x'_{tar} for an extended target.

4.1.2 DAQ and Detector Efficiencies

The yield above must be corrected for losses that occur in the detector and data-acquisition systems. The main sources of lost events are inefficiencies in the trigger and tracking systems, dead-time due to a busy data-acquisition system, and finally inefficiencies in the particle identification cuts. The correction factor is

$$C = \frac{P}{\epsilon_{trig}\epsilon_{track}\epsilon_{det}t_{comp}t_{elec}} \tag{4.4}$$

where P is the prescale factor, used to reduce the trigger rate when data is taken, ϵ_{trig} is the trigger efficiency, ϵ_{track} is the tracking efficiency, ϵ_{det} includes corrections for global detector inefficiencies, t_{comp} is the computer livetime, and t_{elec} is the electronic livetime. Each of these factors is described in the sections below.

Electronic and Computer Deadtime

Events arrive at the HMS Poisson distributed in time. For a mean particle rate R, the probability that n events will arrive during a time t is

$$P(n) = \frac{(Rt)^n e^{-Rt}}{n!}, \tag{4.5}$$

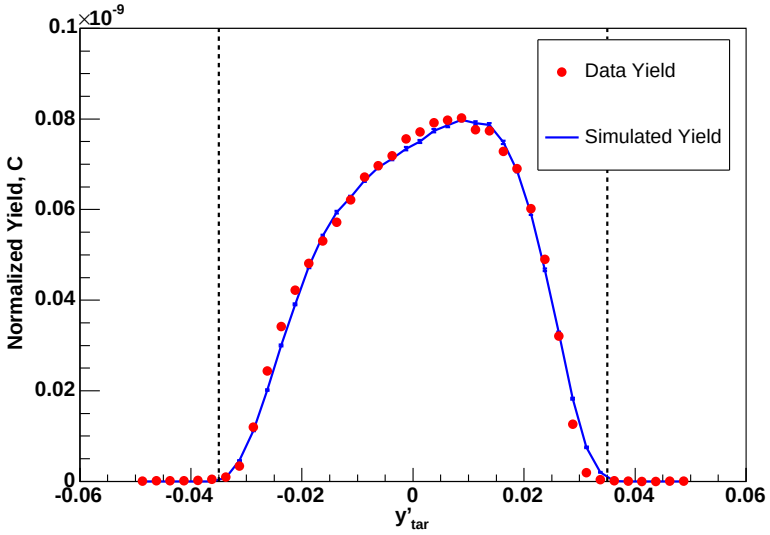

Figure 4-5: Data to Simulated yield comparison for y'_{tar} for a point target.

and the probability distribution for the time between events is

$$P(t) = Re^{-Rt} \tag{4.6}$$

When a trigger is produced, a logic gate goes high for some time τ. The deadtime in the HMS is non-extendable, meaning that if any events arrive while the gate is high, they will be ignored. The livetime, t_{live} is defined as the fraction of events recorded out of the total number that arrive at the detector stack, and is given by the number of events for which the time between events is greater than τ

$$t_{live} = \frac{N_{detected}}{N_{total}} = \int_{\tau}^{\infty} Re^{-Rt} d\tau = e^{-R\tau}. \tag{4.7}$$

In E03-103 the maximum event rate at the hodoscope planes was $\leq$ 1MHz. The gatewidths in the logic modules were 40 ns, except the hodoscopes discriminators whose width was 50 ns. The signals from different hodoscope planes could come up to a few ns apart, causing the trigger gate to stay high longer than the 50 ns gatewidth of the hodoscope discriminators. The variation in the arrival time among the hodoscope planes would therefore cause a variable effective gatewidth with a range from 50 ns to 60 ns. In order to keep a constant gatewidth, the pretrigger gate was

set to 60 ns. The pretrigger gate is the logic pulse that stays high when a trigger is satisfied. At the trigger rates in E03-103, the electronic deadtime was very small and could be approximated by

$$t_{dead} = 1 - t_{live} = R\tau, \tag{4.8}$$

where τ is the trigger gatewidth. The electronic deadtime was then a linear function of the gatewidth. The deadtime was measured by recording a subset of triggers at two different gatewidths in addition to the data recorded at the nominal gate width. The counts at the two different gatewidths are used to extrapolate to zero deadtime. The electronic deadtime was given by

$$\tau_{dead} = \frac{N_{lost}}{N_0} = \frac{N_0 - N_\tau}{N_0} = \frac{(N_1 - N_2)}{N_0}\frac{\tau}{(\tau_2 - \tau_1)}, \tag{4.9}$$

N_1 and N_2 were 100 ns and 150 ns, respectively. For convenience, N_1 was used in the denominator instead of N_0 since N_1 was counted directly. Given the very small deadtimes in this experiment, this was an excellent approximation. The electronic deadtime is always $< 0.1\%$, and this approximation is good to 0.01%. The deadtime is computed for each run using the counts from these two gates. Counts are recorded at these gate widths every 2 s during the run.

The more significant source of deadtime is the speed at which the data acquisition system can record event data. While data are being written, the system cannot accept new events. The time required to write an event's data to storage is about 350 μs and so the computer deadtime will become significant at much lower rates, reaching 10% at about 1 kHz. This effect is partially mitigated using a prescale factor to ignore some fraction of good triggers.

The computer livetime was calculated for each run using the total number of pretriggers for the run, the prescale factor for the run, and the total number of triggers recorded. The computer livetime is

$$t_{comp} = \frac{N_{trig} \cdot P}{N_{pretrig}}, \tag{4.10}$$

where N_{trig} is the number of triggers processed by the trigger supervisor, P is the prescale factor, and $N_{pretrig}$ is the number of good triggers sent to the trigger supervisor. The computer deadtime is always the dominant form of deadtime in the system, and therefore the prescale factor was adjusted as needed to keep deadtime below 10%.

Trigger Efficiency

Events are also lost due to inefficiencies in the detectors themselves. The combined inefficiencies in the scintillators and PID detectors could result in the inability to form a trigger when a good electron passed through the spectrometer. The trigger diagram is shown in Fig. 3-17. The scintillator planes form the first level of the trigger. The efficiency for each hodoscope is calculated using tracks that point at the center of the planes. The total number of tracks that caused a hit in the paddle divided by the total number of tracks that passed through the paddle gave the efficiency. The total plane efficiency was also computed using the other three planes. The per-plane efficiency was the fraction of times that a hit was registered on the plane when there was a hit in each of the other three planes. The `3/4` trigger required only three out of the four planes to register a hit and was therefore its efficiency was usually very high. The trigger efficiency was computed for each run and found to be constant at $(99.7 \pm 0.05)\%$ at all settings so a single efficiency of 0.997 was applied to all runs.

The PID legs of the trigger require that either the Čerenkov or the calorimeter register a good hit. Since the particle identification cuts applied in the analysis are stricter than the trigger requirements, we use only the `3/4` efficiency to correct for lost triggers. (There are efficiencies related to the cuts used in the analysis, however. The correction for these factors is discussed in Sec. 4.2.2.

Tracking Efficiency

In addition to satisfying the trigger, a good event must also have enough information to form a good track in the drift chambers. In order to form a track, there must be enough wires hit so that the left-right ambiguity can be resolved. But if there are too many hits then the tracking algorithm is slow trying to choose among the

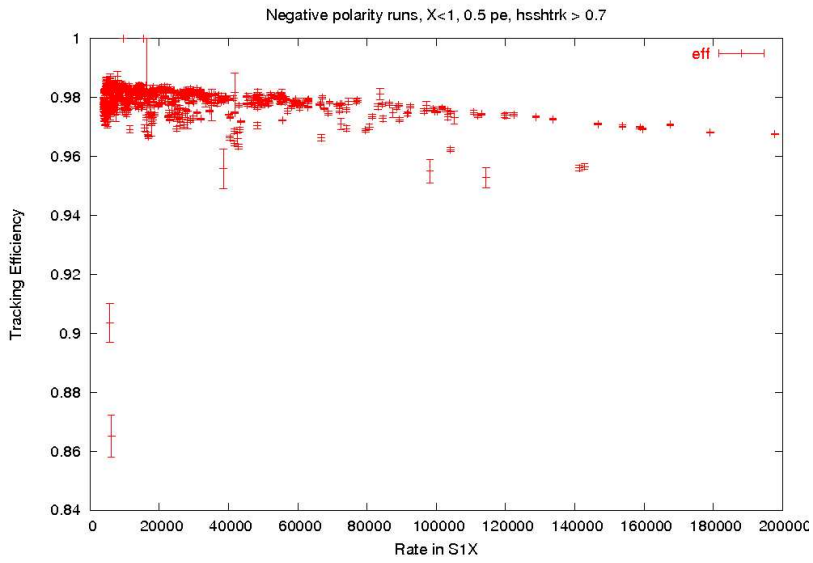

Figure 4-6: HMS tracking efficiency for electrons.

possible tracks. Events with many hits are, therefore, thrown out due to the liklihood that they are due to noise hits on the wires. The tracking efficiency is defined as the number of good tracks formed divided by the number of good events that should have formed a track. An event is designated good if it passes the trigger, has the right time of flight (forward going) and has less than 15 hits in one of the chambers. Events with 15 or more hits in each chamber are assumed to be due to electrons scattering from the magnet edges, causing a shower of particles. These events are lost due to the geometrical acceptance and should were not included in the calculation of the tracking efficiency.

Several versions of the tracking efficiency are calculated. The efficiency for electrons and hadrons is different, so events with a large pion fraction will be biased toward the pion efficiency. We want to correct only for the electrons lost in the tracking, and so we compute the tracking efficiencies for the various cases. The efficiency is computed for all events; events which pass a particle ID cut; events passing through a fiducial region in the hodoscopes; and events which pass both the fiducial and PID cuts. The tracking efficiency used in this analysis includes the fiducial and particle ID cuts. The events that should form tracks are defined as those events which fire both the Čerenkov and the calorimeter (> 1.5 photoelectrons, and deposited energy

$> 0.7 \times p_{track}$ respectively; have hits in the central region of the scintillator planes; and have $\beta > 0$ (forward going particle). The number of events that satisfies these conditions and has an associated track at the focal plane, gives the number of good tracks. The tracking efficiency as a function of total particle rate at the chambers is shown in Fig. 4-6. The fiducial electron tracking efficiency is very high, between 97% and 99%, depending on the particle rate in the spectrometer. The efficiency is calculated for each run and the yield for each run is corrected for the corresponding efficiency. We assign a scale uncertainty of 0.5% to the cross section, due mostly to the uncertainty associated with throwing out tracks with > 15 hits per chamber.

4.1.3 Background Sources

Even with an efficient trigger system, and cuts designed to select only electrons from our data sample there are still unwanted backgrounds that must be removed from the data. Both pions and electrons contribute significant backgrounds. There are two significant sources of background electrons. These are the electrons that scatter in the cryotarget cell walls and the electrons that arise from pair production in the target after the beam electron emits a Bremsstrahlung photon. The next subsections describe how these events are removed from the data sample. The subsequent section describes how the pion background is estimated.

Charge-Symmetric Background

Electrons may radiate high energy photons in the target which go on to produce electron-positron pairs. These electrons can scatter into the detector stack resulting in a sizeable background. In this background process the electrons and positrons are produced in equal numbers, so the background yield is charge-symmetric. Since pair-production is the dominant source of positron production, a measurement of the positron yield gives a direct measurement of the electron background from pair-production. The HMS was run at reverse polarity for each target and at each kinematic setting where the background was was large ($32^\circ, 32^\circ$, and 50°).

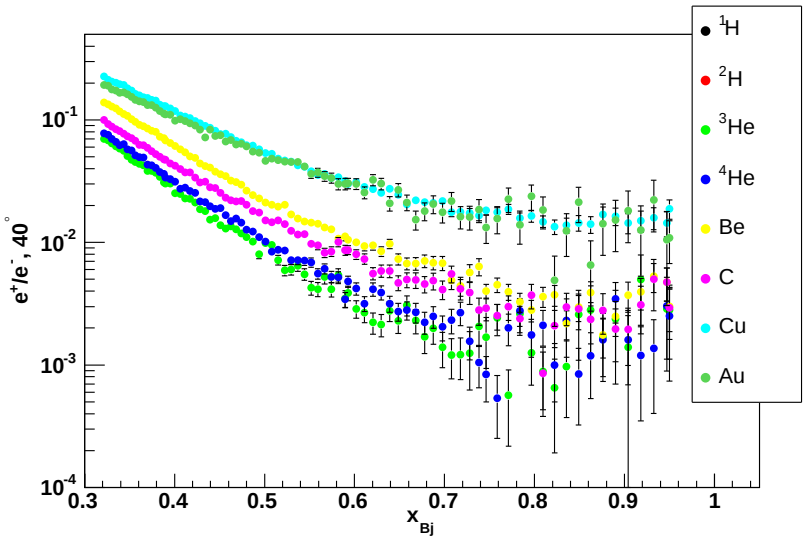

Figure 4-7: Charge Symmetric Background at 40° as a function of HMS momentum. x_{Bj}= 0.6 corresponds to $p_{HMS} = 1.7$ GeV/c. The background for the lighter targets is relatively low at $\approx$ 10%. Only the thickest (in radiation lengths) targets have a large background at the lowest momentum.

The positron sample is subjected to the same set of cuts as the electron sample and the relative yields are used to construct the e^+/e^- ratio, R,

$$R = \frac{e_+}{e_-} = \frac{b_+}{S_- + b_-}, \tag{4.11}$$

where $b_{+/-}$ represents the normalized yield from background sources and S_- represents the normalized yield of signal electrons from electron-nucleus scattering. It is important to note that when running the HMS at positive polarity the total rate in the spectrometer is much higher than at negative polarity due to hadrons. These higher rates required a tighter trigger in order to keep the computer deadtime low. This tighter trigger, `ELCLEAN`, is similar to the standard electron trigger, `ELREAL`, but requires a hit in *both* the Čerenkov and calorimeter. To ensure that the positron to electron ratio is computed correctly, we applied the same trigger to the electron data (both triggers were present for the electron data, but only `ELCLEAN` triggers were present for positron data) to measure an `ELCLEAN` electron yield e^-_{elc}. Then, since the background is charge symmetric, we set $b_- = b_+$, and extracted the corrected electron

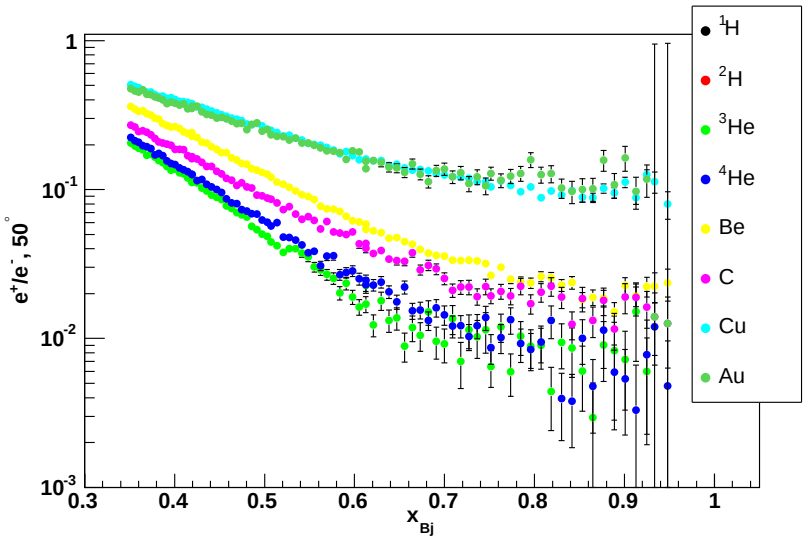

Figure 4-8: Charge Symmetric Background at 50° as a function of HMS momentum. x_{Bj}= 0.6 corresponds to p_{HMS} = 1.25 GeV/c. This figure illustrates the that the background can be very large for the largest angles. In this case, the ratio of background to the total yield is as high as 50% for the thicker (as a fraction of radiation lengths) targets. This means that the signal and background are about the same size.

yield:

$$e^-_{cor} = e^-_{elr} \cdot \left(1 - \frac{e^+_{elc}}{e^-_{elc}}\right). \tag{4.12}$$

Aluminum Target Cell

The cryogenic liquid for the cryotargets was stored in an aluminum cell with a wall thickness of $\approx$ 0.12 mm. The cell was made of Al 7075, which has a density of $\approx$ 2.8 g/cm^3. This corresponded to a target thickness of 2×0.034 g/cm^2 which was approximately 10% of the thicknesses of the cryotargets which ranged from 0.3 to 0.7 g/cm^2. Since the entire target was visible to the spectrometer, these events contributed up to 10% of the total counts. This background was measured directly by taking data on a dummy target cell at each kinematic setting.

The dummy target had approximately the same effective geometry as the aluminum cell at the beam intersection. It was comprised of two flat aluminum plates separated by 4 cm. These plates were approximately 8 times thicker than the actual cell walls. This allowed for much quicker data collection time, but had to be taken

Target	Loop	t_{dummy}/t_{cell}
^{1}H	2	7.803 ± 0.146
^{2}H	3	7.873 ± 0.147
^{3}He	2	7.803 ± 0.146
^{4}He	1	7.069 ± 0.135

Table 4.2: Dummy to Cell-Wall ratio. This table lists the loop number used for each target and the corresponding ratio of the dummy target thickness to the actual cryotarget cell-wall thickness.

into account when the dummy data were used to subtract the cell wall background from the cryogenic target data. The ratio of dummy to cell-wall thickness is shown for the four cryogenic targets in Tab. 4.2. The ratio was measured to a precision of about 2%, resulting systematic uncertainty of 0.2% to the total cross sections for the cryogenic targets.

The same cuts and corrections were applied to both sets of data, and the normalized yield (corrected for charge-symmetric background) from the dummy target was subtracted from the cryogenic target yield so that only the events arising from within the target material remained. This procedure is illustrated in Fig. 4-9 which shows the distribution of detected events in y_{tar}. The two peaks in the green histogram clearly show the two panels that comprise the dummy target. An important feature of this plot is the fact that,due to the resolution in event reconstruction, some events from the cell walls were reconstructed to all points in the target. This meant that it was not possible to use a simple spatial cut to remove the events originating from the cell walls, and it was necessary to use the data from the dummy target to subtract the background from the cell walls. A final complication is the fact that the dummy target is comprised of two flat plates which are transverse to the beam direction. The target cell is round so that particles traverse approximately the same thickness of aluminum, regardless of scattering angle. However, the thickness traversed for events originating from the dummy target will traverse a different thickness depending on the scattering angle. This means that the energy lost due to external radiative corrections will depend on the scattering angle. A correction was applied to the dummy data prior to subtracting it from the cryotarget data. The correction was computed from

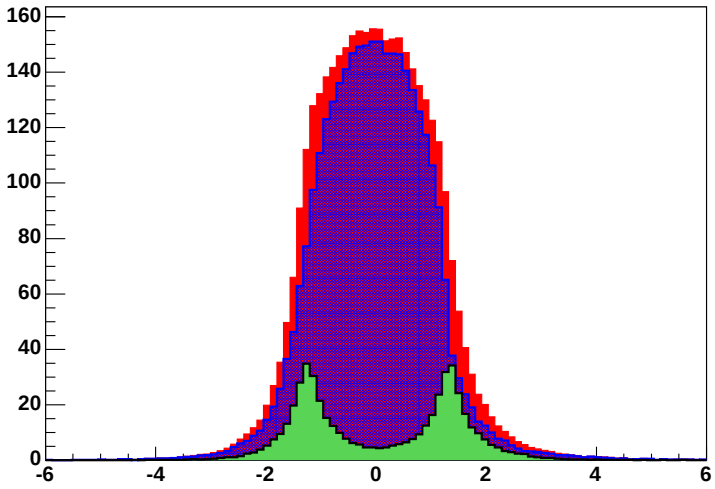

Figure 4-9: y_{tar} distribution. The red histogram shows the y_{tar} distribution for a ^{4}He setting before the dummy target is subtracted; the green histogram shows the distribution for the dummy cell; and the blue shows the ^{4}He events with the dummy subtracted (green histogram subtracted from the red histogram). In this case, the background events from the cell walls are estimated to be about 13% of the total number of events.

the model cross section. The correction was on the order of, and usually less than, 5% of the total radiative correction. Assuming, conservatively, that this number is known to 10%, this size of correction would add an additional systematic uncertainty of 0.1% to the cross section. Combining this with the dummy-to-cell uncertainty, we arrived at a total systematic uncertainty in the cryogenic yield of 0.22% due to the cell wall subtraction.

4.1.4 Pion Contamination

Another source of unwanted events are pions that pass both the Čerenkov cut and the calorimeter cut. Although the pion rejection in the Čerenkov is about $> 500:1$, some pions did fire the Čerenkov by producing knock-on electrons in the aluminum entrance window. These pions deposited, on average, ≈300 MeV in the calorimeter causing a second peak at lower deposited energy as shown in Fig. 4-10. The tail of this peak extends well beyond the nominal cut in the calorimeter at $E_{dep}/E_{track} = 0.7$

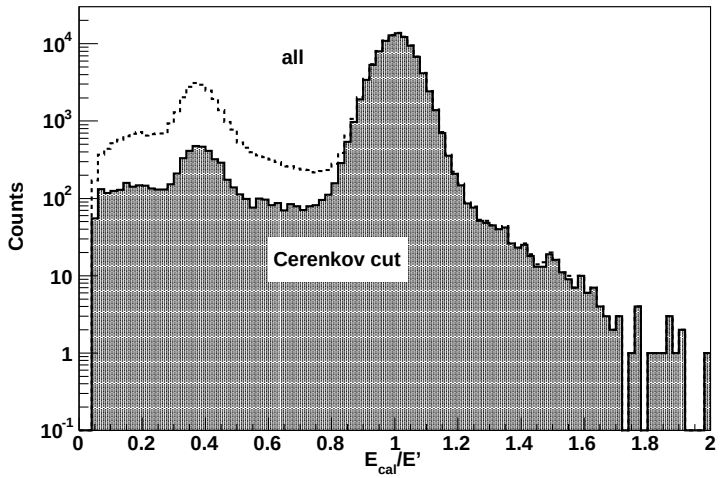

Figure 4-10: Energy deposited in the calorimeter normalized to the particle's momentum. The white histogram shows all events that pass the nominal acceptance cuts. The shaded histogram shows the events which also fire the Čerenkov. The electrons are sharply peaked at one, but there is a large pion background visible at low fractional energy. These events are mostly pions and the tail of the distribution extends under the electron peak, causing a background that can't be removed with simple particle ID cuts.

constitutes the pion background. This background can not be removed with any other detector cuts, and so it was important to estimate the size of the background and make the appropriate correction, if necessary.

To estimate the pion background, a strict set of cuts was used on the unbiased trigger sample to select a clean sample of pions, and the nominal set of cuts were used to select electrons from the standard triggers. The program was to select a set of electrons that represented the good electrons as defined in the data analysis, and then produce a pion spectrum the shape of which matched that of the residual pion background in the electron spectrum. By normalizing this pion spectrum to the background in the electron spectrum, the pion background was measured by integrating the number of events above the calorimeter cut. To avoid biasing the sample, care was taken to select events from the sample of trigger types that did not require calorimeter information. Electrons were selected from events which satisfied the trigger via a hit in the Čerenkov. Pions were selected from the unbiased triggers. Electrons were then defined as those particles with two or more photoelectrons in the

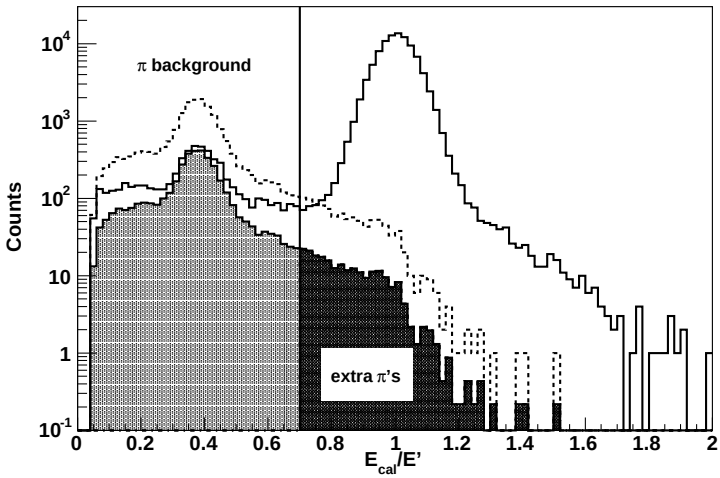

Figure 4-11: The pion background is estimated by matching the background to the spectrum of a pure pion sample. This pure sample is then scaled to match the height of the background at the peak, and the tail is integrated above the calorimeter cut. The peak is actually normalized such that the low energy electron tail plus the constructed pion peak match the background peak. The light shaded histogram above represents the constructed background, and the dark region represents the total number of pions that pass all cuts and constitute the pion contamination.

Čerenkov, and pions were defined as events that left less than 1/2 a photoelectron in the Čerenkov. The resulting spectrum is shown in Fig. 4-11. Next, the pion peak is scaled so that it matches the pion background in the electron spectrum, and the tail of this scaled spectrum is integrated above the calorimeter cut. In the process of scaling the pion peak, care was taken to account for the electron tail below the cut. The dark shaded region in Fig. 4-11 indicates the excess pions in our electron sample.

The pion contamination was found to less than 0.5% for the largest π/e settings, and lower for other settings. Fig. 4-12 shows the pion contamination as a function of HMS momentum for all targets. Note that the pion background is also present in the positive polarity data used to measure the charge symmetric background. Since pion production is approximately charge symmetric, the pion background approximately cancels when the the positive polarity data are subtracted from the negative polarity data. Fig. 4-13 shows the relative difference between positive and negative pions, which is the real measure of the pion contamination. Since the pion contamination is so small in the background subtracted yield we made no explicit correction made

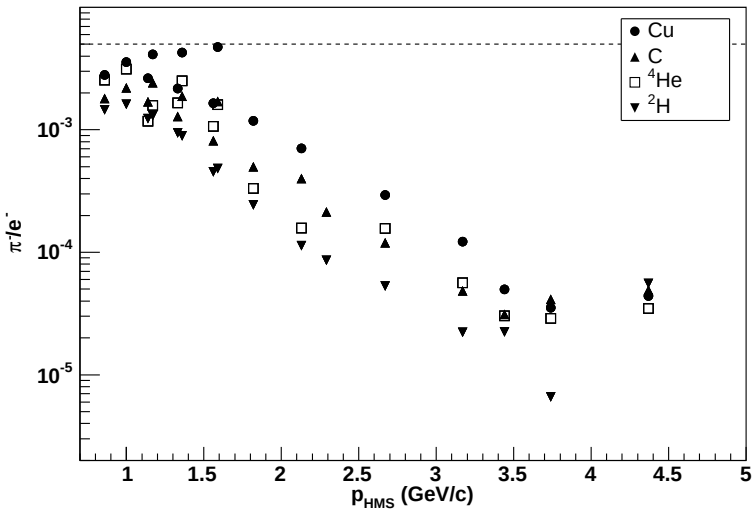

Figure 4-12: Pion contamination as a function of HMS momentum. This figure shows the ratio of pions to the sum of pions and electrons. The pions and electrons are counted as described above. The ratio is small for all targets, 0.5% at most. Only data for $x_{Bj} < 0.9$ are shown.

for the pion contamination. We estimate the relative uncertainty on the background itself at 50%. Therefore, we assigned a 0.2% systematic uncertainty to the cross section to account for the background for the low momentum settings, where the π/e ratio is largest, and 0.1% at the rest of the settings.

4.1.5 Target Boiling

The rastered electron beam deposited a current of 80μA and onto an area approximately 2×2 mm^2. The heat from the beam could cause local boiling very near the beam in the cryogenic targets. This boiling would change the density near the beam, and therefore would change the target thickness seen by the beam. In order to estimate the size of this effect, dedicated scans were made in which data were taken at several different beam currents for carbon and the four cryotargets. It was observed that the charge-normalized, corrected particle yield depended on the the beam current. Figs. 4.1.5 and 4.1.5 show the current dependent yield for ^{3}He and carbon. For cryotargets, the effect may be understood in terms of local boiling in the cryogen due to the electron beam. The solid targets, on the other hand, did not boil or melt

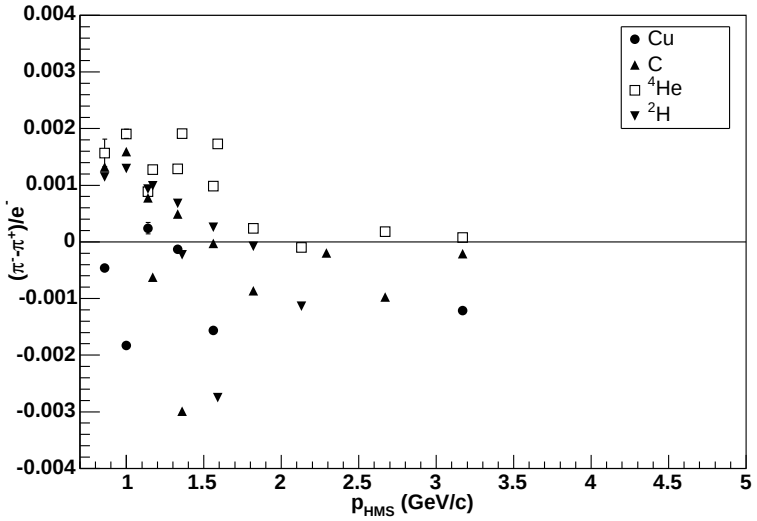

Figure 4-13: This plot shows the relative difference in the number of negative pions and positive pions. If we are correctly extracting the charge-symmetric background, then the number of π^+ should be equal to the number of π^-, and so the difference should be zero. It is clear that at low momenta we are slightly overestimating the positive pion background. However, the difference is very small, and so the total pion contamination remains at the 0.1-0.2% level.

at the currents used in the experiment. However, a drop in the yield was observed for the carbon target, which indicated that there was an additional effect that caused part of the current dependence in the normalized yield.

It was noted that an offset in the BCM calibration would cause an observable drop in particle yield. The particle yield was normalized to the delivered charge:

$$y' = \frac{N}{Q} = \frac{N}{I\Delta t}. \tag{4.13}$$

where I is the beam current computed from the BCM calibration. If this number was different from the true beam current due to a drift in the BCM calibration, for example, then the true beam current would be related to the measured current by $I_{true} = I + \Delta I$, and the actual normalized particle yield would be

$$y' = \frac{N}{Q} = \frac{N}{(I + \Delta I)\Delta t}. \tag{4.14}$$

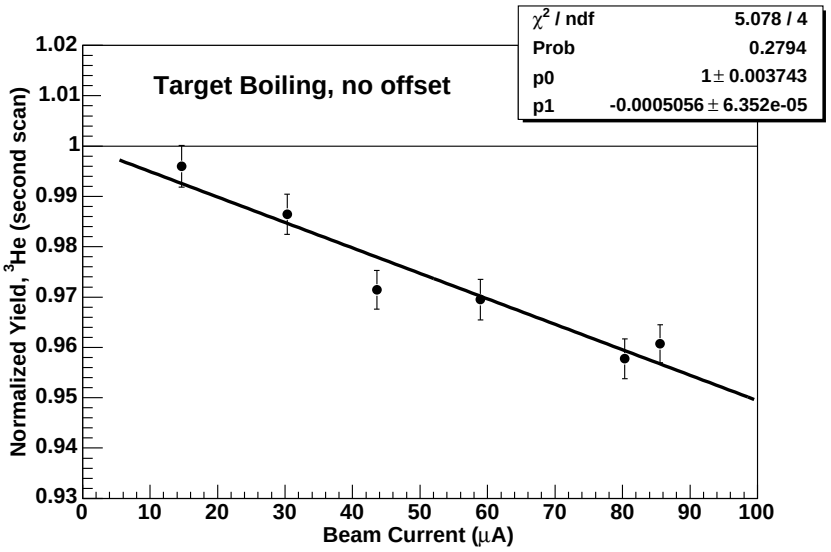

Figure 4-14: Normalized Yield vs. Beam Current for ^{3}He. The dependence of the normalized yield on current in a cryogenic target is interpreted as a reduction in the target density near the beam due to localized boiling. However, only part of the slope shown here is due to boiling. The rest is due a shifting offset in the BCM, which can be measured using the slope for carbon shown in Fig. 4.1.5.

Which means that the *measured* particle yield would be

$$y'_{measured} = y'_{correct}(1 + \Delta I/I). \tag{4.15}$$

So a measured reduction in the particle yield could be an indication that the BCM offset used was too large (that is, ΔI is negative). For all carbon scans, the measured yield dropped as a function of current. This effect was corrected by fitting the offset observed in the carbon scan and applying this offset to the cryotargets and recomputing the measured yields. Any residual slope in the beam-current scan was taken to be due to local boiling of the cryotarget, and the yields were corrected using the measured slope. Fig. 4-16 shows the result for one of the carbon scans taken during the helium running. The data were fit to a function of the form

$$y = \frac{a}{1 + b/I} \tag{4.16}$$

where b gave the current offset. The offset is given by p1 in the fit, and in this case

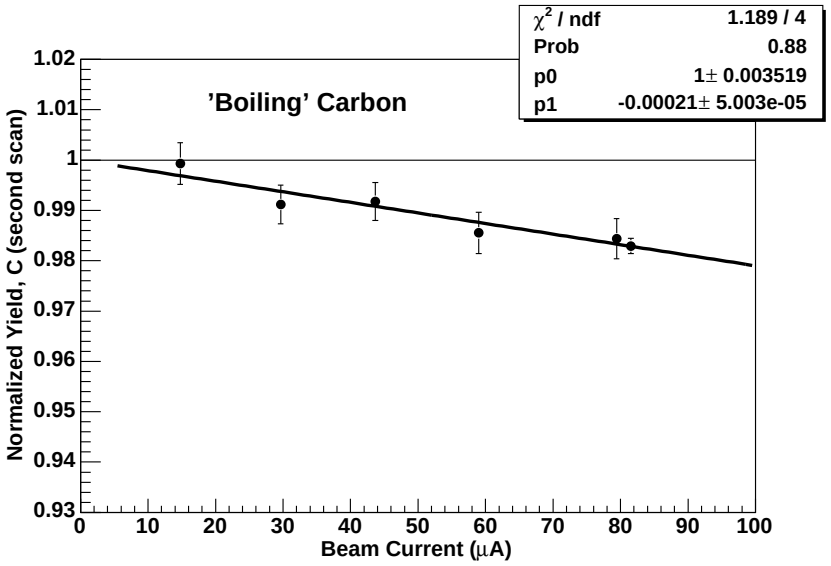

Figure 4-15: Normalized yield vs. Beam Current for carbon. The normalized yield from a solid target should not depend on the the beam current. The slope here is an indication of a shifting offset in the BCM.

the result is p1= -307 nA. This size of offset is consistent with the scatter seen in the BCM calibrations in Fig. 3-4. This offset was then applied to the cryotarget data and the residual slope was extracted as seen in Fig. 4-17 for helium. The slope and the offset could also be extracted directly from the cryotarget data by fitting the cryotarget data to a function of the form

$$y = \frac{a(1+cI)}{1+b/I}. \tag{4.17}$$

The offsets and slopes extracted in this way were consistent with the offsets and slopes extracted as described above. The data were corrected using the offsets calculated from the carbon scan to find the cryotarget slope versus current.

Neither the hydrogen nor the deuterium targets showed residual slopes after correcting for the BCM offset, but both helium targets showed boiling for all scans. The slopes for the separate scans agreed within the fit uncertainties and were averaged together to get the boiling correction. The measured slope was $(3.5 \pm 0.3)\%$ at 80 μA for ^{3}He, and $(1.5 \pm 0.2)\%$ at 80 μA for ^{4}He. The normalized yield for each run was corrected for this effect by multiplying the slope by the average beam-on current

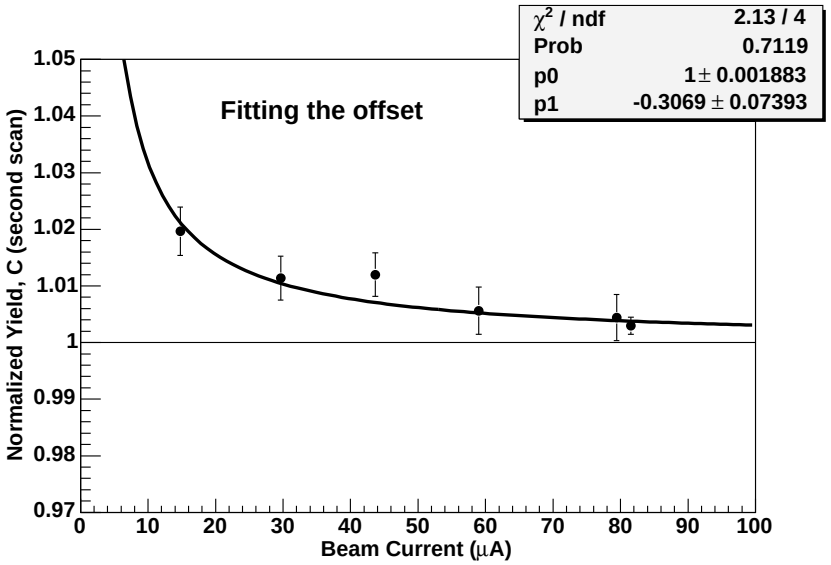

Figure 4-16: Corrected Yield vs. Beam Current for carbon. When the offset from Sec. 4.1.5 is applied, the normalized yield for carbon shows no real dependence on the beam current.

for the run. So the yield was divided by a factor $\tau_{cor} = 1 - m \cdot I_{beam-on}$ to correct for the change in the target thickness due to the current. This correction resulted in an additional systematic uncertainty of 0.5% in the cross section for the cryogenic targets. For the cross section ratios we estimate an uncertainty of 0.5% for the solid target to deuterium ratio and 0.6% for the cryotarget to deuterium ratio.

4.1.6 Normalization

The integrated luminosity, L, is the product of the time-integrated flux (total number of electrons incident on the target) and the target thickness (total number of target particles in the path of the beam). It is computed as

$$L = N_{electrons} \cdot N_{scatterers}. \tag{4.18}$$

The number of electrons delivered to the target is given by

$$N_{electrons} = Q/(1.602 \times 10^{-19}\text{C/e}), \tag{4.19}$$

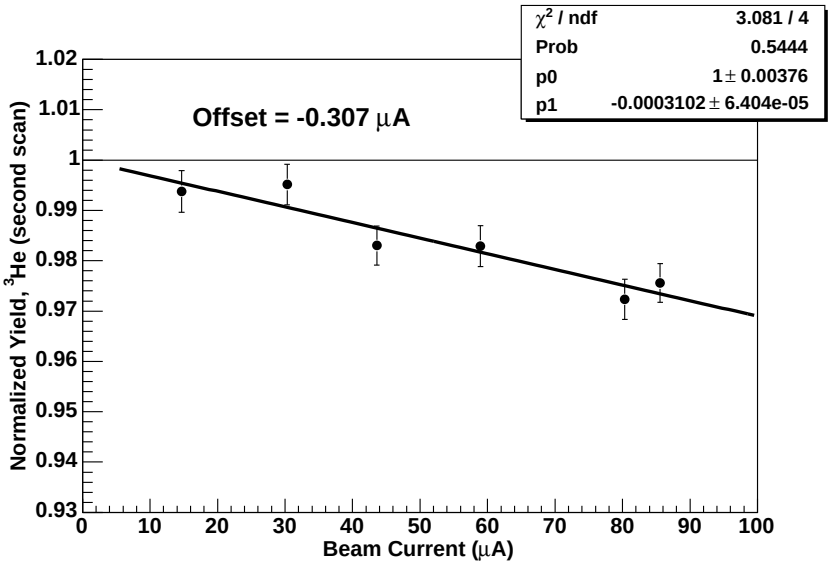

Figure 4-17: Corrected Yield vs. Beam Current for ^{3}He. This plot shows the residual slope after correcting for the BCM offset measured using the carbon scan. The slope above is the result of localized boiling in the target near the beam. A correction factor is applied for each run given by the slope and the average beam-on current for the run.

where Q is the total charge delivered, in Coulombs. The number of scatterers in the target is

$$N_{scatterers} = \mathrm{A} \cdot \frac{\tau}{m_{\mathrm{A}}}, \tag{4.20}$$

where τ is the target thickness in units of grams per cm^2, and m_{A} is the mass of the nucleus in grams. This gives the total number of nucleons per cm^2 in the path of the $N_{electrons}$ electrons that impinge on the target.

4.2 Simulated Yield

Counting the total number of particles in a detector is the first step in forming the cross section, but there are several other pieces that that are necessary in order to convert the normalized electron yield into a physics cross section. The next thing that must be done is to estimate the total acceptance over which the particles were detected, including the feature that the detector is not equally sensitive at all locations in the acceptance. The ratio of the counts to this effective phasespace volume gives

the average cross section over the acceptance. In order to convert this average cross section to the cross section at a particular point, one must account for the variation of the cross section across the acceptance. Finally, one must make a correction for radiative effects where the incoming or outgoing electron loses energy by radiating photons before or after the scattering event.

These effects are accounted for by building a simulated yield from a simulation of the detector acceptance where the events are weighted by the various correction factors described above and a model cross section. The motivation for using the simulated yield can be seen when the data yield is converted to a cross section. If Y_{data} is the normalized yield for a bin centered at E', θ, then the extracted cross section would be

$$\frac{d\sigma(E',\theta)}{dE', d\Omega} = \frac{Y_{data}}{(\Delta E' \Delta\Omega)_{eff}} \left(\frac{c_{BC} \cdot c_{rad}}{\epsilon'_{det}} \right), \tag{4.21}$$

where c_{BC} and c_{rad} are the bin-centering and radiative corrections respectively, and ϵ'_{det} is a factor that accounts for any position or kinematic dependent inefficiencies in the detector that are not related to the geometric acceptance, and so are not built into the simulation. $(\Delta E' \Delta\Omega)_{eff}$ is the effective phase space volume space for the bin over which the yield is collected. We next discuss the form of each of these corrections in detail, and then show how they are actually applied to the data in this analysis.

4.2.1 Acceptance Function

The acceptance function is the relative number of particles that are detected at each point in the phase space. It depends only on the geometry of the detector and not the physics cross section under study. In order to deduce the acceptance function, we performed a Monte Carlo simulation of the experiment at each kinematic setting. The simulation illuminated the HMS with electrons uniformly over the $x'_{tar}, y'_{tar}, \delta$ acceptance. If the detector response was uniform everywhere in the acceptance, then we would start by computing the cross section from the yield and the phasespace volume

$$\sigma' = \frac{Y_{data}}{\Delta E' \Delta\Omega}, \tag{4.22}$$

where σ' would then represent the average cross section over the acceptance. However, the detector is not equally sensitive everywhere, and some events are lost due to the various apertures (magnet entrances and exits, etc.) The non-uniform acceptance must be taken into account when calculating the effective phasespace volume since the particle yield will be biased toward the more efficient regions of the acceptance. The fraction of particles detected at a particular kinematic point, E', θ, ϕ, from a particular point in the target, $x_{tar}, y_{tar}, z_{tar}$, in general depends on all six of these variables. It is convenient at this point to examine the measured yield that would be detected in an experiment. The measured yield would be the integral over the phase space, where the cross section at each point is weighted by an acceptance function, A^6,

$$Y_{data} = \int dx_{tar} dy_{tar} dz_{tar} dE' d\theta d\phi A^6(x_{tar}, y_{tar}, z_{tar}, E', \theta, \phi)\sigma(x_{tar}, y_{tar}, z_{tar}, E', \theta, \phi), \tag{4.23}$$

where $A^6(x_{tar}, y_{tar}, z_{tar}, E', \theta, \phi)$ represents the fraction of particles that are detected at that region of the acceptance. This fraction could, in principle, be measured at each point in the six-dimensional phasespace with a sufficiently large simulation and used to correct the measured yield. However, this is not feasible due to the computing time required. It is convenient, therefore, that it is unnecessary to derive a correction at each point in the six-dimensional phasespace due to the properties of the target-detector system, and the physics of unpolarized inclusive scattering.

First, there was no significant loss of beam intensity along the target, so the measured cross section did not depend on the position from which the scattered particle originated in the target. Therefore, we can integrate over the target position variables to get a new acceptance function which only depends on the measured kinematic variables,

$$Y_{data} = \int dE' d\theta d\phi A^3(E', \theta, \phi)\sigma(E', \theta, \phi). \tag{4.24}$$

Next, we use the fact that in unpolarized inclusive scattering the cross section does

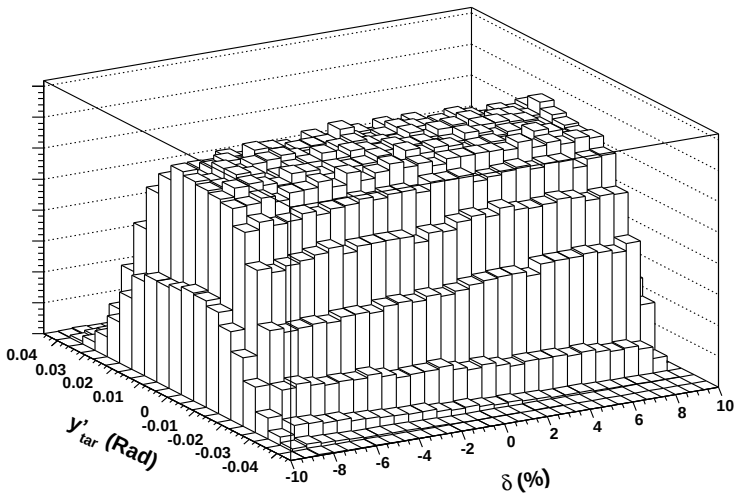

Figure 4-18: Acceptance of the HMS. The z-axis indicates the relative number of particles detected at each point in the phase space. The acceptance function is shown as a function of δ and y'_{tar}, which are analogous to p and (approximately) θ.

not depend on ϕ. Integrating over ϕ gives a new two dimensional acceptance function that depends only on E' and θ:

$$Y_{data} = \int dE' d\theta A^2(E', \theta) \sigma(E', \theta). \tag{4.25}$$

So, although the original acceptance did depend on all six target and kinematic variables, the measured yield depends only on the kinematic variables that the cross section itself depends on. So an effective acceptance function A^2 can be determined in a reasonable amount of time with a high statistics simulation of the detector. An example of the acceptance in the HMS is shown in Fig. 4-18.

Now it is possible to extract the cross section from the measured yield. In principle, $\sigma(E', \theta)$ is inaccessible since it is part of the integrand in Eq. 4.25 and cannot be factored out. However, the acceptance-weighted average cross section is

$$\sigma_{av}(\Delta E', \Delta\Omega) = \frac{Y_{data}(E', \theta)}{\int A^2 dE' d\Omega}, \tag{4.26}$$

and be used to extract $\sigma(E', \theta)$.

Bin Centering

The cross section in Eq. 4.26 must be converted from the average cross section to the value of the differential cross section at a particular combination of E' and θ. We can do this using a model cross section to relate the average cross section to the value at the desired point in the phase space. Denoting the model cross section σ^*, the correction factor we would apply to the measured yield is

$$c_{bc} = \frac{\sigma^*(E',\theta)}{\frac{\int A^2 \sigma^* dE' d\Omega}{\int A^2 dE' d\Omega}}., \tag{4.27}$$

where we have included the acceptance function in the correction factor to give the proper weighting to the average. The cross section at E', θ is then

$$\sigma_{bc}(E',\theta) = \sigma_{ave} \cdot c_{bc}. \tag{4.28}$$

Radiated Cross Section

Now we must take into account the fact that the measured yield, Y_{data}, is actually an integral over the radiated cross section. The incoming electron may lose energy by radiating one or more photons before striking the target nucleus, and the outgoing electron may radiate photons before being analyzed in the spectrometer. If the beam electron radiates, then the scattering at the vertex will occur with an energy lower than the measured beam energy. This will increase the measured yield, relative to the yield at the nominal beam energy, since the cross section is proportional to $1/E^2$. If the outgoing electron radiates on its way to the detector, then it will be measured with a lower energy than it had at the vertex. This means that the measured yield will be less than that expected for the measured energy. At the same time, events will radiate into a given bin from electrons at higher energies that lose energy to radiation. So some events radiate out of the bin,and some events radiate into the bin.

We must account for these radiative effects when calculating the model cross section in order to properly apply the bin centering correction. This means we must

apply another correction factor to relate the radiated cross section at E', θ to the Born cross section at that point. The correction factor is

$$c_{rad} = \frac{\sigma^*_{Born}(E', \theta)}{\sigma^*_{rad}(E', \theta)}, \tag{4.29}$$

Where σ^*_{rad} is the model cross section with radiative corrections applied. The model and the radiative corrections are discussed in detail in Sec. 4.3. So, if we replace σ^* in c_{BC} with the radiated cross section, and include the efficiency factor $\epsilon'_{det}(E', \theta)$, discussed below, in the acceptance integral, the final corrected cross section is

$$\sigma(E', \theta) = \sigma_{ave} c_{bc} c_{rc}, \tag{4.30}$$

which expands to

$$\sigma(E', \theta) = Y_{data} \frac{\sigma^*_{born}}{\int A^2 \epsilon'_{det} \sigma^*_{rad} dE' d\Omega}, \tag{4.31}$$

and we dub the integral in the denominator Y_{sim} in the spirit of Eq. 4.1. Eq. 4.31 is the working equation for computing the Born cross section from our scattering data.

Now all that's left is to properly evaluate Y_{sim}. Here we use the Monte Carlo simulation of the detector. The integral is approximated by binning the data in the simulation with the same binning scheme used for Y_{data}, with σ^*_{rad} and ϵ'_{det} as weighting factors. The acceptance function is automatically generated by binning, provided that we convert the total number of counts in the bin to a fraction representing the number of events detected relative to the number generated that should have reached that bin. So the integral over a particular bin becomes

$$\int A^2 \epsilon'_{det} \sigma^*_{rad} dE' d\Omega = \sum_i \sigma^*_{rad,i} \epsilon'_{det,i} (\Delta E' \Delta\Omega)_{single}, \tag{4.32}$$

where $(\Delta E' \Delta\Omega)_{single}$ represents the relative phase space for a single event in the bin. This quantity is actually the phasespace of the bin divided by the number of events that were generated *in that bin.*. Since events were generated uniformly over the phasespace, we can approximate this by dividing the total phasespace volume over

which events were generated by the total number of events generated,

$$(\Delta E' \Delta\Omega)_{single} = \frac{(\Delta E' \Delta\Omega)_{gen}}{N_{gen}}, \tag{4.33}$$

where N_{gen} must be large enough to make this a good approximation in each bin. In this analysis N_{gen} was 5×10^6, and the total generated phasespace was $0.006 \cdot p_0$ StrGeV. The data were binned into 1% δ bins, and the acceptance cuts give a phasespace volume of $1.05 \times 10^{-4} \cdot p_0$ StrGeV, so the total number of events per final bin was about $87,500$.

4.2.2 Cut Efficiency and Detector Efficiency

The Čerenkov and Calorimeter have both momentum and position dependent efficiencies that must be estimated and corrected for. The Čerenkov detector has two elliptical mirrors whose edges overlap at the center of the acceptance and the mirrors were less efficient in this overlap region. The calorimeter cut placed at $E_{dep}/E^{track} = 0.7$ will also reject some electrons. The cut efficiency exhibited a momentum dependence due to the energy dependence of the calorimeter resolution. The efficiency of the cut must be measured and corrected for in order to get the correct total yield.

It is difficult to measure these effects over all kinematic regions with the production data since it is not possible to form a clean, unbiased electron sample without using both the calorimeter and the Čerenkov. Therefore, these effects were studied using *ep* elastic scattering data as a source of clean electrons. The position dependent Čerenkov efficiency was measured using scans where the elastic peak was positioned at different parts of the acceptance. This allowed for a δ depended efficiency to be computed at each momentum setting. Data were taken at several momenta and so the momentum dependence of both the Čerenkov and calorimeter response could be measured. An example of the detector efficiency function is shown in Fig. 4-19. Note that this correction cancels in the cross section ratio, so we assign no additional systematic uncertainty due to this correction factor.

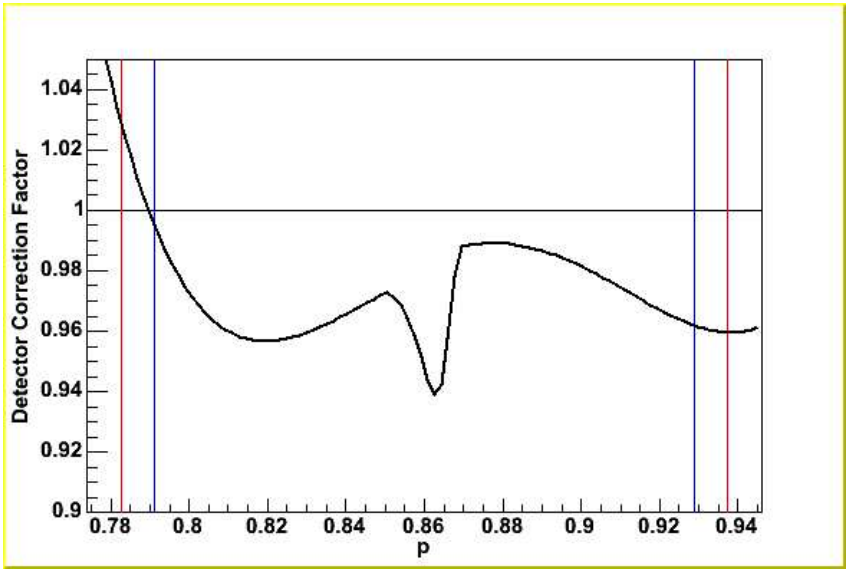

Figure 4-19: Detector and Cut Efficiency in the HMS for $p = 0.86$ GeV. This correction cancels in the cross section ratio.

4.2.3 Energy Loss

Finally, we must account for energy lost by the incoming and scattered electrons as they traverse the target and spectrometer materials. The energy at the vertex is larger (smaller) for the scattered (incoming) electron. Therefore, we must take this into account when computing the cross section. The Hall C Analysis code corrects for energy loss by adding (subtracting) an average value for the energy loss to the particle's total energy, computed from the track momentum, and computes the rest of the quantities from this shifted value. We built the same behavior into the simulation as described in this section.

Charged particles lose energy as they pass through materials. There are several lengths of material that the beam electrons and scattered particles must traverse and to which they can lose energy. This energy loss must be accounted for in order to compute the cross section properly. Since the beam pipe and vacuum chamber share a common vacuum, there is no entrance window to the target. Therefore, the beam electron only loses energy to the target cell walls (if the target is a cryotarget), and the target material traversed before the scattering occurs. The scattered particle, however, traversed several layers of material. First, the particle travels through the

remainder of the target. In the case of the solid targets, the distance depends on the scattering angle. Next there is the target-chamber exit window, an air gap, and the entrance window to the spectrometer.

Instead of correcting the cross section, the analysis code calculates the energy loss in the materials and applies the average energy loss to the particle momentum for each event. The physics quantities calculated by the analysis code, therefore, are computed using the energy-loss corrected vertex values. This same procedure was followed for the monte carlo simulation. The code assumed that the scattering happened at the center of the target. So the energy loss for the beam electron was calculated using 1/2 of the target thickness. After the scattering, the particle traversed the remaining 1/2 of the target material. In the case of solid targets, this length was divided by the cosine of the scattering angle. The scattering chamber exit window was 0.4 mm of Aluminum, followed by an air gap of 15 cm. The entrance window to the HMS is 0.43 mm of mylar. The energy loss is computed using the standard Bethe-Bloch equation [41].

Once the energy loss had been computed, it was applied to the simulated data in the following way. First, the particle momentum and energy were computed from the spectrometer quantities δ, x'_{tar}, and y'_{tar}. Then the energy losses from each stage were summed to find the total energy loss. The total energy loss was then subtracted from the particle's total energy, and the momentum was recomputed. This energy-loss corrected momentum was then binned into the simulated yield histogram for comparison to the data yield histogram.

4.3 Model Cross Section

The simulated yield includes bin-centering and radiative corrections, both of which were computed from a model cross section. The model Born cross section was used as input to the calculations or radiative corrections. The Born cross section model was a sum over two independent model cross sections, one for the DIS piece and one

for the Quasielastic piece:

$$\sigma^*_{Born} = \sigma^*_{DIS} + \sigma^*_{QE}. \tag{4.34}$$

The following sections outline the two different models used to compute the cross section, the radiative correction procedure for computing the radiated cross section from the Born cross section, and finally the iteration procedure for adjusting the model to agree with the data.

4.3.1 Deep Inelastic Cross Section

The DIS cross section is computed differently for different x_{Bj} regions. The difference lies in how the structure function, F_2^A is computed. At $x_{Bj} < 0.8$, the structure function for a nucleus is built using the deuterium structure function. The nuclear structure function is given by

$$F_2^A = F_2^D \left(\frac{Z + N(F_2^n/F_2^p)}{1 + F_2^n/F_2^p} \right). \tag{4.35}$$

where the factor that multiplies F_2^D accounts for the number of protons and neutrons in the nucleus. For isoscalar nuclei, this reduces to

$$F_2^A = (A/2)F_2^D. \tag{4.36}$$

We use a parameterization for F_2^n/F_2^p from Whitlow *et al.*[42] described in Sec.5.1.1. Next, we make an explicit correction for the EMC effect. This correction is fit from our own data by forming the cross section ratio to deuterium, then fitting this ratio, applying the fit polynomial back into the model, re-computing the model cross section tables and re-extracting the cross section in an iterative procedure.

At $x_{Bj} > 0.9$ the nuclear structure function is constructed as a convolution of the sum of the nucleon structure functions with a function that accounts for the smearing due to the Fermi motion of the nucleons. The formalism is well outlined in [43]. The nuclear structure function is computed as the sum over the nucleon

structure functions:

$$F_2^A = Z \cdot F_2^p + N \cdot F_2^n, \tag{4.37}$$

convolved with a function, $f(z, \beta)$, which accounts for the Fermi motion of the nucleon,

$$F_2^A(x, Q^2) = \int_x^A dz f(z, \beta) \left(\mathrm{Z} F_2^p(x/z, Q^2) + (\mathrm{A} - \mathrm{Z}) F_2^n(x/z, Q^2) \right). \tag{4.38}$$

where z is the light-cone fraction of the nuclear momentum carried by the nucleon, x is the momentum fraction of the struck quark, and $\beta = |q_3|/\nu$. The nucleon momentum fraction z ranges from x, (corresponding to a proton at rest) to A, and so the ratio x/z ranges from one to x/A. The data for $f(z)$ are given by [43]. The nucleon structure functions are computed from a universal fit to the DIS background and a resonance fit. The coefficients were fit by Bodek [44] from proton and deuterium data from SLAC E139.

4.3.2 Quasielastic Cross Section

The quasielastic cross section is computed from a y-scaling model, given by a fit to the scaling function $F(y)$. The scaling variable y can be interpreted as the minimum momentum of the struck nucleon in the direction of the virtual photon. This scaling function is defined as the ratio of the measured nuclear cross section to the off-shell cross section for a nucleon, multiplied by a kinematic factor: [45]

$$F(y) = \frac{d\sigma}{d\Omega d\nu} \frac{1}{\mathrm{Z}\sigma_p + \mathrm{N}\sigma_N} \frac{q}{\sqrt{M^2 + (y+q)^2}}, \tag{4.39}$$

where Z is the number of protons in the nucleus, N is the number of neutrons, q is the three-momentum transfer, and M is the proton mass. We use the following parameterization to fit the scaling function $F(y)$

$$F(y) = \frac{C}{y_0} e^{-(y/y_0)^2/2} + \frac{D}{e^{By} + e^{-By}}, \tag{4.40}$$

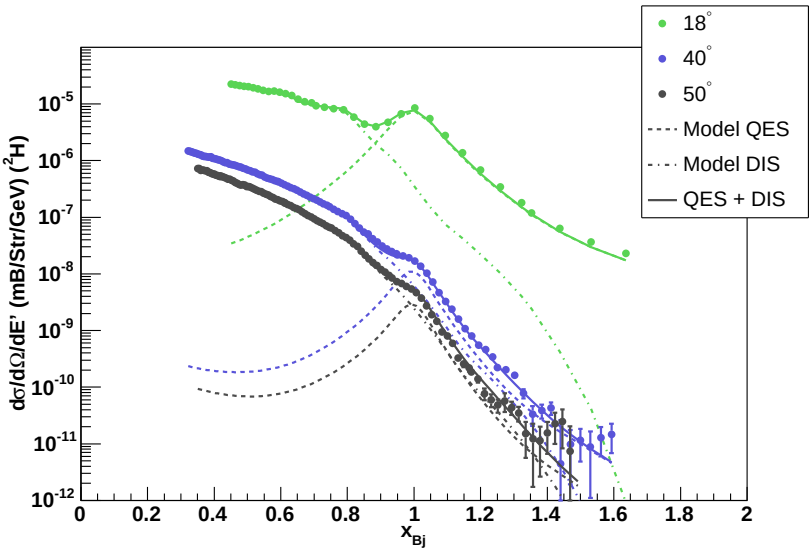

Figure 4-20: Cross Section data and Models for deuterium. The quasielastic and DIS parts of the model are shown, along with the sum. Data are shown for the 18,40, and 50 degrees, which cover the full range of angles and serve to illustrate the agreement of the model with data in regions where the DIS cross section dominates (40 and 50 degrees) and where the quasielastic peak dominates (18 degrees).

where parameters B, C, and D are fit to the data, and y_0 is a parameter given by the Fermi momentum.

The quasielastic peak accounts for a large portion of the total cross section, especially at the lower Q^2 settings. This is important since the model is also used for radiative corrections, and the correction due to the quasielastic tail can be significant far from the peak itself. We therefore fit the peak independently from the DIS part of the cross section. The peak was fit to the data after subtracting off the DIS piece from the model. New parameters for $F(y)$ were calculated, and this process was repeated until good agreement with the data was achieved.

Both pieces of the cross section are iterated until good agreement with the data is achieved. The models and data can be seen in Fig. 4-20. We assign a 2% model uncertainty to the cross section measurement due to bin-centering. This number was computed by measuring the change in the cross section for different input models. A flat cross section, a ξ scaling model and our model were used as inputs. The variation gives the conservative estimate on the uncertainty in the cross section due

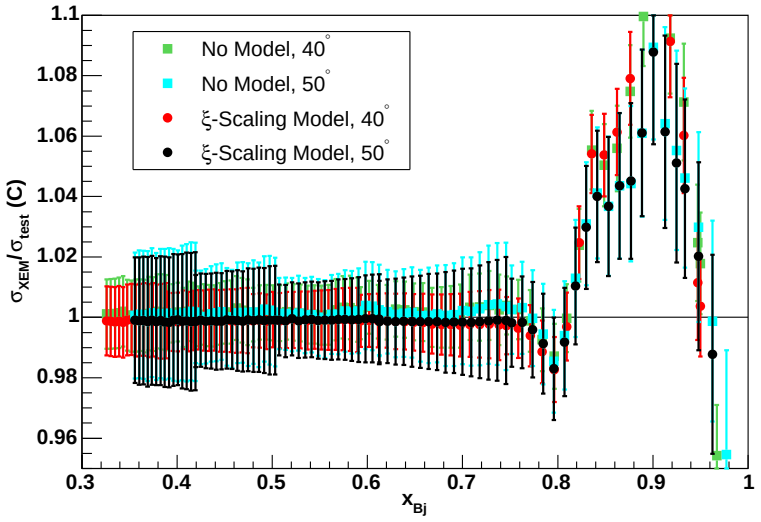

Figure 4-21: Model dependence of the cross section ratio for carbon. This figure shows the ratio of the cross section ratio as calculated using our cross section model, to that calculated a ξ-scaling model, and a flat cross section. The models give the same results for the cross section ratio for $x_{Bj} < 0.8$, and we assign a point-to-point uncertainty of 0.5% to the ratio in this region. At higher x_{Bj}, however, there is a strong dependence on the model and we assign an uncertainty of 2% to the cross section ratio in this region. Note that the cross section ratios presented below are shown out to $x_{Bj} = 0.85$. Data above this region are excluded due to the cut we place at $W^2 = 1.7$ (GeV)^2.

to the model in the bin-centering procedure. The cross section ratios are much less sensitive to the model and bin-centering. Fig. 4-21 shows a comparison of the EMC ratios using the three different cross section models. The spread in the data for the different models gives a conservative estimate of the bin-centering uncertainty. For $x_{Bj} < 0.8$ we assign an uncertainty of 0.5% to the ratio. For larger x_{Bj}, however, the dependence on the model is stronger and we assign an uncertainty of 2% point-to-point uncertainty to both the cross section and the cross section ratios.

4.3.3 Radiative Corrections

The cross section model above is used as input into the calculation for the radiative correction. The radiative correction is applied in order to account for the number of counts that are gained or lost due to radiation of one or more photons by the incoming

or outgoing electron. Radiative corrections are computed to the quasielastic peak and to the inelastic continuum using Eq. (A82) in [46], which is a peaking approximation in the spirit of Mo and Tsai. [47, 48]. No explicit correction is made for the nuclear elastic tail or nucleon resonances. The nuclear elastic tail contributes less than 0.1% to the total cross section in deuterium and even less in heavier targets, and so it is safe to neglect this piece. The resonances make up a small part of the total cross section, and are included in the deep inelastic part of the cross section model, so the radiative tails are included in the total correction for the inelastic cross section.

4.4 Coulomb Corrections

There is an additional correction that must be made due to the acceleration of the electrons in the Coulomb field of the target nucleus. The momentum of the beam electron will increase from its measured value as it approaches the nucleus, and the momentum of the scattered electron will be similarly shifted from the value measured in the detectors stack. This means that if the measured beam and scattered electron energies are E_0 and E', then the energies at the vertex will be $E_0 + \Delta E$ and $E' + \Delta E$. The real cross section depends on the vertex energy values, so we must apply a correction factor to the cross section measured at the asymptotic values of E_0 and E'. There is a rich and varied literature discussing the application of Coulomb corrections in scattering experiments. At the energies in the present experiment, the Effective Momentum Approximation (EMA) is a good approximation [49, 50, 51] to the exact calculation [52]. We apply the correction as outlined in [50], by adding an energy boost to the incoming and outgoing electron energy and calculate the change in the cross section. The energy boost is given by the change in potential energy the electron experiences as it falls into the nucleus from very far away. Setting the potential energy at ∞ to zero, the change in potential energy an electron would experience falling from infinity along the z-axis of a uniformly charged sphere, with a charge Ze and radius

R_0 is (for $z < R_0$):

$$\Delta V(z) = V(\infty) - V(z) = -\frac{\mathrm{Z}\alpha\hbar c}{2R_0}\left(3 - \frac{z^2}{R_0^2}\right), \tag{4.41}$$

where z is measured from the center of the sphere. If we assume that the electron scatters off a nucleon at the center of the nucleus, then $z \to 0$, and the energy boost is given by

$$\Delta E = -\Delta V(0) = -V_0 = \frac{3(\mathrm{Z}-1)\alpha\hbar c}{2R_0} \tag{4.42}$$

Note that we use Z-1 for the charge of the residual nucleus that causes the acceleration, while the references use Z. It has been observed [50] that it is a better approximation to assume the scattering happens closer to the surface of the nucleus. This can be achieved by using a sightly modified effective potential energy given by a factor of $0.75 - 0.8$ times V_0. This factor varies slightly depending on the nucleus in question and represents the difference between using the average value of the focusing factor (see next section) over the transverse extent of the nucleus versus it's value at the center of the nucleus. It is perhaps more enlightening to note that the scaled effective potential is very close to the value of the energy boost given by the average potential inside the nucleus, rather than taking the difference from the edge to the center. That boost is equal to $4V_0/5$. In this analysis, the boost was $\Delta E = 0.775V_0$, where we have just taken the central value of the range of scale factors given by Aste *et al.*[50].

In addition to the energy boost experienced by the electron, there is a second effect that must be accounted for in the cross section. This is the fact that the electron wave function is enhanced, or focused, when it is very near to the nucleus. This feature manifests itself as a scale factor of k_{eff}/k on the wave function, which enters into the cross section quadratically. The focusing factor for the outgoing electron is canceled by the Jacobian when the cross section is expressed in terms of the effective momentum. The correction factor, c_{CC}, is given by the ratio of the model cross section at the nominal kinematics to that at the boosted kinematics:

$$\sigma_{CC} = \sigma_{meas}\frac{\sigma^*(E, E')}{\sigma^*(E + \Delta E, E' + \Delta E)}\left(\frac{E}{E + \Delta E}\right)^2, \tag{4.43}$$

where σ_{meas} is the measured, but uncorrected cross section, and σ^* is the model cross section. The values for the RMS charge radii used in Eq. 4.42 and the resulting boost are given in Tab. 4.4. The values of the radii for helium are measured values, and the rest of the radii are given by the empirical equation from [49]

$$R = 1.1 \cdot A^{1/3} + 0.86 \cdot A^{-1/3}. \tag{4.44}$$

Note, of course, that no correction is made for Hydrogen or deuterium since, in both cases, there is only a single charged nucleon, which is included in the scattering cross section itself. The model used for radiative and bin-centering corrections was also

Target	R_0 (fm)	ΔE (MeV)
^{3}He	1.95	0.85
^{4}He	1.70	1.0
Be	2.70	1.9
C	2.89	2.9
Cu	4.59	10.2
Au	6.55	19.9

Table 4.3: Size of the energy shift due to the acceleration of the electron in the Coulomb field of the nucleus before and after scattering.

used to calculate the Coulomb corrections. The correction was computed at a given kinematic point by computing the cross section at the nominal kinematics and the boosted kinematics, and using Eq. 4.43 to compute the correction. The Coulomb corrections are relatively small for most targets and settings in this analysis. The correction of the order of 0.5% at the lowest momentum for the helium targets, rising to 1 to 2% near the quasielastic peak. For ^{9}Be and ^{12}C the correction is at most 3.0%. For the heavier targets the correction can be significant, reaching 6% for Au at the lowest momentum setting.

4.5 Cross Section Results

The inclusive electron-nucleus scattering cross sections constitute the primary measurement from which the structure function ratios are extracted. We include the cross sections here along with the cross section model that was used for radiative and bin-centering corrections. The model shows good agreement with the data for all targets.

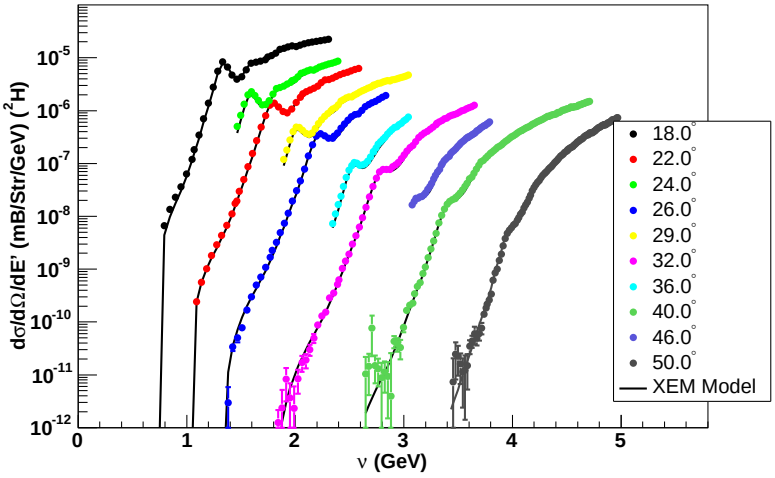

Figure 4-22: ^{2}H Cross Section. The deuterium cross section is used to form the cross section ratios for all targets.

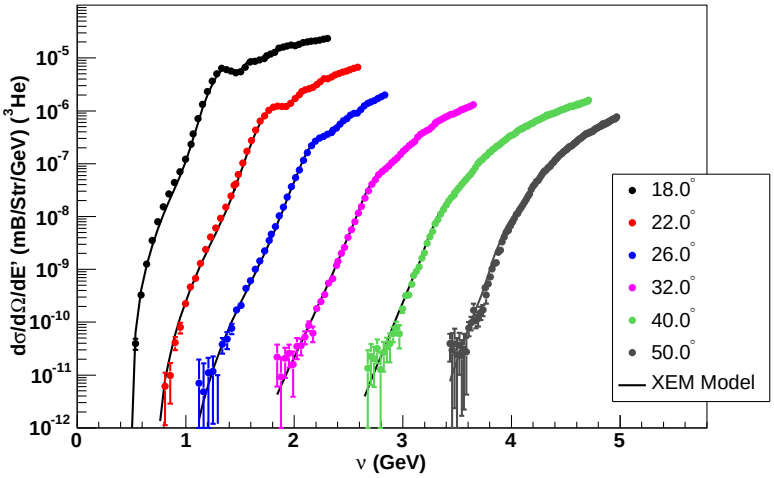

Figure 4-23: ^{3}He Cross Section.

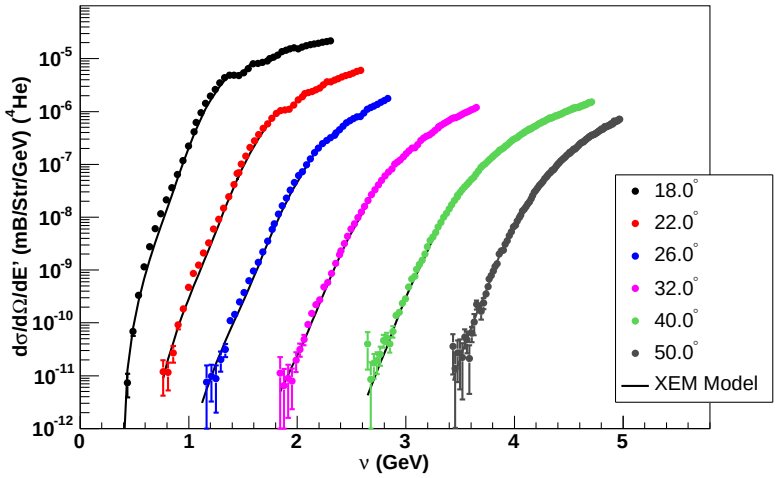

Figure 4-24: ^{4}He Cross Section.

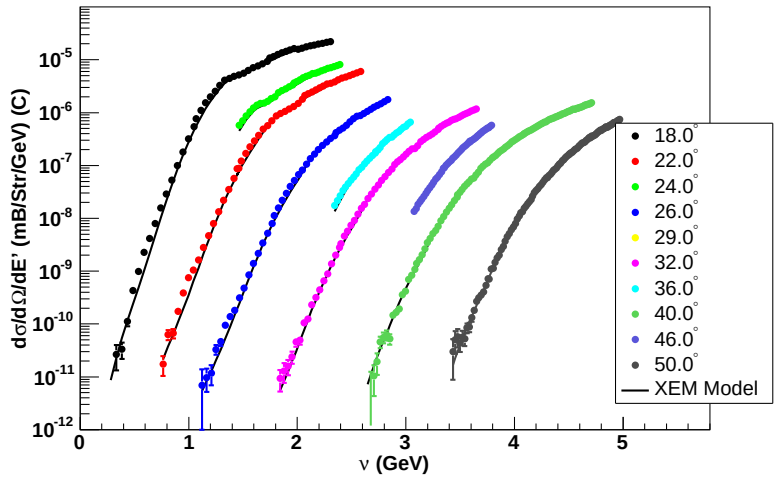

Figure 4-25: C Cross Section.

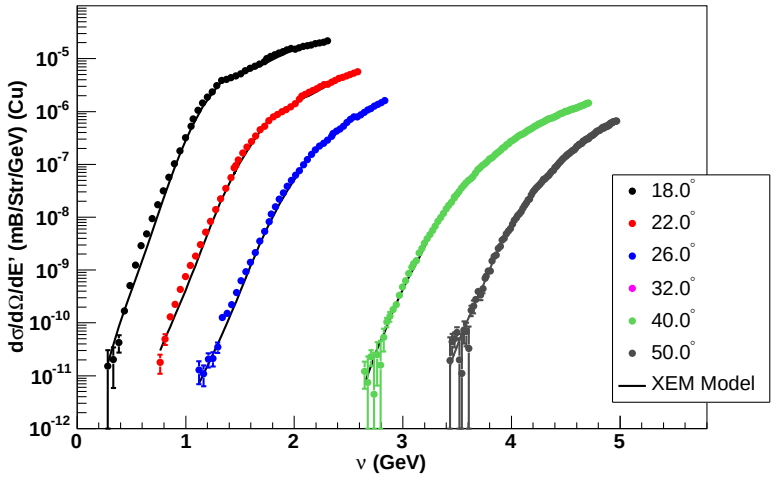

Figure 4-26: ^{63}Cu Cross Section.

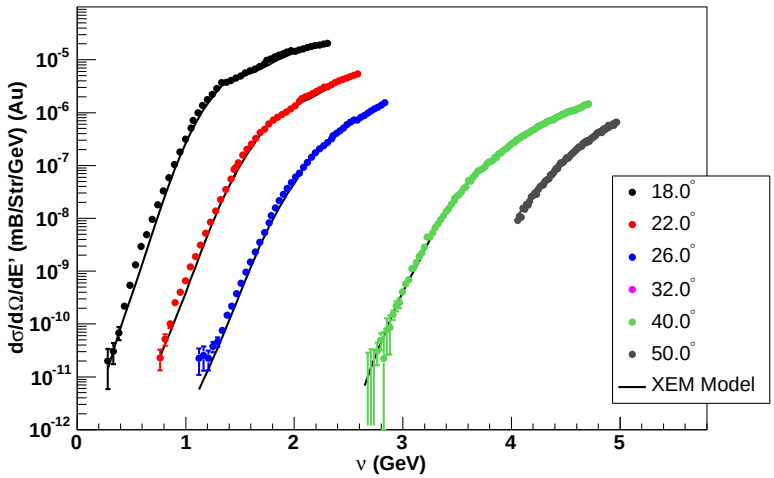

Figure 4-27: ^{63}Au Cross Section.

Chapter 5

Results

We are now prepared to extract the structure function ratios from the measured cross sections. Before discussing the ratios, however, we will first examine the structure functions themselves in order to understand their scaling behavior versus both x_{Bj} and ξ. Following the discussion of the structure functions, we will present the structure function ratios, along with the details of the proton excess correction and the ratio of the longitudinal to transverse cross sections. The systematic uncertainties have been discussed throughout the text, and will be presented in summary at the end of the chapter.

5.1 Structure Functions

The EMC effect demonstrates that the structure function per nucleon, $F_2^{\mathrm{A}}/\mathrm{A}$, exhibits a nuclear dependence. The structure functions of deep inelastic scattering give information about how momentum is distributed among the quarks in the nucleus. At high momentum and energy transfer, the nucleon structure functions scale in x_{Bj}. At lower-energy kinematics, Björken scaling is violated due to finite-mass effects, and because other processes (nucleon resonances, quasielastic scattering) become more prominent. However, the scaling of the structure functions in ξ holds to lower Q^2 because it partially accounts for the mass-effects that cause the scaling violations in x_{Bj} at low Q^2. It is, therefore, interesting to study the structure functions in order

to study the scaling behavior in x_{Bj} and ξ before examining the cross sections ratios. The next section describes the process for extracting the structure function from the cross section and presents the results for several targets.

5.1.1 Extraction of $F_2^{\rm A}$ from Cross Sections

The structure functions are extracted using the measured cross sections and a model for the ratio of longitudinal to transverse cross sections, $R = \sigma_L/\sigma_T$. We start with the form of the cross section as given in Eq. 2.1,

$$\sigma_{\rm A} = \frac{4\alpha^2 E'^2}{Q^4}\left[2\frac{F_1^{\rm A}}{M}\sin^2\frac{\theta}{2} + \frac{F_2^{\rm A}}{\nu}\cos^2\frac{\theta}{2}\right]. \tag{5.1}$$

This can be further reduced to the following form using Eq. 2.4,

$$\sigma_{\rm A} = \sigma_{Mott}\frac{F_2^{\rm A}}{\nu}\left[1 + \tan^2\frac{\theta}{2}\left(1 + \frac{\nu^2}{Q^2}R - 1\right)\right], \tag{5.2}$$

where σ_{Mott} is the familiar Mott cross section, $\sigma_{Mott} = 4\alpha E'^2\cos^2(\theta/2)/Q^4$. Solving Eq. 5.2 for $F_2^{\rm A}$ gives

$$F_2^{\rm A} = \nu\frac{\sigma_{\rm A}}{\sigma_{Mott}}\frac{1}{(1+\beta)}, \tag{5.3}$$

where β is

$$\beta = 2\tan^2\frac{\theta}{2}\left(\frac{1+\frac{\nu^2}{Q^2}}{R-1}\right). \tag{5.4}$$

We then compute the structure function at x_{Bj} and Q^2 using the measured cross section, $\sigma_{\rm A}$, and a model for R at that point. If R is independent of A, then β is also independent of A, and the structure function ratio will be equal to the cross section ratio.

The model for R used in this analysis is the so-called R_{1990} from [42] which is a fit to world data. This is the same model for R that was used to compute the cross section for bin-centering and radiative corrections. The parameterization is the average of three different fits. Each of the fits has a slightly different functional form, and each describes the data well. The final parameterization, R_{1990}, is given by the

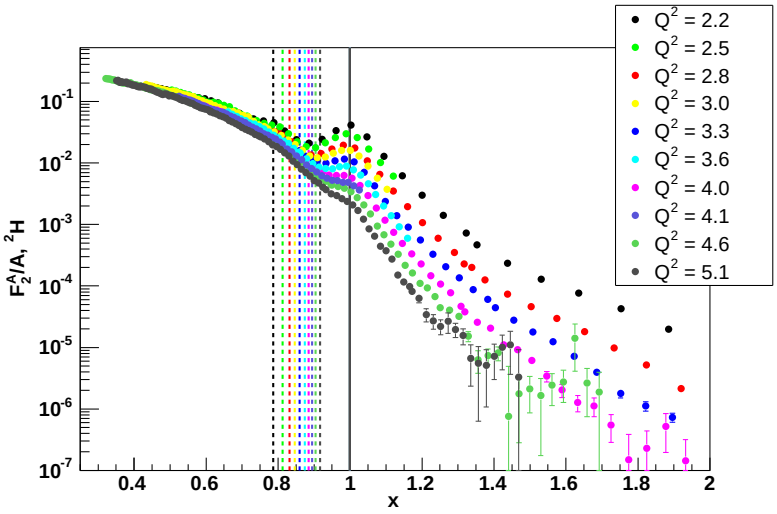

Figure 5-1: Structure function per nucleon for deuterium vs. x_{Bj}. The solid line at $x_{Bj} = 1$ indicates the quasielastic peak, while the dashed lines indicate the positions of the Δ for the different Q^2 settings. The Q^2 values listed in the legend are the Q^2 values at $x_{Bj} = 0.6$. The most notable feature at these kinematics is that Björken scaling breaks down, as expected, well before the quasielastic peak. Björken scaling is not expected to hold in the resonance region. Note that the units have been suppressed in the figure for clarity. The units of Q^2 are $(\mathrm{GeV/c})^2$.

average of the three fits,

$$R_{1990} = (R_A + R_B + R_C)/3, \tag{5.5}$$

$$R_A = a_1 R_{log} + \frac{a_2}{(Q^8 + a_3^4)^{1/4}}, \tag{5.6}$$

$$R_B = b_1 R_{log} + \frac{b_2}{Q^2} + \frac{b_3}{Q^4 + 0.3^2}, \tag{5.7}$$

$$R_C = c_1 R_{log} + \frac{c_2}{\sqrt{(Q^2 - Q_r^2)^2 + c_3^2}}, \tag{5.8}$$

$$R_{log} = \frac{1 + 12\left(\frac{Q^2}{1+Q^2}\right)\left(\frac{0.125^2}{0.125^2 + x_{Bj}^2}\right)}{\ln\left(\frac{Q^2}{0.4}\right)}, \tag{5.9}$$

$$Q_r = 5 \cdot (1 - x_{Bj}). \tag{5.10}$$

5.1.2 Structure Functions

The structure functions were extracted from the cross sections using Eq. 5.3 and plotted versus x_{Bj} and ξ. Fig. 5-1 shows the structure function for deuterium as a

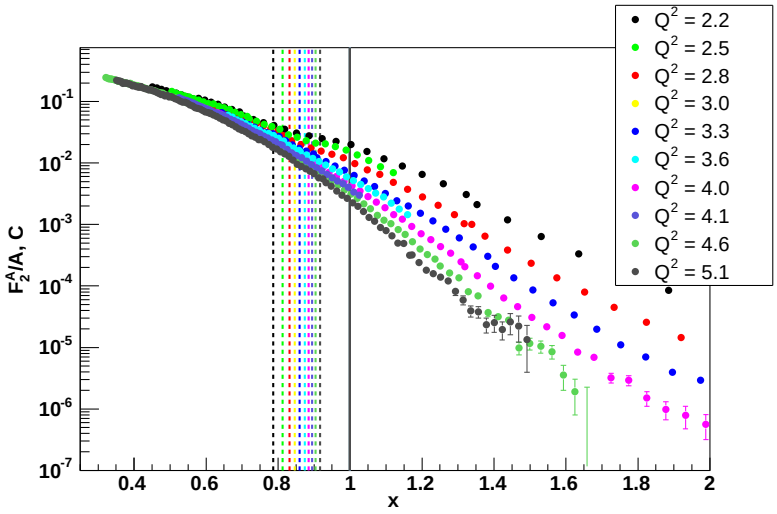

Figure 5-2: Structure function per nucleon for carbon vs. x_{Bj}. The solid line at $x_{Bj} = 1$ indicates the quasielastic peak, and the dashed lines indicate the positions of the Δ for the different Q^2 settings. The Q^2 values listed in the legend are the Q^2 values at $x_{Bj} = 0.6$. The scaling violations in carbon differ from those in deuterium. The Fermi-motion of the nucleons washes out the resonances and the quasielastic peak.

function of x_{Bj}. The data are plotted over the entire kinematic region covered in the experiment, although this analysis will focus exclusively on the region below $x_{Bj} = 1$. The solid line at $x_{Bj} = 1$ indicates the position of quasielastic peak, while the dashed lines indicate the positions of the Δ for each Q^2 setting. The Q^2 values listed in the legend are the Q^2 values corresponding to $x_{Bj} = 0.6$. The units have been suppressed in the figure for clarity. Although Björken scaling holds at high Q^2 and high W^2, it is not expected to hold well over much of the kinematic region in this experiment. This is demonstrated in our data by the clear Q^2 dependence of the structure function in Fig. 5-1. The quasielastic peak is very prominent at the E03-103 kinematics, and the Δ peak is also clearly visible at several of the Q^2 settings. Qualitatively, all Q^2 settings scale fairly well for $x_{Bj} < 0.6$, and the scaling improves as Q^2 increases. At the four settings $Q^2 \geq 4.0$ (GeV/c)^2, both the Δ and the quasielastic peak are greatly suppressed and those data lie much closer together out to much higher x_{Bj} values. This is also expected, since as Q^2 increases, the DIS cross section dominates the quasielastic cross section, and also because the nucleon resonances are shifted to

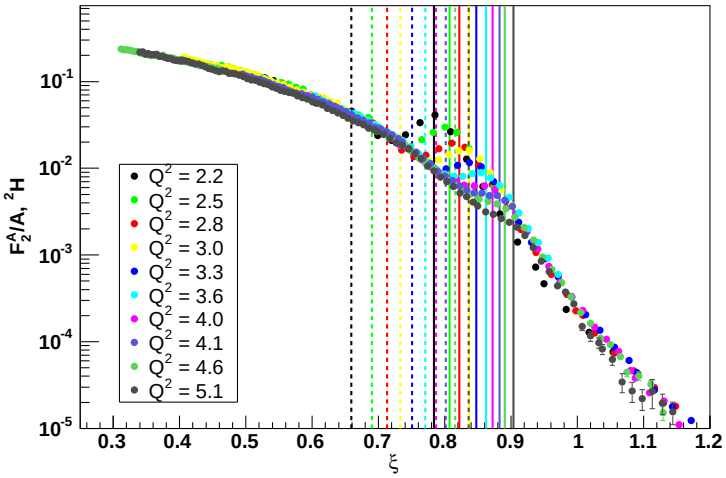

Figure 5-3: Structure function per nucleon, $F_2^{\mathrm{D}}/\mathrm{A}$, for deuterium. The solid lines indicate the position of the quasielastic peak and the dashed lines represent the positions of the Δ peak. The structure function clearly scales better as a function of ξ than in x_{Bj}, and even scales beyond the quasielastic peak.

higher and higher x_{Bj} values.

The carbon structure function for carbon as a function of x_{Bj} is shown in Fig. 5-2 and shows a slightly different picture. Björken scaling is still violated in the resonance region and near the quasielastic peak, but the peaks themselves are washed out due to the Fermi motion of the nucleons in the nucleus. In fact, at this scale, the Δ is no longer visible and the quasielastic peak is only visible as a shoulder for the lower Q^2 settings. The curves at the higher Q^2 settings agree very well, even at the quasielastic peak. This is a qualitative illustration of how true scaling of the structure functions can be imitated in the resonance region by nuclear effects as discussed earlier in Sec. 1.3.

The picture is quite different when we examine the structure functions versus ξ. The deuterium and carbon structure functions as a function of ξ are shown in Figs. 5-3 and 5-4. The first thing to note is that the position of the quasielastic peak depends on Q^2 like the other resonances. The peak moves to lower ξ for lower Q^2. Below the quasielastic peak the structure function exhibits very little Q^2 dependence and so exhibits ξ-scaling. These plots serve to illustrate, qualitatively, that ξ-scaling

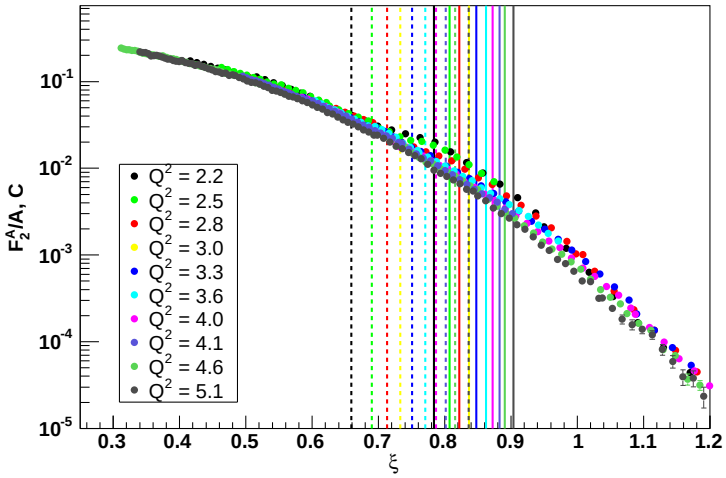

Figure 5-4: Structure function per nucleon, $F_2^{\mathrm{C}}/\mathrm{A}$, for carbon. The solid lines indicate the position of the quasielastic peak and the dashed lines represent the positions of the Δ peak. The structure function clearly scales better as a function of ξ than in x_{Bj}, and even scales beyond the quasielastic peak.

holds better than x_{Bj}-scaling in the resonance region and near the quasielastic peak. Furthermore, the structure function as measured at different Q^2 values agree *above* the quasielastic peak. That is, the structure function exhibits ξ-scaling for $x_{Bj} > 1$. The quasielastic peak is seen as a deviation from the universal background curve for all Q^2 settings. The three highest Q^2 settings agree very well out to about $\xi = 0.8$, which lies just below the quasielastic peak for the lowest Q^2 setting. The structure functions are shown as functions of x_{Bj} and ξ for the rest of the targets in Sec. A.1.

The dramatic difference between the x_{Bj} and ξ plots is essentially a result of mapping. Projecting onto ξ shifts and compresses the lower Q^2 points to lower ξ values. This is more than a mathematical trick. At finite Q^2, ξ is a better approximation to the x used in the infinite momentum frame where Björken-Scaling holds strictly. In this frame, the quark is free and has no transverse momentum, and so the quark momentum is easily related to the nucleon momentum via x. As we move from the infinite momentum frame to finite Q^2, mass effects become important as Q^2 is reduced, and x_{Bj} becomes less suitable as the energy is reduced. One could apply explicit target-mass corrections to the points at each x_{Bj} value, but using ξ

is a better approximation [53, 54]. This is because ξ partially accounts for these mass effects and therefore exhibits a different approach to the scaling at infinite Q^2. For the kinematics of E03-103, ξ-scaling is better satisfied for the structure functions than Björken scaling, but results for the cross section ratios will be presented in both variables. We now turn to a more quantitative discussion of x_{Bj} and ξ scaling.

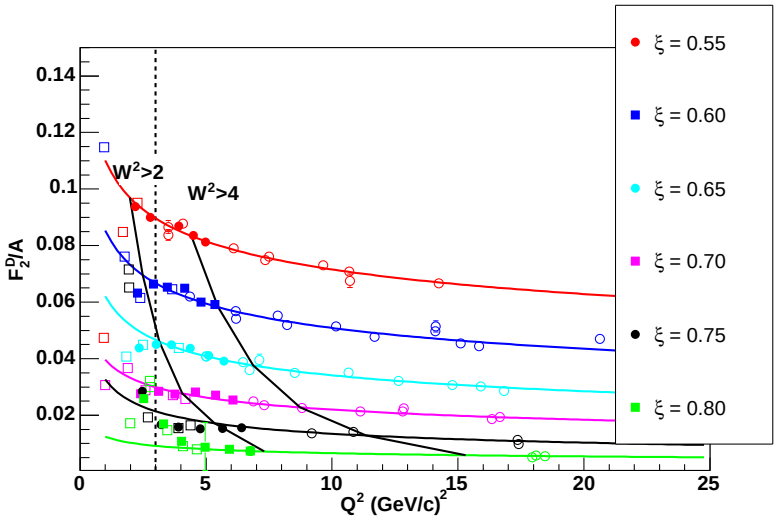

Figure 5-5: ξ-Scaling in deuterium. The structure function for deuterium is plotted as a function of Q^2 for several values of ξ. Open circles (squares) are SLAC (JLab) data, and filled squares are E03-103 data. The structure function continues to scales to a few percent as low as $Q^2 = 3$ (GeV/c)^2 except at the highest ξ values.

5.1.3 Q^2 Dependence of F_2^{A}

The scaling of the structure function F_2^{A} holds strictly in the Björken Limit, and holds approximately at finite Q^2. The scaling of the structure function with ξ holds to lower Q^2 than does the scaling in x_{Bj}. In this section we examine, quantitatively, the Q^2-dependence of the structure functions for both variables. Fig. 5-5 shows the structure function for deuterium as a function of Q^2 for several values of constant ξ. The data from E03-103 are plotted along with data from E89-008 [34] at low W^2, and SLAC [55] at high Q^2. The values at constant ξ for E03-103 were computed by fitting the structure function data near the desired value of ξ. The shape of the structure function is different for different ξ regions. At low ξ, the structure function

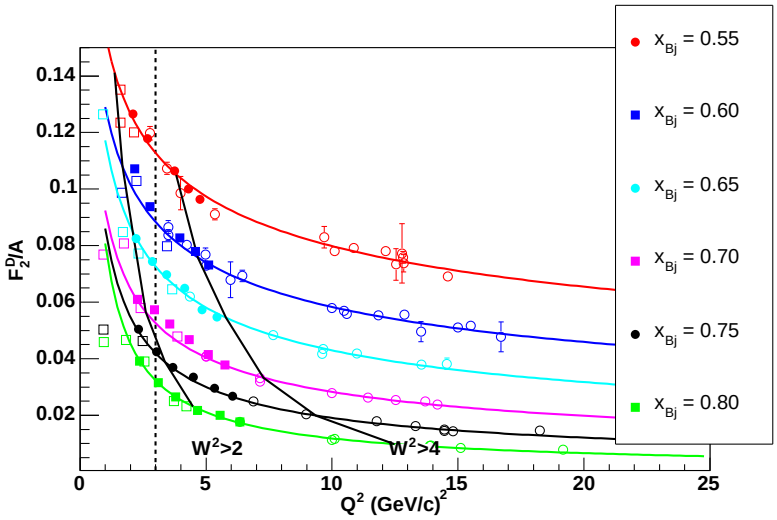

Figure 5-6: Björken Scaling in deuterium. The structure function for deuterium is plotted as a function of Q^2 for several values of x_{Bj}. Open circles (squares) are SLAC (JLab) data, and filled squares are E03-103 data. The scaling violations appear at higher Q^2 than they do when plotted versus ξ.

changes relatively slowly and is best fit to a straight line. At large ξ, however, it drops more rapidly, and an exponential is the more appropriate fitting function. In order to choose the appropriate function for a given point, the structure function was fit twice at each Q^2 point. The model which gave the χ^2/NDF closest to one was chosen as the fit for that Q^2 point. The error shown is the error from the fit parameters only.

In Fig. 5-5 we see that the structure function for deuterium exhibits logarithmic scaling violations expected from QCD, but does not show strong violations in the resonance region. Scaling violations are expected due to the resolving power of the virtual photon, as described in [56]. As Q^2 increases, so does the resolving power of the virtual photon, and the scattering is more like scattering from an individual quark. At low Q^2, however, the virtual photon scatters from groups of quarks and gluons. Since a group of quarks and gluons will carry a larger momentum fraction than any of the individual quarks in the group, the scattering at lower Q^2 will show a higher fraction of quarks with larger x_{Bj}. Said another way, the structure function at a constant value of x_{Bj} or ξ will increase as Q^2 decreases. The curves in the figure

are fits to the high Q^2 data from SLAC to a function of the form

$$F_2^{\mathrm{A}} = \exp(a + b \cdot \ln(Q^2)), \tag{5.11}$$

such that $d\ln(F_2)/d\ln(Q^2) = constant$ as predicted by QCD. Deviations of the data from the curves give a measure of scaling violations as a function of Q^2. Note that no W^2 cut has been applied to the data at this stage. Scaling violations are at the few percent level all the way down to Q^2 values of $Q^2 = 2(\mathrm{GeV/c})^2$ for $\xi < 0.75$, and down to $Q^2 \approx 3$ $(\mathrm{GeV/c})^2$ for $\xi = 0.75$. The structure function is shown as a function of Q^2 for constant x_{Bj} values in Fig. 5-6.

5.2 Cross Section Ratios

The structure functions exhibit ξ-scaling to Q^2 as low as 2 $(\mathrm{GeV/c})^2$ as shown in the plots above. We will therefore use data above this cutoff to examine the ratios of cross sections as functions of ξ. Cuts were placed on the invariant mass, at $W^2 = 1.7$ $(\mathrm{GeV})^2$ and $Q^2 = 2.5$ $(\mathrm{GeV/c})^2$. The invariant mass cut excludes most of the Δ and quasielastic peaks, but accepts the rest of the resonance region. The Q^2 cut was chosen based on Q^2-dependence results from Sec. 5.1.3. We note that scaling breaks down more quickly at higher values of ξ. For example, at ξ of 0.8, the structure function rises very quickly as Q^2 decreases below Q^2 of 4 $(\mathrm{GeV/c})^2$. In our kinematics, Q^2 increases as ξ increases and that the cutoff of $W^2 = 1.7$ $(\mathrm{GeV})^2$ corresponds to Q^2 values greater than 5.8 $(\mathrm{GeV/c})^2$ for the lowest Q^2 setting, safely within the ξ scaling region, as indicated in Figs. 5-5 and 5-6. We first discuss the results for carbon and ^{4}He, focusing on the agreement of these results with world data, and then turn to the new result for ^{3}He. The ratios were constructed by binning the data in 1% δ bins for each momentum setting and computing the ratios for the final cross sections. These data were then re-binned into bins of constant ξ or x_{Bj}. We present results for the ratios with the separate Q^2 settings as an example of the Q^2 dependence of the ratio. We then present results for the two highest Q^2 settings averaged together. The data

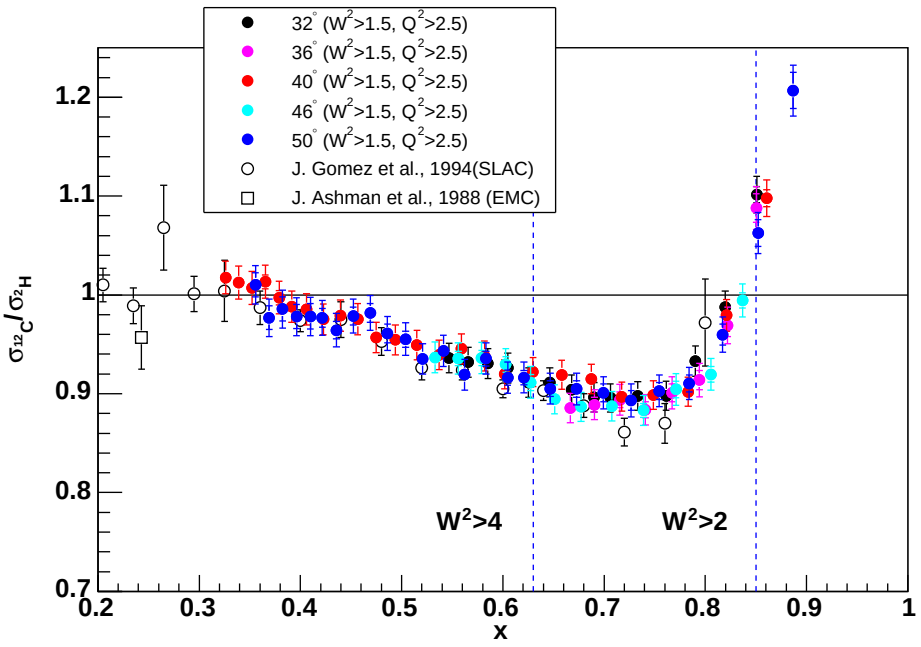

Figure 5-7: Ratio of ^{12}C and ^{2}H cross sections for several Q^2 settings as a function of x_{Bj}. The dashed vertical lines indicate the value of W^2 for the highest Q^2 setting (50°). The data at 36° and 46° were collected with a beam of 5 (GeV/c)^2.

used to generate the plots presented in this chapter may be found in Sec. A.1.

5.2.1 Cross Section Ratio for Carbon

The EMC effect has been well studied in carbon. SLAC measured the ratio of carbon to deuterium in their comprehensive study in 1994 [15] and the EMC collaboration measured the ratio in the followup to their original measurement on Iron [14]. We therefore present our result on carbon first. The discussion of the carbon results includes details of how the E03-103 results were derived, as well as how the results from other experiments are displayed as a function of ξ. Our results are displayed in Figs. 5-7 and 5-10 with data from SLAC[15], EMC[14] and JLab E89-008[7]. The ξ values in the E89-008 were converted to x_{Bj} using the beam energy of 4.045 GeV and the scattering angle of 55°. The E03-103 results are the average over the two highest Q^2 settings (40° and 50° data) in x_{Bj} and ξ bins of constant width. The statistical error is significantly smaller than the point-to-point systematic error of 0.8% and so

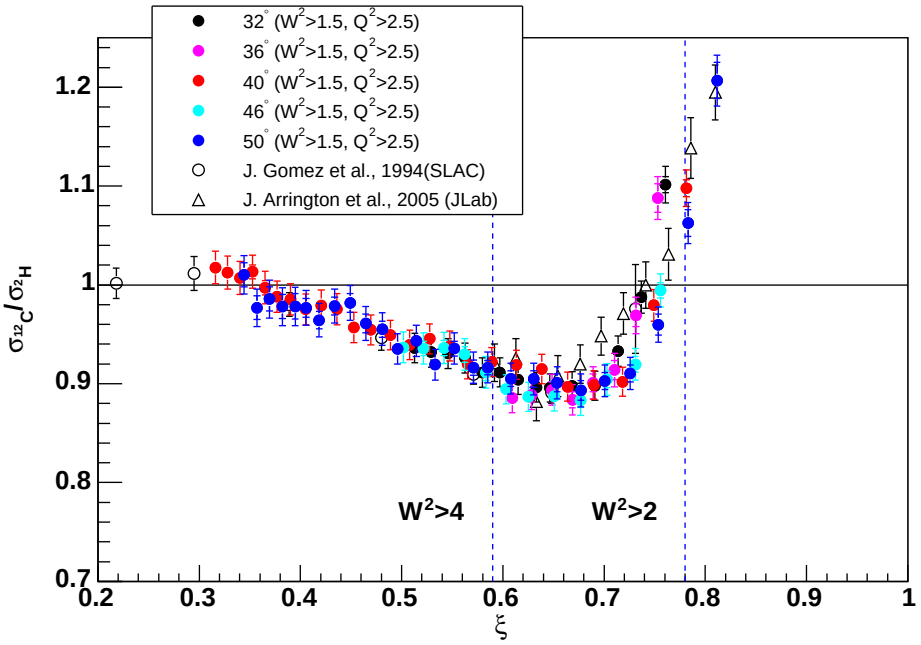

Figure 5-8: Ratio of ^{12}C and ^{2}H cross sections for several Q^2 settings as a function of ξ. The dashed vertical lines indicate the value of W^2 for the highest Q^2 setting (50°). The data at 36° and 46° were collected with a beam of 5 (GeV/c)^2.

we are able to present a very fine grid over the kinematic range covered. There is also a normalization uncertainty of 1.1% due primarily to the target thickness and integrated charge measurements. Systematic errors will be discussed in more detail in Sec. 5.3.

We turn first to the cross section ratio for the various Q^2 settings as a function of x_{Bj} and ξ shown in Figs. 5-7 and 5-8. Data were taken on carbon and deuterium at 2 different beam energies and so there are more settings. The different settings agree very well over most of the kinematic range covered. However, for the region above $x_{Bj} = 0.75$, the two lowest Q^2 settings (32° and 36°) begin to show deviations from the higher Q^2 when the structure function is plotted versus ξ, as in Fig. 5-8. while these low Q^2 settings settings deviate in the region $\xi > 0.7$, the highest Q^2 settings agree over the entire region covered by E03-103. We therefore use only those settings for the final binning.

The final, re-binned data are shown in Figs. 5-9 and 5-10. Our data agree well with both the SLAC and previous JLab data out to $x_{Bj} = 0.7$. At the higher x_{Bj} region the

data diverge slightly from one another, but are consistent with one another. E03-103 has significantly smaller error bars than the other two data sets in this region, though the data were taken at relatively low values of W^2 as indicated by the blue dashed lines. Note, however, that at the third crossover point (where the ratio becomes greater than one around x_{Bj} of 0.83) the older JLab data are at lower W^2 ($W^2 \approx 1.5$ $(\mathrm{GeV})^2$). Also the E03-103 data have Q^2 values around 5 $(\mathrm{GeV/c})^2$ and the highest energy SLAC point has a Q^2 value of 10 $(\mathrm{GeV/c})^2$. It is significant that these three data sets agree as well as they do, given the different kinematics regions covered. It is also significant that the third crossover point is consistent for the two JLab data sets and the SLAC fits. The position of the minima for the datasets are also consistent within error bars. However, it is notable that the depths of the minima are slightly different for each set. The SLAC data drop as low as 0.85, while the E03-103 data only drop to 0.9. All three sets have a consistent value at the first crossover point.

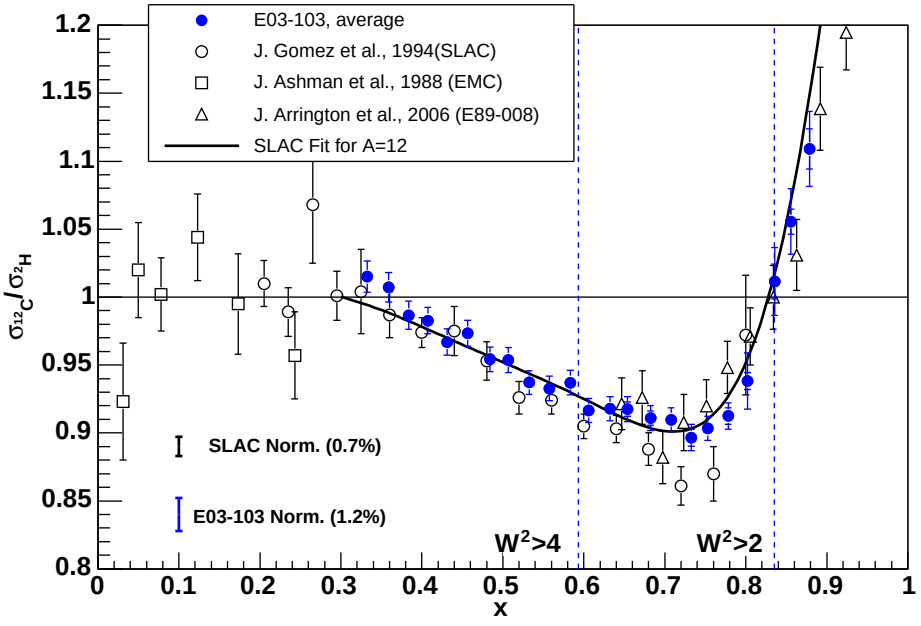

Figure 5-9: Ratio of ^{12}C and ^{2}H cross sections. The E03-103 result (solid circles) are shown with data from SLAC[15] as open circles; EMC[14] as open squares; and JLab E89-008[7] as open triangles. The SLAC fits are the ln (A) parameterizations from[15]. The vertical dashed lines delineate different W^2regions for the E03-103 data.

Fig.5-10 shows the same data presented as a function of ξ. The SLAC data shown here are the coarse-binned data from[15], and have been corrected for Coulomb distortion [57]. The Coulomb corrections were less than 1%. Again, the agreement between the data is good. In particular, all three data sets show the same second and third cross over points. Our data have much higher precision at $\xi > 0.7$ and also show some deviation from the world data in this region. Note that the data now show the same depth of minima, though this may be a result of the re-binning since there is no longer a data point where the minimum lies for the finely binned data. Also, there may be a slight difference in the ξ positions of the minima for the different experiments. There is a noticeable discrepancy between the JLab datasets between $\xi = 0.68$ and $\xi = 0.72$, before the third crossover. The disagreement among the JLab measurements may be significant, especially given that they are at more similar kinematics than the SLAC data. The disagreement with the high ξ SLAC point is less significant given the large error bar on the point. However, the two JLab data sets agree well at the crossover and beyond. There is also disagreement with the SLAC fit. However, this is due to the conversion of the SLAC parameterization that was attempted with the SLAC data. The fit is generated as a parameterization of x_{Bj} and A. In order to produce the fit in the plot, a fit was done to x_{Bj} versus ξ for the SLAC kinematics. Then for a given ξ point, an x_{Bj} value was generated, corresponding to the x_{Bj} value in the SLAC experiments. This x_{Bj} was used to compute the value of the fit, and that value was plotted at ξ.

In general, the agreement for carbon is very good. The various datasets are consistent within experimental uncertainties in both x_{Bj} and ξ. The various data sets give consistent crossover points, and the position and the depth of the minimum are also consistent with experimental uncertainties. The agreement among the data sets gives confidence in our method of extracting the ratios, and also indicates that the cross section ratio exhibits very little Q^2 dependence over a large kinematic range. Therefore, we are confident as we move on to study the lighter nuclei which comprise the most significant measurement in E03-103.

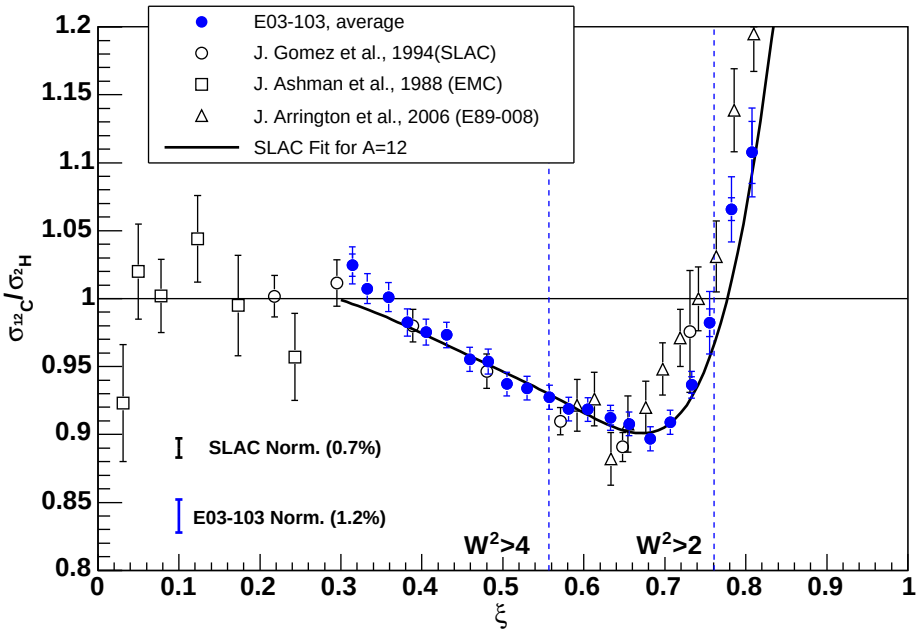

Figure 5-10: Ratio of ^{12}C and ^{2}H cross sections. The SLAC fit was converted from $x_{Bj}$to ξ by fitting the kinematic settings to get x_{SLAC} as a function of ξ_{SLAC}.

5.2.2 Cross Section Ratios for ^{4}He

There is very little data on the EMC effect in light nuclei. The SLAC measurement on ^{4}He and the HERMES measurement on ^{3}He are the only dedicated measurements of the effect for A$\leq$4. This is unfortunate since calculations are more tractable for few body nuclei, and therefore they serve as a good proving ground for the various models of in-medium modification of nucleon structure. Our measurement of the effect in ^{3}He and ^{4}He will therefore provide a strong improvement to the world data in this region.

We discuss the ^{4}He result, shown in Figs. 5-11 and 5-12, first since it can be more easily compared with world data, and has no complications due to proton or neutron excess. The data are presented along with the SLAC parameterization for A=4 and A=12. The fit parameterizes the cross section ratio as a function of ln (A). Calculations from Benhar *et al.* [30] and Smirnov [31] are also presented. There is reasonable agreement, to within the normalization uncertainties, with the existing measurement from SLAC and the present measurement is a great improvement at x_{Bj}

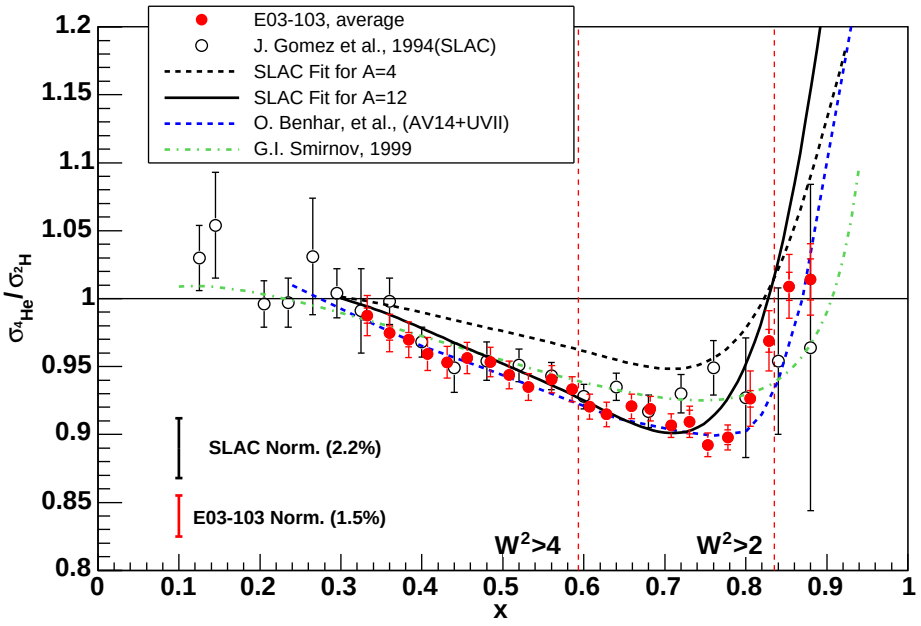

Figure 5-11: ^{4}He EMC Ratio as a function of x_{Bj}.

> 0.7. It is instructive to compare the data with the parameterizations from the SLAC measurement. Clearly the fit for A=12 compares better with both measurements than does the fit for A=4. The fact that the strength of the effect is the same in ^{4}He as in carbon is an indication that the effect may be more dependent on the nucleon number density, ρ(A) than on ln (A). The fits shown in the figure are the fits versus ln (A), and so are different for A=4 and A=12. But ^{4}He and carbon have about the same average nucleon number density and therefore should agree if the effect depends on ρ. This dependence is discussed in the original SLAC paper and will be discussed below. One significant difference between the carbon and ^{4}He results is that the third crossover may occur at larger x_{Bj} for ^{4}He. The data are presented as a function of ξ as shown in Fig. 5-11. The Benhar curve was converted to ξ using a Q^2 value of 10 (GeV/c)^2.

Plotted versus ξ, the data remain consistent with the (now coarse-binned) SLAC data, which have been converted to ξ using x_{Bj} and Q^2 from the experimental kinematics. The calculations both describe the data fairly well in the region from $x_{Bj} < 0.7$, and both are consistent with the SLAC data. Our data give a preference

to the Benhar calculation[30], which better describes the depth and position of the minimum. This calculation takes into account the binding energy of the nucleons in a realistic way. An off-shell prescription is used to write down the nuclear tensor without modifying the parton distributions inside the nucleons. The calculation is done for both infinite nuclear matter and deuterium at the same kinematics as the SLAC data (Q^2=10 (GeV/c)^2). This calculation does an excellent job for nuclear matter, and indeed, they find that binding, properly applied, is sufficient to explain the effect at large x_{Bj}. Their calculation describes our data quite well for $x_{Bj} < 0.7$, but disagrees markedly with our data above that point, particularly in the position of the third cross over point. This may be an indication that binding and Fermi motion may not be enough to explain the effect for finite, or at least very light, nuclei. Smirnov's calculation is a global fit to all EMC effect data spanning a large range in A and Q^2. The SLAC data for ^{4}He were included in the fit, but do not constrain the fit well at the highest x_{Bj} values. The disagreement with Smirnov is consistent with the statement that the per-nucleon structure function of ^{4}He does not follow the pattern observed in heavier nuclei.

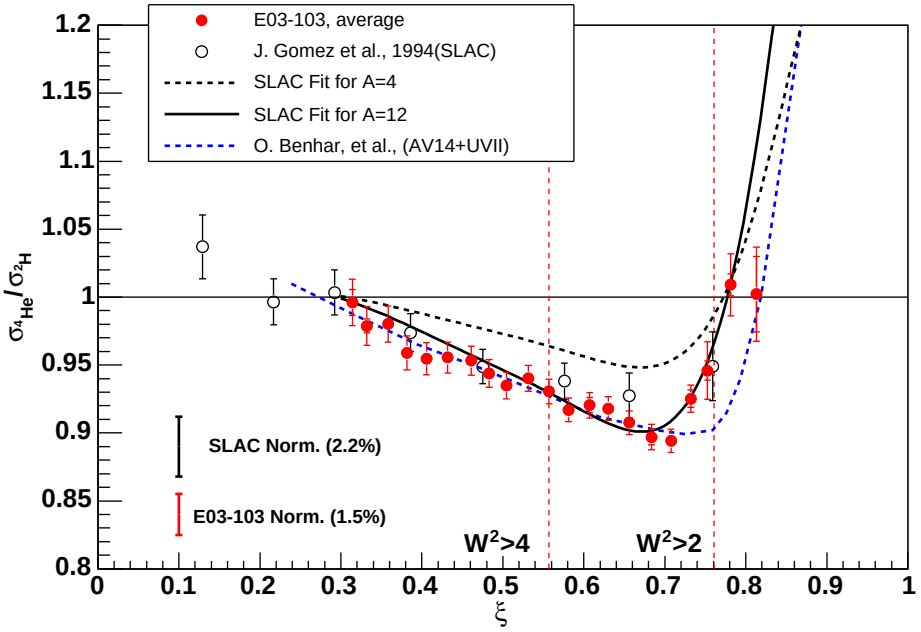

Figure 5-12: ^{4}He EMC Ratio as a function of ξ.

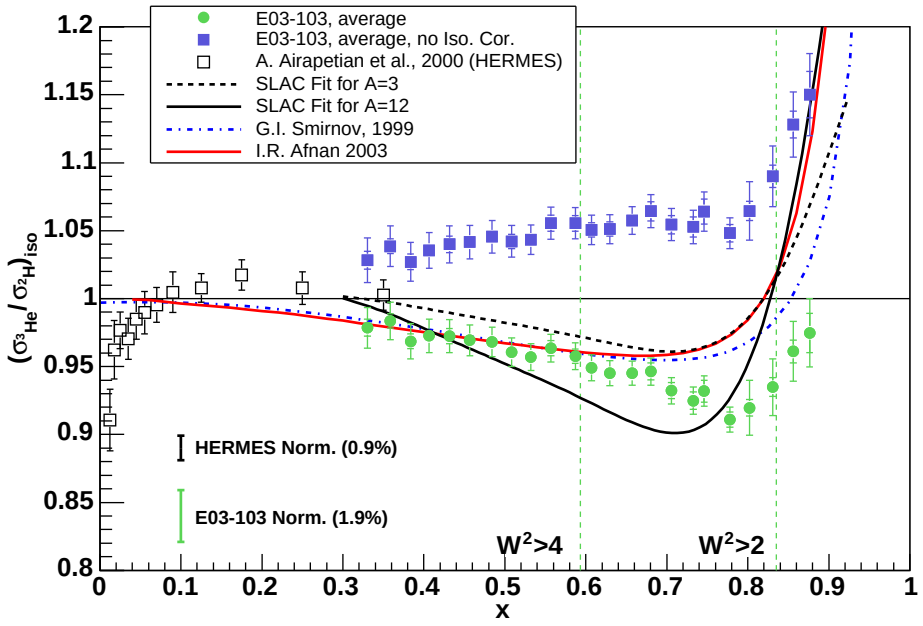

Figure 5-13: ^{3}He EMC Ratio as a function of x_{Bj}. The uncorrected cross section ratio is also presented along with the SLAC fit(black) and calculations from Smirnov (blue) and Afnan *et al.* (red).

5.2.3 Cross Section Ratio for ^{3}He

Finally, we turn to the first measurement of the EMC effect on ^{3}He for $x_{Bj} > 0.4$. The results are shown in Figs. 5-13 and 5-14. The data are presented along with the only other existing measurement of the EMC effect on ^{3}He from HERMES [58], as well as Smirnov's fit, and a model prediction from Afnan *et al.* [32]. Our data are consistent with the HERMES data within the normalization uncertainties of the two experiments, though the amount of overlap in the two datasets is minimal. It should be noted that HERMES scaled their ^{3}He cross section by a factor of 1.009, after applying the proton excess correction (see page 343 in[58]), in order to better match the NMC result on ^{4}He. It should also be noted that HERMES applied a proton excess correction that used the NMC parameterization for F_2^n/F_2^p, which gives a smaller correction than does the SLAC parameterization used in our analysis. The NMC parameterization is simply a fit to the ratio of the deuterium to proton cross sections with no corrections for the Fermi motion of the nucleons in the Deuteron. The fit was

made using data for $x_{Bj} < 0.6$ and therefore is not constrained over a large portion of our data. The SLAC parameterization also extracted F_2^n/F_2^p from deuterium and proton cross sections, but the Fermi motion in deuterium were corrected for, so their result should be more accurate for the free neutron to proton ratio. The details of the isoscalar corrections are discussed below in Sec. 5.2.4. For reference, we have also included the raw cross section ratio that includes no isoscalar correction.

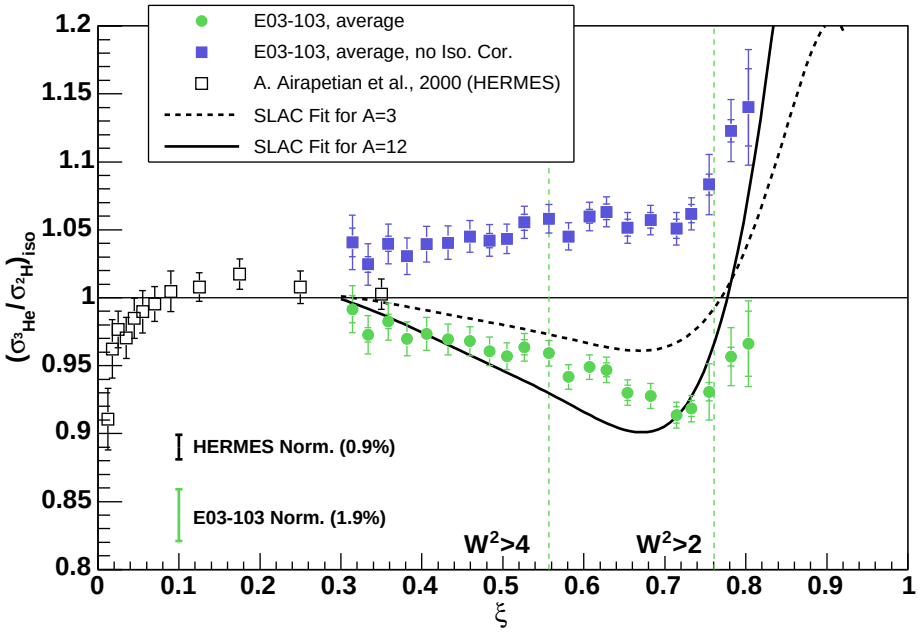

Figure 5-14: ^{3}He EMC Ratio as a function of ξ. The uncorrected cross section ratio is also presented along with the SLAC fit (black) and calculations from Smirnov (blue) and Afnan *et al.* (red).

Our data show a strong deviation from the models shown in Fig. 5-13 at $x_{Bj} > 0.7$. Both models are consistent with our data at lower x_{Bj} values. Of particular note is the fact that neither model predicts a second crossover at $x_{Bj} \approx 0.3$. These data are in agreement with those calculations and therefore with the possibility that the second crossover is absent in ^{3}He. However, given our relatively large uncertainty and limited range in that region, it is difficult to say anything conclusive. Smirnov's calculation is a fit to the world data for A$\geq$ 4. Afnan *et al.*'s calculation[32] is an explicit calculation of the EMC effect where they used the CTEQ[59] parameterization at $Q^2 = 10$ (GeV/c)^2 for the parton distributions to compute the nucleon structure

functions, then convoluted these with a realistic three-body spectral function to compute the nuclear structure function. They solved the homogeneous Faddeev equation to evaluate the spectral function to get the distribution of nucleons in the nucleus.

Our data show a minimum that is deeper than that predicted by the calculations, and also shifted to higher x_{Bj} as compared to the SLAC fit. The disagreement with the calculations is significant. The disagreement with the Afnan calculation illustrates that a convolution of the free nucleon structure functions with the momentum distribution of nucleons in the nucleus may not be sufficient for describing the nuclear structure function of three body nuclei. This is tantamount to the statement that three body nuclei exhibit different quark distributions than heavier nuclei or nuclear matter. This statement is corroborated, at least in part, but the disagreement of our data with the calculation of Smirnov, which predicts the pattern of the EMC effect from a fit constrained almost exclusively by data for A$>$ 4. It is therefore possible to state that the per-nucleon structure functions for ^{3}He is very different from both deuterium and nuclear matter. This statement must be tempered with the fact that the proton excess correction is quite large in ^{3}He. We turn now to a discussion of this correction and how it affects the uncertainty on these results.

5.2.4 Isoscalar Correction

At this stage, it is worthwhile to discuss the isoscalar correction and compare the various parameterizations for F_2^n/F_2^p in order to understand the difference they have on the proton excess correction. The isoscalar correction accounts for the relative number of protons and neutrons in different nuclei. Since the proton and neutron have different cross sections, the cross sections for nuclei with Z $\neq \frac{\mathrm{A}}{2}$ will differ significantly from those with Z $= \frac{\mathrm{A}}{2}$. In order to compare the cross section for an average nucleon, as manifested in a particular nucleus, we must correct the ratio for this proton or neutron excess. This correction constructs an isoscalar nucleus, with $\frac{\mathrm{A}}{2}$ protons and $\frac{\mathrm{A}}{2}$ neutrons, from the non-isoscalar nucleus. The isoscalar ratio is given

by the ratio of cross sections

$$\left(\frac{\sigma_{\rm A}}{\sigma_{\rm D}}\right)_{iso} = \left(\frac{\sigma_{\rm A}}{\sigma_{\rm D}}\right) \cdot \frac{\frac{1}{2}(F_2^p + F_2^n)}{\frac{1}{\rm A}({\rm Z}F_2^p + ({\rm A}-{\rm Z})F_2^n)}, \tag{5.12}$$

$$\left(\frac{\sigma_{\rm A}}{\sigma_{\rm D}}\right)_{iso} = \left(\frac{\sigma_{\rm A}}{\sigma_{\rm D}}\right) \cdot \frac{\frac{1}{2}(1 + F_2^n/F_2^p)}{\frac{1}{\rm A}({\rm Z} + ({\rm A}-{\rm Z})F_2^n/F_2^p)}. \tag{5.13}$$

The correction depends on the proton to neutron structure function ratio F_2^n/F_2^p. This ratio has been extracted from measurements of the deuteron to proton cross section ratios at SLAC [44], and by NMC [13, 21]. The two parameterizations are significantly different, as can be seen in Fig. 5-15. SLAC applied corrections to the deuterium cross section in an attempt to unsmear the extracted neutron cross section, while NMC took the direct ratio of the deuterium to proton cross sections, making no corrections for nuclear effects. Therefore, the SLAC fit is a parameterization of the free nucleon structure function ratio, and the NMC fit is a parameterization for the bound nucleon ratio. The size of the corrections for the different parameterizations of

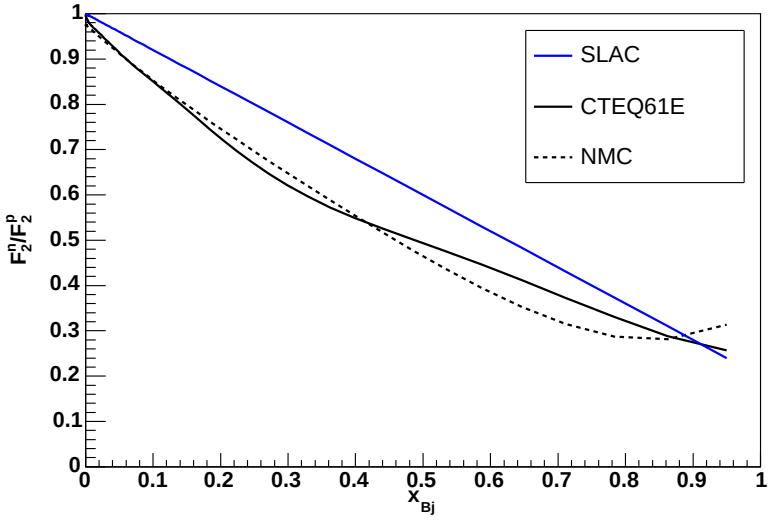

Figure 5-15: F_2^n/F_2^p Parameterizations. The SLAC fit has been corrected for Fermi motion of the nucleons in deuterium. The NMC result is for bound nucleons. The CTEQ fit is from parton distributions resulting from a global analysis of inclusive scattering data and data from other processes.

F_2^n/F_2^p for ^{3}He are shown in Fig. 5-15, along with F_2^p/F_2^n constructed from parton dis-

tributions from CTEQ[59] computed at Q^2=10 (GeV/c)^2. The parton distributions are parameterizations from global fits to inclusive scattering data. This parameterization agrees with the NMC fit, but also neglects the motion of the nucleons. In this analysis we therefore use the SLAC parameterization for F_2^p/F_2^n as it more closely represents the free nucleon value. The corrections computed from the SLAC and NMC parameterizations differ by, typically, 2-4%. We estimate a normalization uncertainty of 1.5% due to this correction. This estimate is on half of the difference between the correction from using the NMC parameterization versus using the SLAC parameterization. We take the SLAC correction as the centroid. We believe this is a conservative estimate of the uncertainty.

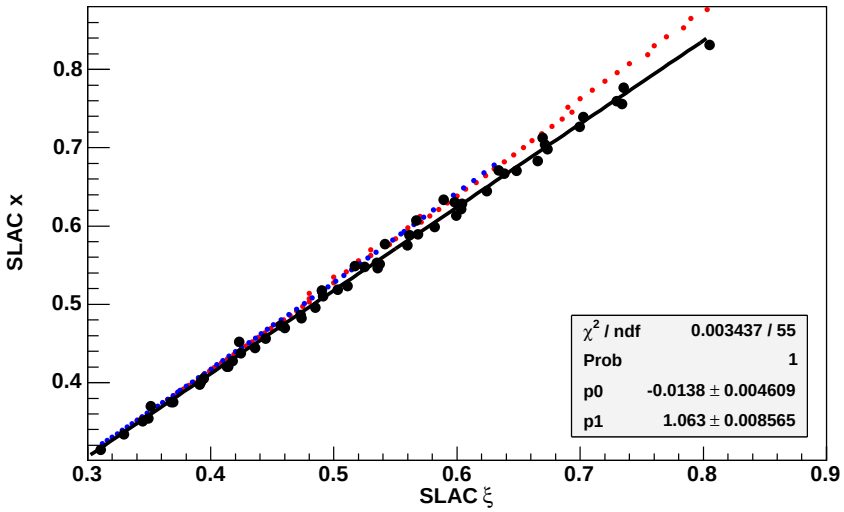

Figure 5-16: x_{Bj} vs. ξ for SLAC and XEM kinematics. The SLAC data covered a large range in Q^2, but ξ is a relatively weak function of Q^2 when Q^2 is larger than the mass of the proton squared. So the SLAC data clusters nicely about the fit line, while XEM kinematics lie slightly above the fit. This figure illustrates that $x_{Bj}(\xi)$ is different for the two experiments, and so when applying the SLAC parameterization of F_2^n/F_2^p, care must be taken to use the value at the corresponding values of x_{Bj}.

We also note that care must be taken when applying this correction as a function of ξ. The parameterizations are given as functions of x_{Bj}. In the Björken limit $\xi \to x_{Bj}$, but for any kinematics, $\xi < x_{Bj}$, and the difference between x_{Bj} and ξ depends on Q^2. Therefore, in order to compute the correction, we have fit SLAC's kinematics to derive x_{Bj} as a function of ξ in their kinematics. Since we expect scaling to hold to lower Q^2

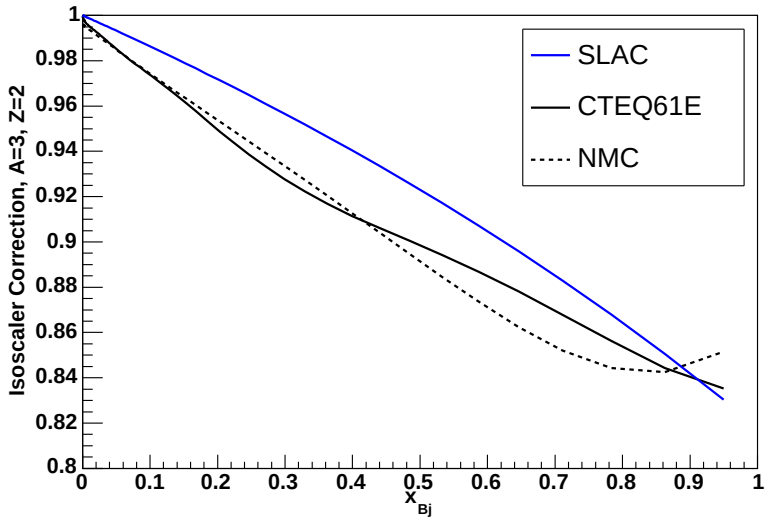

Figure 5-17: Isoscalar Correction for ^{3}He for the different parameterizations of F_2^n/F_2^p.

when the structure functions are examined as a function of ξ, we then use our ξ values to map to the corresponding x_{Bj} in the SLAC experiments, and then calculate the isoscalar correction. The dependence of x_{Bj} on ξ in the SLAC experiment is shown in Fig. 5-16. The correction factors for the various parameterizations are shown in Fig. 5-17.

5.3 Experimental Uncertainties

The uncertainties in the experiment are separated into groups based on their source and how they affect the results. Statistical uncertainties come from the counting statistics of the various yields used to compute the cross sections. In addition to counting statistics, there are several sources of systematic uncertainty which are separated into point-to-point uncertainties and normalization uncertainties. Normalization uncertainties are those uncertainties caused by global aspects of the experiment, and affect the overall scale of the cross sections, such as target thickness. Point-to-point uncertainties are due to changes in experimental conditions, either over time (run to run variations) or kinematics (changing the spectrometer from one setting to another). Most of the uncertainties have been discussed in the text, and are summa-

rized in Table 5.1. We note that the overall uncertainty on the cross section is larger than the resulting overall uncertainty on the cross section ratios. This is because there are several corrections that are made to the cross sections which cancel in the ratio, and so do not add any additional uncertainty. The data are listed in Sec. A.1 along with their statistical and systematic uncertainties.

The uncertainties in the beam energy, measured momentum and measured scattering angle result in uncertainties in the extracted cross section. The uncertainty in the beam energy measurement is discussed in detail in Sec. 3.1.1. The absolute uncertainty in the beam energy is 0.1%, and is reproducible to 0.01%. The effects of these uncertainties on the cross section were estimated by calculating the cross section at the nominal kinematics, and comparing this to the cross section when each of the kinematic variables were shifted by its uncertainty. The variation in the cross section is taken as the uncertainty in the cross section due to the uncertainty in that variable. For example, the relative uncertainty in the cross section due to the uncertainty in the beam energy is

$$\frac{\Delta\sigma(E,E',\theta)}{\sigma(E,E',\theta)} = \frac{\sigma(E+\Delta E,E',\theta)-\sigma(E,E',\theta)}{\sigma(E,E',\theta)}. \tag{5.14}$$

The largest uncertainties in the cross section ratios are due to the uncertainties in the target thicknesses and the integrated charge measurement. The thicknesses for the cryogenic targets are determined from the physical dimensions of the cryocell and the density of the cryogen. These are discussed in detail in Sec. 3.2. The uncertainty in the integrated charge is due to the stability of the BCM calibration over the course of the run and is discussed in detail in Sec. 3.1.3.

The correction for cryotarget boiling is significant for the helium targets. The uncertainty in this correction comes from the uncertainties in the fits to the carbon and cryogenic target luminosity scan data as discussed in Sec. 4.1.5. The fits to carbon and cryogenic target data are uncorrelated, so their uncertainties are added in quadrature. The total relative uncertainty in the cross section due to this correction is 0.6%. This uncertainty only applies to the cryotargets. Even though no correction

is made to the hydrogen or deuterium targets, the uncertainty in the boiling of those targets still requires that we add the uncertainty to the cross section. Therefore, the ratios of the solid target to deuterium have an additional normalization uncertainty due to the uncertainty to the boiling in deuterium.

The uncertainty in the cross section model has two distinct contributions. The first is the resulting uncertainty in the bin-centering correction, and the second is the resulting uncertainty in the radiative correction. The bin-centering uncertainty was studied by computing the cross section with our model and comparing it to the cross section computed with other models. The first was a flat cross section, and the second was a ξ-scaling model. The uncertainty due to bin-centering was estimated from the variation in the cross sections for the three models. The variation in the absolute cross section was as large as 2%, so we take this as a conservative estimate of the uncertainty in the cross section. Cross section ratios, however, showed very little variation for the different models, and so the uncertainty in the ratio is much smaller. The normalization uncertainty due to bin-centering is estimated to be 0.5% at the lowest x_{Bj} values, and has its maximum value of 2% at $x_{Bj} > 0.8$.

A similar test was done to estimate the model-uncertainty due to the radiative corrections. The DIS and QES models were independently shifted from their nominal values and the change in the radiative correction was used to estimate the model uncertainty due to radiative corrections. The iterated model agrees with the data, with fluctuations on the order of 2-3% at $x_{Bj} < 0.8$, 3-5% at $x_{Bj} > 0.8$. Shifting the cross section models results in changes in the cross sections due to the radiative corrections. The change in the cross section is most pronounced at the lowest x_{Bj} values, and the change in the ratio decreases with x_{Bj}. The shape of the x_{Bj} dependence in the cross section due to a shift in the radiative correction was fit to a third degree polynomial, and the fit function was used to compute the systematic uncertainty over the x_{Bj} and ξ range. Shifting either the quasielastic or the deep inelastic model by 3% gave a change in the cross sections of 0.4% at the lowest x_{Bj}, and 0.1% at the highest x_{Bj}. The uncertainties due to the quasielastic and deep-inelastic scattering models are added in quadrature. The uncertainties in the cross

sections must be added in quadrature when computing the uncertainty on the ratio. The point-to-point uncertainty has its maximum of 0.6% at the lowest x_{Bj}.

Finally, we have included an additional systematic uncertainty for the helium cross section ratios. It was observed that the ratios for the 40° and 50° diverged slightly at the lowest x_{Bj} values. The average discrepancy has a small, but systematic effect on the results when the data are averaged together. We therefore include a point-to-point uncertainty to account for this. The difference between the two datasets is largest at the lowest x_{Bj}, and is typically less than 2%. To estimate the uncertainty, the average was formed and compared to the results for 40° and 50° computed alone. The shift in the averaged, and re-binned, ratios was less than 1%. We have therefore assigned a point-to-point uncertainty of 1% at $x_{Bj} = 0.3$. Since the datasets, and therefore the average, converge (within statistical uncertainty), we scale this systematic uncertainty linearly by x_{Bj} such that no additional systematic uncertainty is applied at $x_{Bj} > 0.7$.

5.3.1 Ratio of Longitudinal to Transverse Cross Sections

This analysis has extracted the ratio of nuclear structure functions, F_2^{A}, using the ratios of inclusive cross sections. This procedure hinges entirely on assumption that the ratio of longitudinal to transverse cross sections, $R = \sigma_L/\sigma_T$, is independent of A. If this assumption is satisfied, then the ratio of cross sections is equivalent to the ratio of the structure functions. If not, then the structure in the cross section ratio may be due, at least in part, to the difference, $\Delta R = R_{A1} - R_{A2}$ for different nuclei, as can be seen from Eq. 2.4. The difference in the ratio for different targets have been measured over a large kinematic range and for various combinations of targets, although it has yet to be measured in the resonance region. A detailed discussion of the ratio and differences between different targets is given in [18]. Although the precision on the measurements is poor, the difference is generally found to be consistent with zero for all targets and kinematics that have been studied. Therefore, we work under the assumption that R is the same for all A, and equate the measured cross section ratios to the ratio of structure functions. Since R is poorly known, we assign an uncertainty to the ratio in order to account for a possible variation of in R with A. Since ΔR is

known to be consistent with zero to the level of 10% (that is $\Delta R = 0 \pm 0.10$), we assign an uncertainty to the structure function ratio by measuring the change in the structure function ratio for a difference in R of 10% between the two nuclei. At our kinematics a 10% change in R would change the structure function ratio by about 2.5%. Therefore, if one wishes to equate the measured cross section ratio to the structure function ratio, one should assign an additional, very conservative, overall uncertainty of 2.5%. We stress, however, that since the cross section is extracted for each target, there is no uncertainty due to R in the cross section ratios besides that built in to the uncertainty due to the choice of model and radiative corrections, and this is small.

Source	Absolute Uncertainty	Relative Uncertainty	$\delta\sigma/\sigma$ (%)	$\delta R/R$ (%) point-to-point Helium	$\delta R/R$ (%) scale Helium	$\delta R/R$ (%) point-to-point Solid	$\delta R/R$ (%) scale Solid
HMS Momentum	<0.1%	0.01%	0.2	-	-	-	-
Beam Energy	<0.1%	<0.02%	0.2	0.1	-	0.1	-
θ	0.5 mr	0.2mr	0.1	0.1	0.1	0.1	0.1
τ_{D}	0.8%	-	0.8	-	0.8	-	0.8
$\tau_{^3\mathrm{He}}$	1.5%	-	1.5	-	1.5	-	-
$\tau_{^4\mathrm{He}}$	1.0%	-	1.0	-	1.0	-	-
τ_{C}	0.5%	-	0.5	-	-	-	0.5
τ_{Be}	0.5%	-	0.5	-	-	-	0.5
τ_{Cu}	1.0%	-	1.0	-	-	-	1.0
τ_{Au}	2.0%	-	2.0	-	-	-	2.0
Charge	0.4%	0.3%	0.5	0.4	0.2	0.4	0.2
Target Boiling	0.6	-	0.5	0.3	0.6	-	0.5
Endcap Subtraction	<1.0%	0.2%	<1.0	0.1	0.1	0.1	0.1
Acceptance	1.5%	0.2%	1.5	0.2	-	0.2	-
Detector Efficiency	0.5%	0.2%	0.5	0.2	-	0.2	-
Deadtime Correction	<0.5%	0.2%	<0.5	0.1	0.1	0.1	0.1
Bin-Centering	2.0%		2.0	0.5-2.0	-	0.5-2.0	-
Radiative Corrections	2.0%	0.5%	2.0	0.3	0.4	0.3	0.4
Total			3.5-4.0	0.8-2.1	1.5-1.9	0.8-2.1	1.2-2.3
isoscalar correction	-	-	-	-	1.5	-	1.5

Table 5.1: Summary of Systematic Uncertainties. The various sources of systematic uncertainty are shown for the different targets. For the total uncertainty, the uncertainties for a each target are added in quadrature. The uncertainty due to the isoscalar correction applies only non-isoscalar (Z≠N) nuclei and is not included in the overall normalization uncertainty. This analysis assumes that the ratio of longitudinal to transverse cross sections is independent of A. For a discussion of the uncertainty on this ratio and its impact on a measurement of the structure function ratio, see Sec. 5.3.1

Chapter 6

Conclusions and Outlook

We have measured the inclusive electron scattering cross section from ^{3}He, ^{4}He and deuterium. These were used to perform the first extraction to date of the ratio of the F_2 structure function of ^{3}He to that of deuterium in the kinematic region $x_{Bj} > 0.4$. The data agree reasonably well with what little existing data there are from HERMES. The data exhibit the same general shape as observed for the ratios of structure functions in heavier nuclei, although the effect is stronger than what would be expected given the pattern seen in heavy nuclei. Also the third cross-over lies at higher x_{Bj} than all heavier nuclei. The extraction is highly dependent on the correction for proton excess, however, and this correction is currently limited by the lack of precise measurements of the ratio of the free nucleon structure functions F_2^n/F_2^p. Future measurements of the structure functions on ^{3}He and ^{3}H may yield a model independent way to extract this ratio and thus prove a valuable enhancement to the study of the EMC effect in light nuclei.

We have also performed a precise extraction of the ratio for ^{4}He and carbon. The effect in carbon has been well studied and there has been one extraction of the ratio for ^{4}He from SLAC. Our data agree well with the SLAC measurements over the entire x_{Bj} range in which they overlap. At higher x_{Bj} however, our data are much higher precision and show some deviation from the C data from SLAC and E89-008 at JLab. At high x_{Bj} the SLAC data on ^{4}He have very large error bars and in this region both data sets are consistent. Our data improve the precision in this region by a large

factor and give a fine mapping of the EMC effect in the region above $x_{Bj} = 0.7$.

There are three significant results contained in these data, each of which is more significant when viewed in light of the others. The first is the fact that the ratio of the structure functions exhibits scaling to better precision than the structure functions themselves. This is best illustrated by the carbon data. The data from Jefferson Lab had already demonstrated that the ratio of structure functions exhibited ξ-scaling [7]. Those data were taken at very low W^2, so the agreement with the DIS data from SLAC was significant when plotted versus ξ. The agreement of our data with those two data sets shows that ξ-scaling holds for the structure function ratio, but it also shows that Björken-scaling is well satisfied as well. This result is significant in that it allows the structure function ratios of Deep Inelastic Scattering to be extracted from data taken at decidedly non-DIS kinematics, giving some weight to the notion of Bloom-Gilman duality as described in Ch. 1. This result also gives us confidence in the results presented for helium.

The second notable result is that our data give the first extraction of ^{3}He at large x_{Bj}. These data, coupled with the data from HERMES at low x_{Bj} provide a complete map for the ratio of structure functions for $x_{Bj} < 0.85$. Though our data were taken at kinematics below the conventional DIS cutoffs for W^2 and Q^2, the quality of both ξ- and Björken-scaling as demonstrated by the carbon result gives us confidence that these data give access to the ratio as would be measured at higher Q^2. The EMC effect in ^{3}He appears to be as strong as the effect in ^{4}He. The effect in ^{4}He appears to be as strong as that in carbon.

This is the third significant result: the per-nucleon structure functions for both ^{3}He and ^{4}He are very different from both deuterium and heavy nuclei. This statement says that there are effects present in few body nuclei that are not present in deuterium, and also that the features of nuclear structure that are useful for describing the pattern of the EMC effect for heavy nuclei are not sufficient to account for the effect in few body nuclei. That is, the fact that the effect exhibits a pattern of nucleon number dependence, or density dependence seems not to hold for few body nuclei. This could be an indication that there are features of the nuclear force that first

appear in few body nuclei that aren't present in deuterium, but which saturate for heavy nuclei. However, it is clear that few body nuclei are interesting in that their underlying structure is different from that of nuclear matter. And this should serve as motivation for making further measurements of the EMC effect in light nuclei in order to understand the effect itself, but also to make more precise measurements of the structure of the few body nuclei themselves.

6.1 Outlook

There is much to be excited about regarding the understanding of the nuclear structure functions. The extraction presented here adds what, we hope, will provide valuable clues to several long-standing puzzles in the field. In particular, E03-103 has measured the EMC effect in the resonance region which will provide (in a separate analysis) more detailed information about the quality of x_{Bj} and ξ scaling of the structure functions and their ratios in this region for both heavy and light targets. In this analysis we have made the first study of the EMC effect in ^{3}He and improved the precision of the extraction of the effect in ^{4}He. These data will prove invaluable in the study of the evolution of the EMC effect, which has suffered from the lack of data for A<4 nuclei [31].

As important as the study of the EMC effect on ^{3}He is, it is important to keep in mind that it depends, critically, on the parameterization of F_2^n/F_2^p. ^{3}He is the most proton-rich nucleus and therefore requires a very large correction, on the order of 10%, for proton excess. Thus the study of the evolution of the structure functions from the lightest nuclei would benefit greatly from improved data on the free nucleon structure function ratio F_2^n/F_2^p. A novel method for extracting this ratio has been suggested by [60] using complementary measurements of the structure function ratios in both ^{3}He and ^{3}H. The ratio of structure function ratios can be formed and F_2^n/F_2^p can be extracted from this ratio. Because isospin symmetry is well respected in nuclei, the difference in the nuclear effects are expected to be small, allowing for a cleaner extraction from this method than the standard method which is via the ratio

of deuterium to proton cross sections. There is currently a proposal to perform this experiment at Jefferson Lab as part of the 12 $(\mathrm{GeV/c})^2$ program.

Finally, we note that there is also interest in studying the polarized EMC effect as discussed in [33], which would give information on the ratio of the *spin* structure functions g_{1p}^A/g_{1p}. It is our hope that the data presented herein will provide an important link between earlier measurements of the EMC effect on heavy nuclei and the next stage of novel, precision measurements of the effect in light nuclei.

Appendix A

Collected Results

This appendix collects together some of the results not included in the text. This includes the structure functions and cross sections for all targets, as well as data tables for the cross section ratios presented in Ch. 5.

A.1 Structure Functions

The structure functions for all targets are shown below. The solid lines denote the position of the quasielastic peak, and the dashed lines indicate the position of the Δ resonance ($W^2 = 1232$ MeV^2). The Q^2 values listed in the legends indicate the Q^2 value at $x_{Bj} = 0.6$. For more discussion on the scaling properties of the structure function versus x_{Bj} and ξ, please see Sec. 5.1.

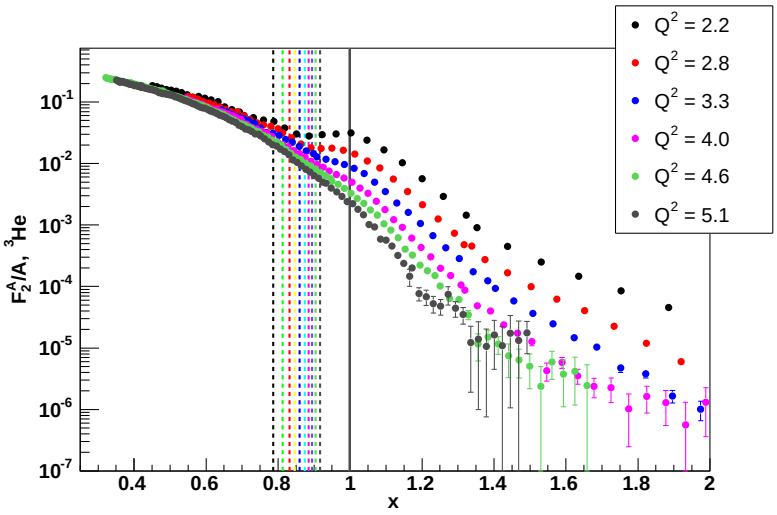

Figure A-1: Structure function per nucleon, $F_2^{\mathrm{A}}/\mathrm{A}$, for ^{3}He versus x_{Bj}.

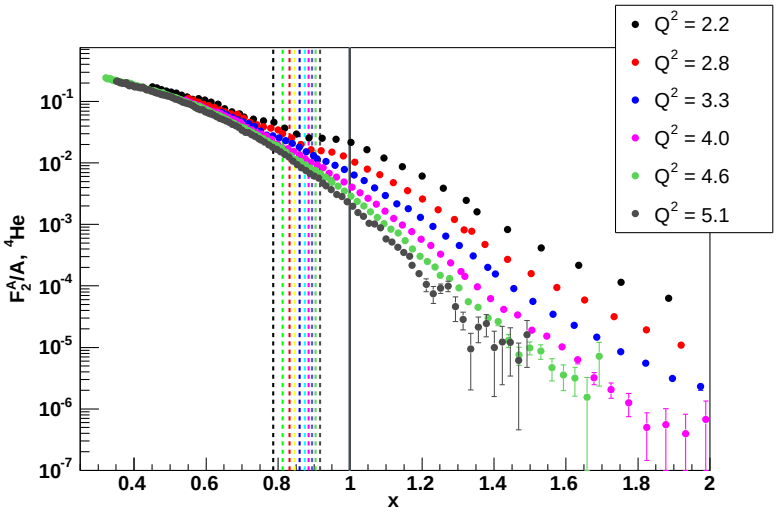

Figure A-2: Structure function per nucleon, $F_2^{\mathrm{A}}/\mathrm{A}$, for ^{4}He versus x_{Bj}.

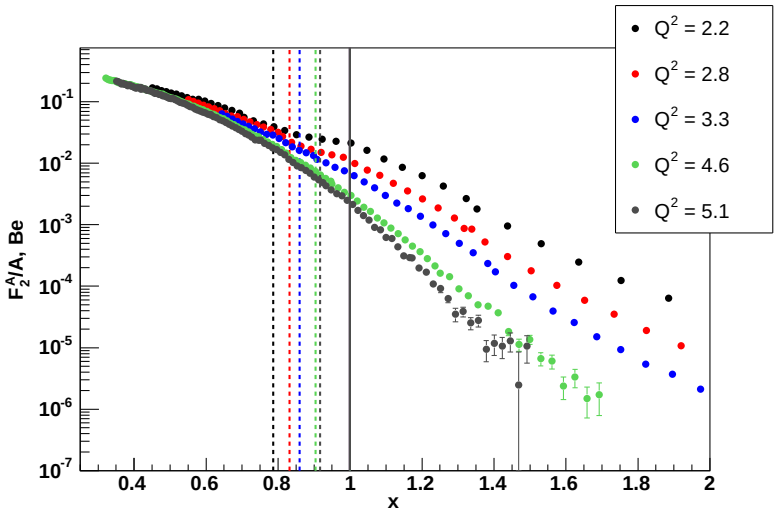

Figure A-3: Structure function per nucleon, $F_2^{\mathrm{A}}/\mathrm{A}$, for Be versus x_{Bj}.

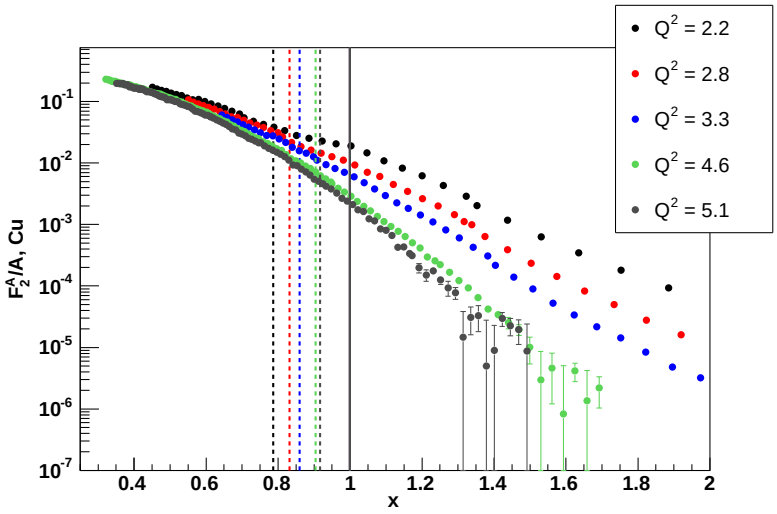

Figure A-4: Structure function per nucleon, $F_2^{\mathrm{A}}/\mathrm{A}$, for Cu versus x_{Bj}.

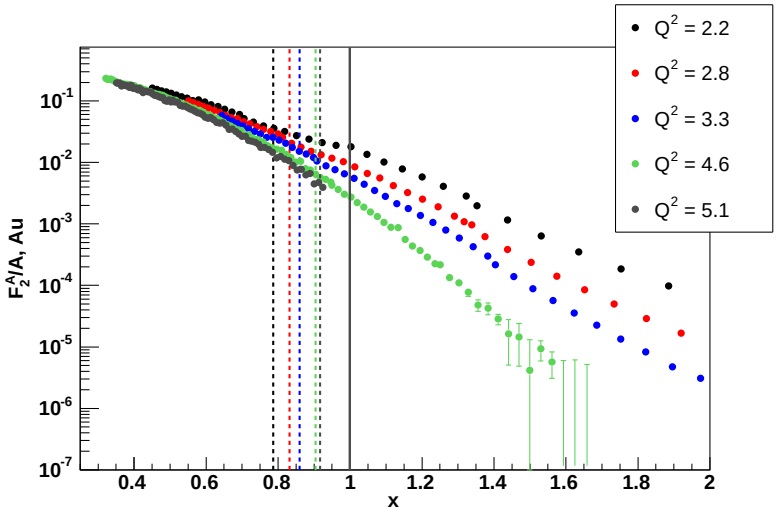

Figure A-5: Structure function per nucleon, $F_2^{\mathrm{A}}/\mathrm{A}$, for Au versus x_{Bj}.

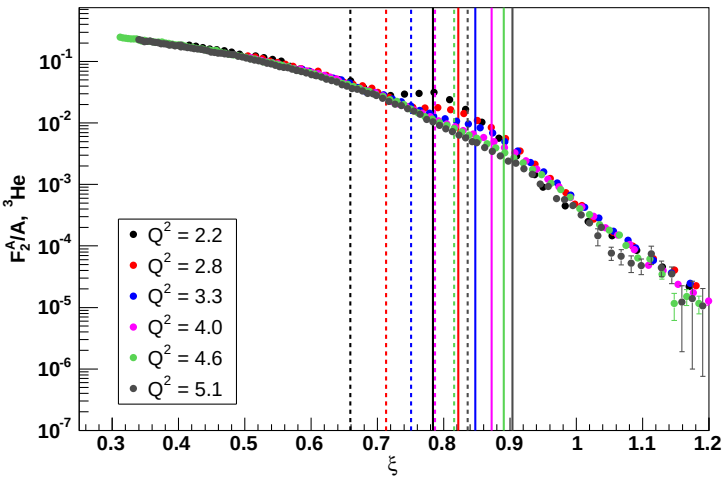

Figure A-6: Structure function per nucleon, $F_2^{\mathrm{A}}/\mathrm{A}$, for ^{3}He versus ξ.

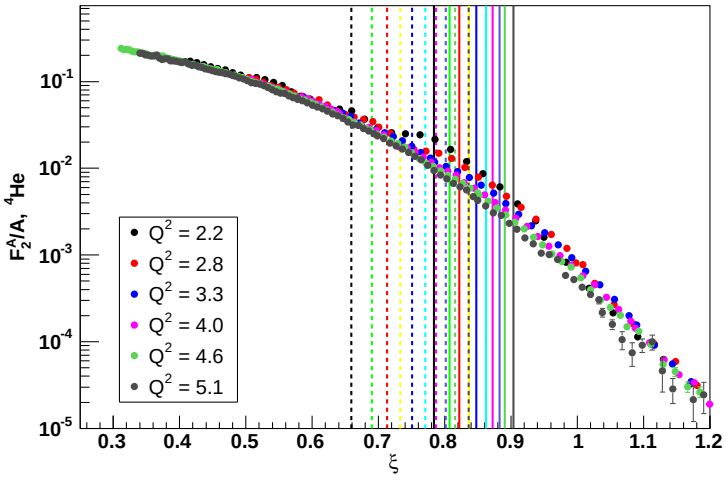

Figure A-7: Structure function per nucleon, $F_2^{\mathrm{A}}/\mathrm{A}$, for ^{4}He versus ξ.

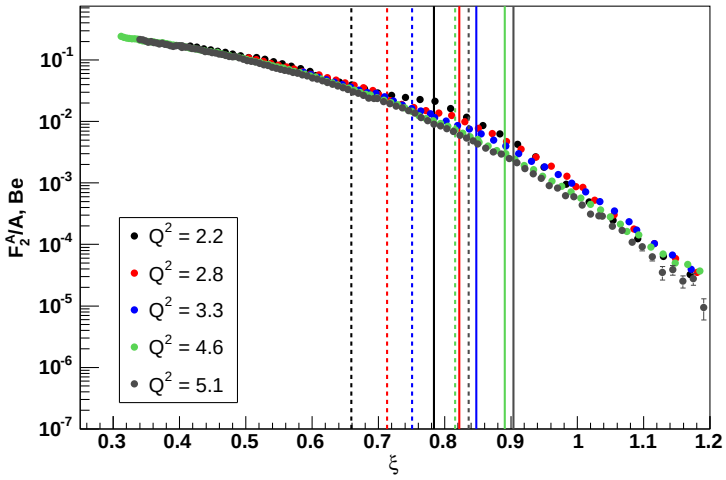

Figure A-8: Structure function per nucleon, $F_2^{\mathrm{A}}/\mathrm{A}$, for Be versus ξ.

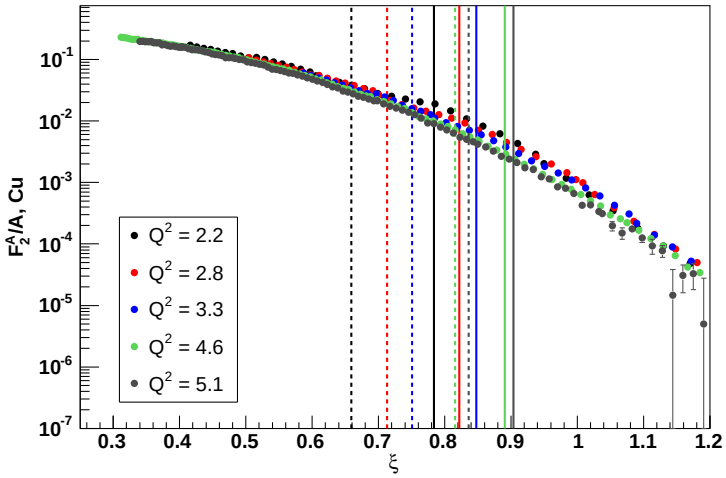

Figure A-9: Structure function per nucleon, $F_2^{\mathrm{A}}/\mathrm{A}$, for Cu versus ξ.

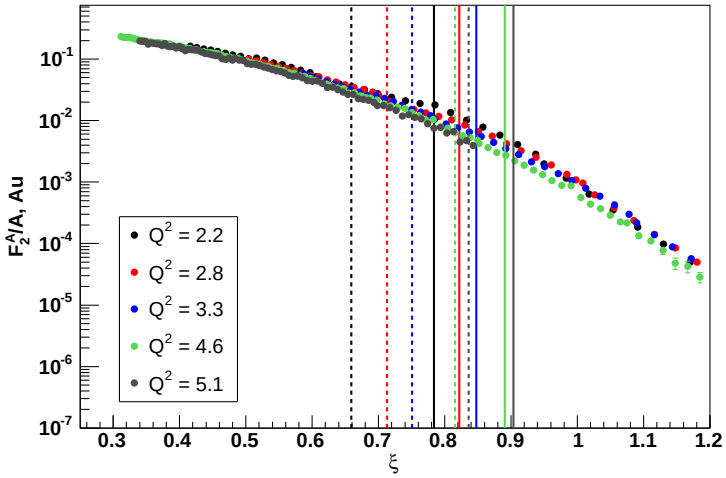

Figure A-10: Structure function per nucleon, $F_2^{\mathrm{A}}/\mathrm{A}$, for Au versus ξ.

A.2 Cross Section Ratio Data

The cross section ratios were presented in Ch. 5. The data for the helium and carbon results are listed in the tables below. The tables include the statistical and point-to-point systematic uncertainties. The normalization uncertainties are listed in the captions for each target. The values for x_{Bj}, ξ, and the ratios represent the statistics-

weighted average over the different Q^2 settings.

x_{Bj}	R	δR_{stat}	δR_{ptp}
0.332	1.015	0.005	0.012
0.359	1.007	0.005	0.011
0.384	0.987	0.005	0.010
0.407	0.983	0.004	0.010
0.431	0.967	0.005	0.010
0.456	0.973	0.004	0.009
0.484	0.954	0.004	0.009
0.507	0.954	0.004	0.009
0.532	0.937	0.004	0.009
0.557	0.933	0.004	0.009
0.583	0.937	0.005	0.009
0.606	0.916	0.005	0.009
0.632	0.918	0.005	0.009
0.654	0.918	0.005	0.009
0.682	0.911	0.005	0.009
0.708	0.910	0.005	0.009
0.733	0.897	0.006	0.010
0.753	0.903	0.005	0.009
0.778	0.912	0.006	0.010
0.802	0.938	0.006	0.021
0.836	1.012	0.013	0.025
0.856	1.056	0.009	0.024
0.879	1.109	0.015	0.028

Table A.1: Cross Section ratio data for carbon versus x_{Bj}. The relative normalization uncertainty of 1.2% is not shown in the table.

ξ	R	δR_{stat}	δR_{ptp}
0.324	1.025	0.008	0.014
0.344	1.007	0.004	0.011
0.372	1.001	0.004	0.011
0.397	0.982	0.004	0.010
0.422	0.975	0.004	0.010
0.450	0.973	0.004	0.009
0.481	0.955	0.004	0.009
0.507	0.954	0.004	0.009
0.532	0.937	0.004	0.009
0.560	0.934	0.004	0.009
0.592	0.927	0.004	0.009
0.619	0.919	0.004	0.009
0.647	0.918	0.004	0.009
0.679	0.912	0.005	0.009
0.706	0.908	0.005	0.009
0.738	0.897	0.005	0.009
0.767	0.909	0.005	0.009
0.799	0.936	0.006	0.010
0.825	0.982	0.010	0.023
0.860	1.066	0.008	0.024
0.882	1.108	0.023	0.033

Table A.2: Cross Section ratio data for carbon versus ξ. The relative normalization uncertainty of 1.2% is not shown in the table.

x_{Bj}	R	δR_{stat}	δR_{ptp}
0.332	0.988	0.006	0.015
0.360	0.975	0.005	0.014
0.384	0.970	0.005	0.013
0.407	0.959	0.004	0.012
0.431	0.953	0.005	0.012
0.456	0.956	0.005	0.011
0.484	0.953	0.005	0.011
0.508	0.944	0.005	0.010
0.531	0.935	0.004	0.010
0.560	0.941	0.005	0.010
0.586	0.933	0.004	0.009
0.607	0.920	0.004	0.009
0.628	0.915	0.005	0.009
0.659	0.921	0.005	0.009
0.682	0.919	0.005	0.009
0.708	0.907	0.005	0.009
0.731	0.909	0.009	0.011
0.753	0.892	0.005	0.009
0.778	0.898	0.005	0.009
0.806	0.926	0.006	0.020
0.829	0.969	0.008	0.022
0.854	1.009	0.010	0.024
0.880	1.014	0.015	0.026

Table A.3: Cross Section ratio data for ^{4}He versus x_{Bj}. The relative normalization uncertainty of 1.5% is not shown in the table.

ξ	R	δR_{stat}	δR_{ptp}
0.324	0.996	0.010	0.017
0.343	0.979	0.005	0.014
0.371	0.980	0.005	0.013
0.396	0.959	0.005	0.012
0.423	0.955	0.004	0.012
0.451	0.956	0.005	0.011
0.483	0.953	0.005	0.011
0.508	0.944	0.005	0.010
0.531	0.935	0.004	0.010
0.563	0.940	0.005	0.010
0.592	0.931	0.004	0.009
0.619	0.917	0.004	0.009
0.650	0.920	0.006	0.009
0.676	0.918	0.004	0.009
0.706	0.908	0.004	0.009
0.739	0.897	0.006	0.009
0.767	0.894	0.004	0.008
0.798	0.925	0.006	0.010
0.819	0.946	0.007	0.021
0.856	1.009	0.008	0.023
0.889	1.002	0.028	0.035

Table A.4: Cross Section ratio data for ^{4}He versus ξ. The relative normalization uncertainty of 1.5% is not shown in the table.

x_{Bj}	R^{iso}	δR^{iso}_{stat}	δR^{iso}_{ptp}	R^{raw}	δR^{raw}_{stat}	δR^{raw}_{ptp}	c_{iso}
0.330	0.979	0.006	0.015	1.028	0.007	0.016	0.952
0.359	0.984	0.005	0.014	1.039	0.005	0.015	0.947
0.384	0.969	0.005	0.013	1.027	0.006	0.014	0.943
0.407	0.973	0.004	0.012	1.036	0.005	0.013	0.939
0.431	0.972	0.006	0.012	1.040	0.006	0.014	0.935
0.457	0.969	0.005	0.011	1.042	0.005	0.012	0.931
0.484	0.968	0.005	0.011	1.046	0.005	0.012	0.926
0.508	0.960	0.005	0.011	1.042	0.005	0.012	0.922
0.532	0.957	0.004	0.010	1.043	0.005	0.011	0.917
0.557	0.963	0.005	0.010	1.056	0.006	0.012	0.913
0.587	0.957	0.005	0.010	1.055	0.006	0.011	0.907
0.607	0.949	0.005	0.009	1.051	0.005	0.011	0.903
0.630	0.945	0.005	0.009	1.051	0.005	0.011	0.899
0.657	0.945	0.004	0.009	1.057	0.005	0.010	0.894
0.680	0.946	0.006	0.010	1.064	0.007	0.012	0.889
0.706	0.932	0.006	0.010	1.054	0.007	0.012	0.884
0.733	0.925	0.006	0.010	1.053	0.007	0.012	0.879
0.746	0.932	0.008	0.011	1.064	0.009	0.014	0.876
0.778	0.911	0.006	0.009	1.048	0.006	0.011	0.869
0.802	0.920	0.006	0.020	1.064	0.007	0.021	0.864
0.831	0.935	0.007	0.021	1.090	0.008	0.022	0.858
0.856	0.961	0.008	0.022	1.128	0.010	0.024	0.852
0.876	0.975	0.014	0.025	1.150	0.017	0.030	0.848

Table A.5: Cross Section ratio data for ^{3}He versus x_{Bj}. The relative normalization uncertainty of 1.9% is not shown in the table.

ξ	R^{iso}	δR^{iso}_{stat}	δR^{iso}_{ptp}	R^{raw}	δR^{raw}_{stat}	δR^{raw}_{ptp}	c_{iso}
0.324	0.992	0.010	0.017	1.041	0.010	0.020	0.953
0.345	0.973	0.005	0.014	1.024	0.006	0.015	0.949
0.372	0.982	0.005	0.014	1.040	0.006	0.015	0.945
0.397	0.970	0.005	0.013	1.031	0.005	0.013	0.941
0.423	0.973	0.005	0.012	1.039	0.005	0.013	0.936
0.452	0.969	0.005	0.011	1.041	0.005	0.012	0.932
0.482	0.968	0.004	0.011	1.045	0.005	0.012	0.926
0.508	0.960	0.005	0.011	1.042	0.005	0.012	0.922
0.532	0.957	0.004	0.010	1.043	0.005	0.011	0.917
0.557	0.964	0.005	0.010	1.056	0.006	0.012	0.913
0.592	0.959	0.004	0.009	1.058	0.005	0.011	0.906
0.619	0.942	0.004	0.009	1.045	0.005	0.010	0.901
0.649	0.949	0.005	0.009	1.060	0.005	0.010	0.895
0.673	0.947	0.005	0.009	1.063	0.006	0.011	0.891
0.703	0.930	0.005	0.009	1.051	0.006	0.011	0.885
0.738	0.928	0.005	0.009	1.057	0.006	0.011	0.878
0.776	0.914	0.006	0.010	1.051	0.007	0.012	0.869
0.798	0.918	0.006	0.010	1.062	0.007	0.012	0.865
0.824	0.931	0.007	0.021	1.083	0.008	0.022	0.859
0.857	0.957	0.007	0.021	1.123	0.008	0.023	0.852
0.877	0.966	0.024	0.032	1.140	0.028	0.042	0.847

Table A.6: Cross Section ratio data for ^{3}He versus ξ. The relative normalization uncertainty of 1.9% is not shown in the table. The uncertainty in the isoscaler correction gives an additional systematic uncertainty of 1.5% for the isoscalar corrected ratio. The isoscalar correction is given in the last column as c_{iso}.

A.3 Shifting Calorimeter Gain

A.3.1 What's the problem?

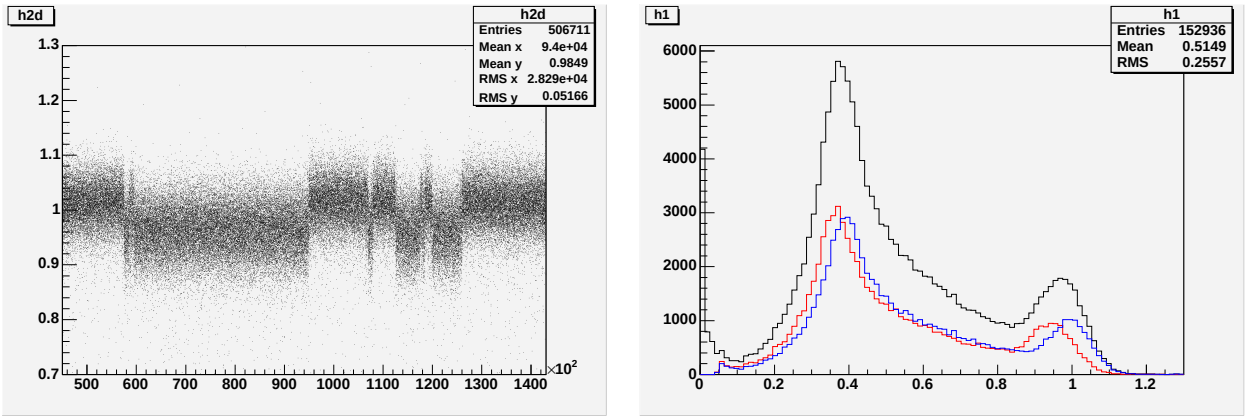

Figure A-11: The left panel shows HSSHTRK vs. EVENTID for the ^{3}He runs at 40°*and*1.33 GeV, and the right panel shows the HSSHTRK peaks for the different peak positions. The events shown in the right plot are from run 51572, which was taken at 50° and 0.86 GeV.

The problem is that the HSSHTRK peak shifts over time as shown in figure A-11. This shift is a problem because HSSHTRK is used to separate electrons from pions that survive the Čerenkov and acceptance cuts. For a given cut, a shifting peak may cause electrons to be excluded, or pions to be included, relative to the number that would have been counted if the peak was stationary at the nominal value of 1. The right panel in figure A-11 shows the HSSHTRK peak for a subset of events from run 51572. The blue histogram shows a set of events for which the HSSHTRK peak is located at the nominal position, and the red histogram shows a set of events where the HSSHTRK peak is shifted about 5% below the nominal position. The black histogram is the sum of the red and blue histograms, and there are about the same number of entries in the blue and red histograms. Besides shifting the overall HSSTHRK peak to smaller values, this shift of course also widens the peak, increasing the effective calorimeter energy resolution (as given by the width of the HSSHTRK peak) beyond the intrinsic value given by the width of either the red or blue electron peaks. Note also that the π peak (located at HSSHTRK$\approx$ 0.4) is not shifted quite as much as the

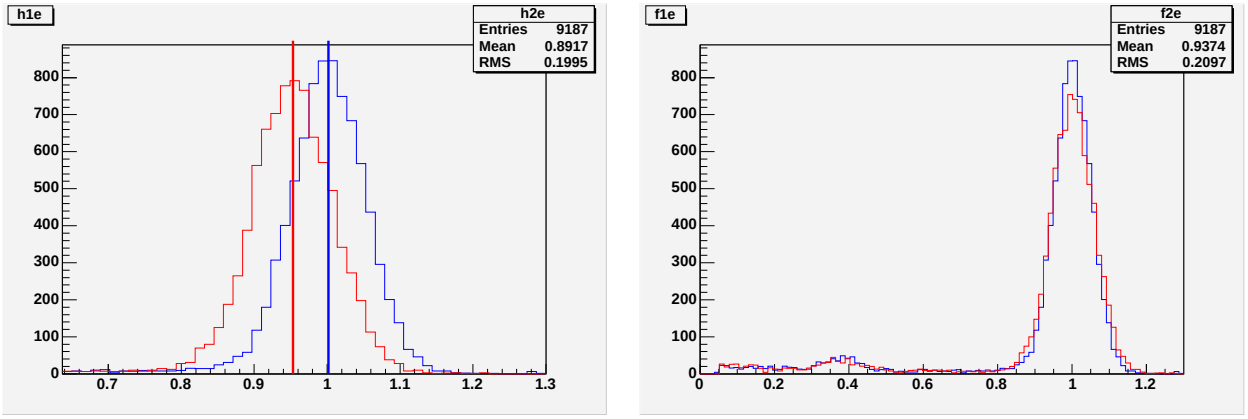

Figure A-12: Uncorrected and corrected electron peaks. The panel on the left shows the two HSSHTRK peak positions. The peak positions give $\delta = 0.0512$. The right panel shows the result of the correction given in equation A.1. Note that the corrected peak (red) is normalized to the nominal peak (blue). Cuts were placed on trigger type (ELREAL) and the Čerenkov in order to get a clean sample of electrons.

electron peak. This is an indication that the shift is due to a change in the overall gain of the calorimeter, and not something like a pedestal shift, which would move all bins by the same amount.

Given that the shift in HSSHTRK was due to a change in the overall gain of the calorimeter, it was found that the shift could be corrected by scaling HSSHTRK:

$$h' = h(1 + \delta), \tag{A.1}$$

where h is the uncorrected HSSHTRK value, and δ is given by the deviation of the mean from the nominal position (see figure A-12):

$$\delta = \frac{\mu_{nominal}}{\mu_{shifted}} - 1. \tag{A.2}$$

This type of correction was effective for both the electron peak and the pion background (see figures A-12 and A-13). Using only one scale factor (given by the electron peak position), the entire spectrum can be corrected. This correction gets the electron peak position correct by construction, but also gets the π peak position and shap correct.

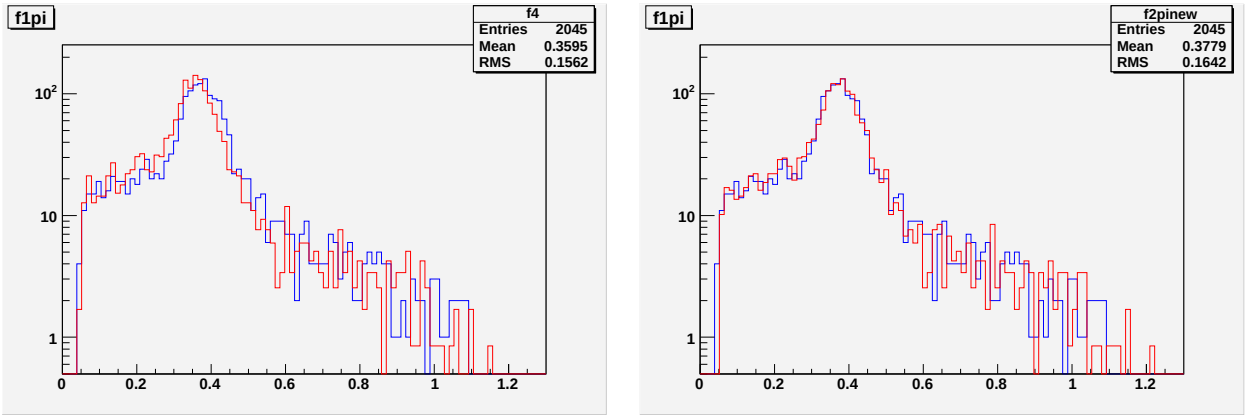

Figure A-13: Uncorrected and corrected pion peaks. The panel on the left shows the two HSSHTRK peaks before correcting, and the right panel shows the result of the correction given in equation A.1. Note that the corrected peak (red) is normalized to the nominal peak (blue). No particle ID cuts were used to make this plot, and PIPRE was required in order to select an unbiased sample of events.

Since it is possible to correct the data with a simple scale factor as described above, it is also possible to un-correct the data using the same model. That is, we can use that model to convert events at the nominal position to events at any shifted position. This allows us to count the number of events that would lie within our cuts for the nominal set of events and use it as a comparison to the number that pass the cuts when those same events are shifted. The difference in these two samples should give us a good idea of the size of effect the shift causes, and since we're using the same set of events for both samples, it should be independent of statistical fluctuations if the study were done with different event samples.

A.3.2 Procedure

I prepared a set of events at the nominal HSSHTRK position. The sample was a subset of events from run #51572. This run was taken at $p_{HMS} = -0.86, \theta_{HMS} = 50°$, which is the setting with the highest π/e ratio (see figures A-15, and the largest (worst) intrinsic calorimeter resolution (see figure A-16). The sample of events used for the study is shown in figure A-14. In all of the work reported below, events were required to be within the acceptance of the detector: $|\delta| < 9, |x'_{tar}| < 0.08$, and $|y'_{tar}| < 0.04$;

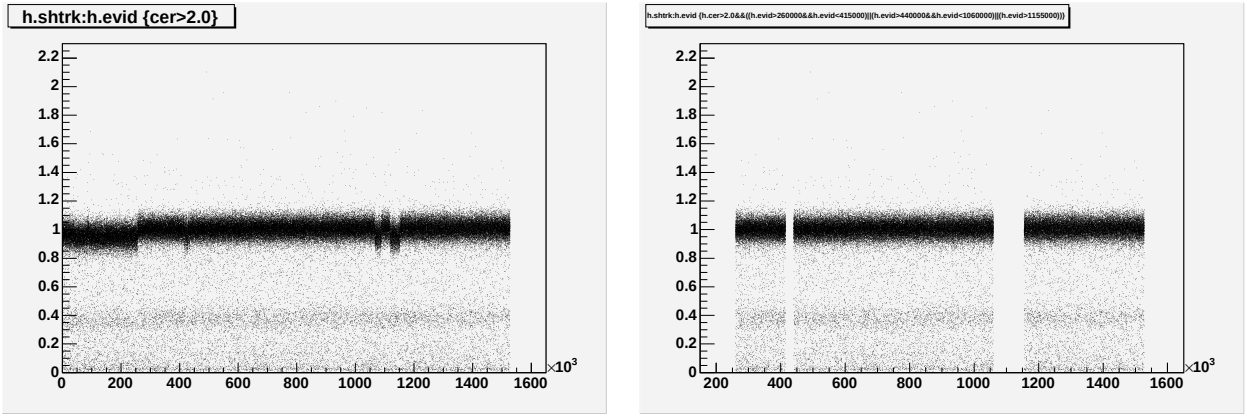

Figure A-14: HSSHTRK vs. EVENTID for run 51572. The left panel shows all events and the right panel shows the set of events used in this study.

and electrons were selected by requiring: HCER_NPE> 2.

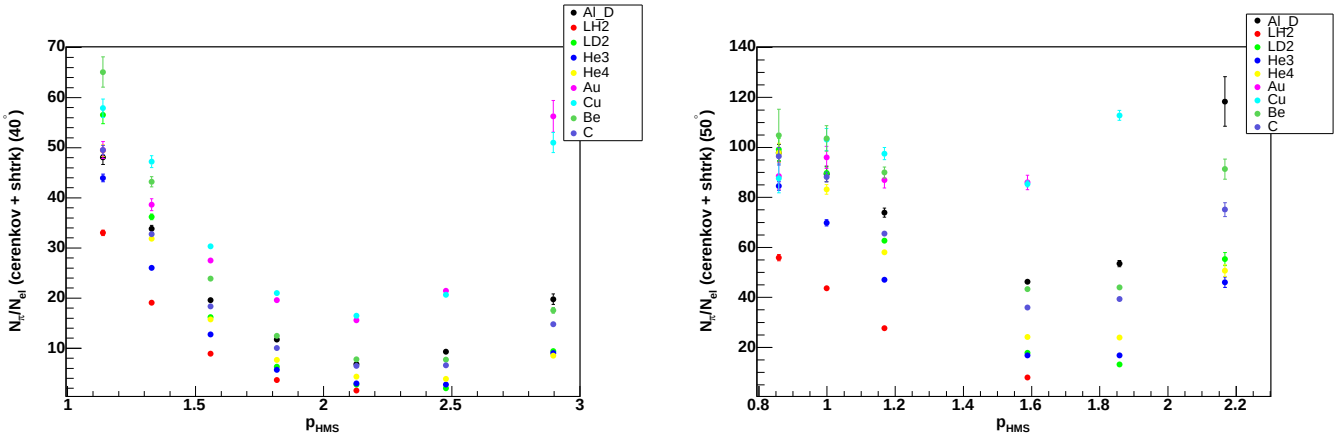

Figure A-15: π to e ratios at 40° and 50°. Note that for the left panel, $p_{\mathrm{HMS}} > 2.37$GeV corresponds to $x_{Bj} > 1$ and for the left panel $p_{\mathrm{HMS}} > 1.81$GeV corresponds to $x_{Bj} > 1$. At these high momentum settings there are very few electron events.

Once the events were selected, the number of events passing an HSSHTRK cut were counted for various peak positions from $\mu' = 0.9$ to $\mu_{\prime} = 1.1$ and compared to the number of events that pass the same cut for $\mu' = \mu$ (the nominal peak position). This procedure was done for several different HSSHTRK cuts. The number of interest is the relative difference between the shifted-peak yield and the nominal-peak yield:

$$\Delta = \frac{Y_{shifted} - Y_{nominal}}{Y_{nominal}}. \tag{A.3}$$

Two different types of cuts were applied: symmetric and asymmetric. By 'symmetric'

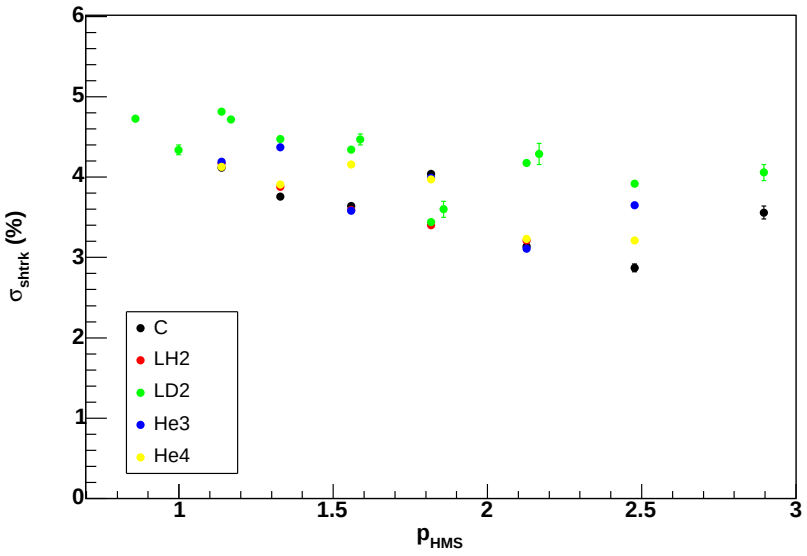

Figure A-16: Calorimeter resolution vs. HMS central momentum for the light targets at 40 and 50 degrees. Note that at the two highest momentum settings there were very few electrons available with which to measure the resolution (these settings correspond to $x_{Bj} > 1$). These last points should be treated with care. The rest of the data roughly follow the expected shape for resolution: $\sigma^2 = a + b/p_{HMS} + c/E^2 + ...$, though there is some dependence on scattering angle and target material.

I really just mean:

$$h_{lo} < h' < h_{hi}, \tag{A.4}$$

and by 'asymmetric' I just mean

$$h_{lo} < h'. \tag{A.5}$$

A symmetric cut will likely be used in the analysis, and gives the overall result caused by the peak shift. The asymmetric case shows what part of the total effect is due to the low HSSHTRK cut, where we may either exclude electrons (if the peak shifts to smaller values) or include pions (if the peak shifts to higher values) relative to the nominal case.

A.3.3 Results and Discussion

The results of this study are shown in figures A-17- A-18. The main feature to note is that the symmetric cuts with low edges at 0.7, 0.75 and 0.8 result in a Δ on the

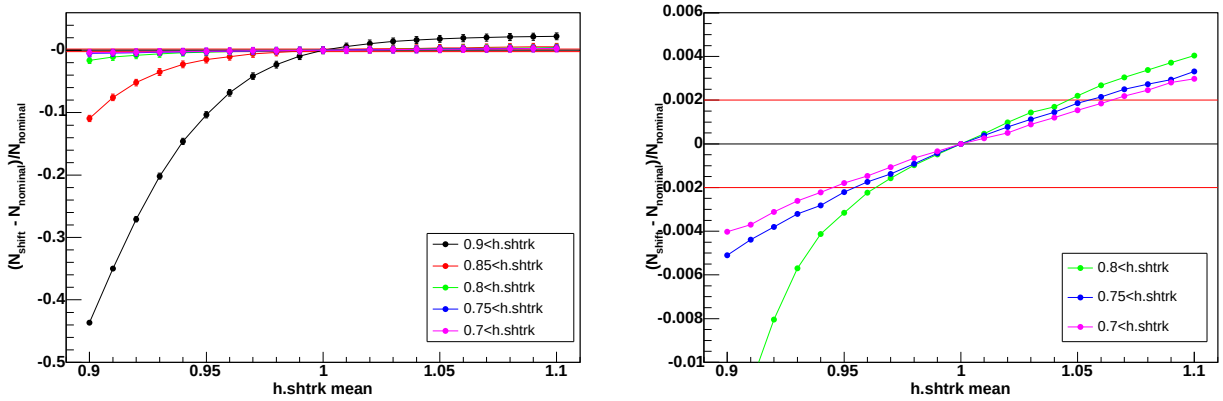

Figure A-17: Results of shifting peak using the asymmetric cut (low calorimeter cut only.) The error bars in the left plot are $\approx 0.5\%$, and have been suppressed for clarity in the right plot.

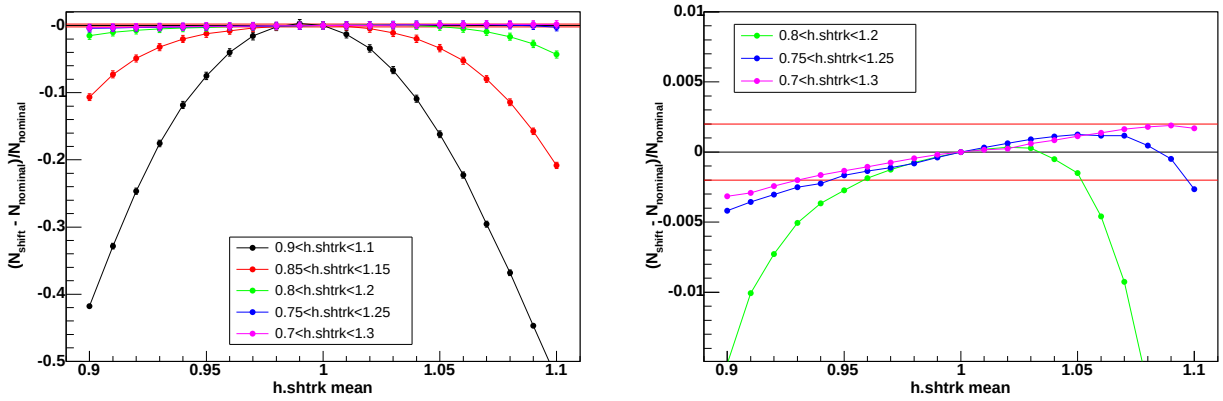

Figure A-18: Results of shifting peak using the symmetric cut (high and low calorimeter cuts.) The error bars in the left plot are $\approx 0.5\%$, and have been suppressed for clarity in the right plot.

order of 0.2% out to peak positions of $\pm 5\%$. Figure A-19 shows the high and low peak positions, within a run, as a function of run number. Note that the high position of the HSSHTRK peak is rarely greaer than 1.05, and the low position of the peak is very rarely below 0.95. Furthermore, since the symmetric cut is somewhat antisymmetric about the nominal peak position, if there are two peak positions, one above and one below the nominal position, they will partially offset each other.

From these results it would be resonable to conclude that any miscount in the total yield would be within $\pm 0.2\%$. It should be noted, however, that this result assumed that the entire sample of events for a given setting was shifted, In fact, there

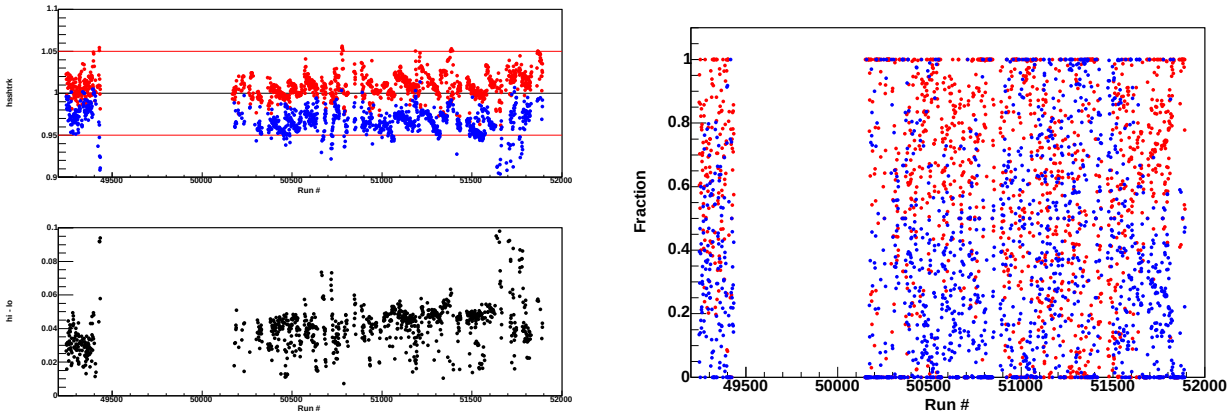

Figure A-19: The left panel shows the Positions of high and low peak positions (top), and the difference between those peaks (bottom). The left plot shows the fractions of time spent at the high and low positions.

is usually a mix of events at the high and low positions, and so the results presented in figures A-17- A-18 may be regarded as an upper limit. We can go further by calculating the error based on the amount of time spent at the shifted position. Figure A-19 shows that the time spent at the high and low positions is roughly equal. The actual numbers (over the course of the entire running period) are: 60% high, and 40% low (calculated by counting the number of bins at the each position, divided by the total number of bins over the all runs. This calculation assumes that there are only two discrete levels between which the gain jumps.) So, on average, only about half of the events in a run, or at a given setting, will be shifted[1]. The size of the miscount depends directly on the fraction of events that occur in the shifted peak:

$$\Delta_{real} = f\Delta_{Max}, \tag{A.6}$$

where Δ_{Max} is the value in figures A-17-A-18. If half the events are normally at the nominal position, and half of the events are at the shifted position, then we can expect that the actual miscount will be $(1/2)0.2\% = 0.1\%$ Of course, this feature

[1]This is not exactly correct. Both sets of events as being shifted from the nominal value. So in principle, each peak will miscount. But typically one peak is closer to the nominal position of 1, and the other is farther away. The peak that is the furthest away is no more than 5% from 1. So the two peaks will most likely miscount different amounts, with the added bonus that if the two peaks stradle HSSHTRK= 1, they will partially cancel each other.

relies heavily on the global behavior of the effect of the shift. For a given setting, or a given run, this argument may not hold.

Bibliography

[1] J.J. Aubert et al. *Physics Letters*, 123B:275, 1983.

[2] T.W. Donnelly. *Modern Topics in Electron Scattering.* 1990.

[3] E.D. Bloom et al. *Phys. Rev. Let.*, 123B:930, 1969.

[4] M. Breidenbach et al. *Phys. Rev. Let.*, 23:935, 1969.

[5] S. Eidelman et al. Review of particle physics. *Physics Letters B*, 592:1+, 2004.

[6] L.Y. Zhu et al. *Phys. Rev. C*, 71:044603, 2005.

[7] J. Arrington et al. *Phys. Rev. C*, 73:035205, 2006.

[8] E. Bloom and F. Gilman. *Phys. Rev. D*, 4:2901, 1971.

[9] M.A. Dewitt and S. Jeschonnek. *Quarks, Hadrons, and Nuclei Proceedings of the Sixteenth and Seventeenth Annual HUGS at Jefferson Lab Summer School.* World Scientific, 2004.

[10] A. De Rújula, Howard Georgi, and H. David Politzer. *Annals of Physics*, 103:315, 1977.

[11] O. Nachtmann. *Nuc. Phys. B*, 63:237, 1973.

[12] I. Niculescu et al. *Phys. Rev. Let.*, 85:1186, 2000.

[13] M. Arneodo et al. *Nuc. Phys. B*, 364:107, 1995.

[14] J. Ashman et al. *Physics Letters B*, 202:603, 1988.

[15] J. Gomez et al. *Phys. Rev. D*, 49:4348, 1994.

[16] G. Bari et al. *Physics Letters*, 163B:282, 1985.

[17] S.J. Brodsky, F.E. Close, and J.F. Gunion. *Phys. Rev. D*, 6:177, 1972.

[18] D.F. Geesaman, K. Saito, and A.W. Thomas. *Annu. Rev. Nucl. Part. Sci.*, 45:337, 1995.

[19] P.R. Norton. *Rep. Prog. Phys.*, 66:1253, 2003.

[20] M. Arneodo et al. *Physics Letters B*, 211:493, 1988.

[21] M. Arneodo et al. *Nuc. Phys. B*, 487:3, 1997.

[22] A. Bodek et al. *Phys. Rev. Let.*, 50:1431, 1983.

[23] A. Bodek et al. *Phys. Rev. Let.*, 51:534, 1983.

[24] D.O. Caldwell et al. *Phys. Rev. Let.*, 42:553, 1979.

[25] S. Dasu et al. *Phys. Rev. Let.*, 60:2591, 1988.

[26] A. Airapetian et al. *hep-ex/0210068*, 2002.

[27] J. Arrington et al. *Phys. Rev. C*, 53:2248, 1996.

[28] P.P. Alport et al. *Phys. Let. B*, 232:417, 1989.

[29] M.R. Adams et al. *Phys. Rev. Let.*, 69:1026, 1992.

[30] O. Benhar, V.R. Pandharipande, and I.Sick. *Phys. Lett. B*, 410:79, 1997.

[31] G.I. Smirnov. *Eur. Phys. J. C*, 10:239, 1999.

[32] I.R. Afnan et al. *Phys. Rev. C*, 68:035201, 2003.

[33] I.C. Clöet, W. Bentz, and A.W. Thomas. *nucl-th/0504019*, 410:79, 1997.

[34] J.R. Arrington. PhD thesis, California Institute of Technology, 1998.

[35] D.J. Gaskell. PhD thesis, Oregon State University, 2001.

[36] C. Yan, R. Carlini, and D. Neuffer. *CEBAF-PR-93-004*.

[37] D. Meekins. *Hall C internal report*.

[38] T. Horn. PhD thesis, University of Maryland, 2006.

[39] C.S. Armstrong. PhD thesis, The College of William and Mary in Virginia, 1998.

[40] J. Volmer. PhD thesis, Vrije Universiteit Amsterdam, 2000.

[41] W.R. Leo. *Techniques for Nuclear and Particle Physics Experiments: A How-to Approach*. Springer-Verlag, second revised edition edition, 1994.

[42] L.W. Whitlow et al. *Phys. Lett. B*, 250:193, 1990.

[43] O. Benhar, S. Fantoni, G.I. Lykasov, and N.V. Slavin. *Phys. Rev. C*, 57:1532, 1997.

[44] A. Bodek et al. *Phys. Rev. D*, 20:1471, 1979.

[45] D. Day and I. Sick. *Phys. Rev. C*, 69:028501, 2004.

[46] S. Stein et al. *Phys. Rev. D*, 12:1884, 1975.

[47] Y.S. Tsai. *SLAC-PUB-848*, 1971.

[48] L.W. Mo and Y.S. Tsai. *Rev. Mod. Phys.*, 41:205, 1969.

[49] A. Aste and J. Jourdan. *nucl-th/0403075*, 2004.

[50] A. Aste, C. von Arx, and D. Trautmann. *nucl-th/0502074*, 2005.

[51] M. Traini. *Nucl. Phys. A*, 694:325, 2001.

[52] K.S. Kim, L.E. Wright, Yanhe Jin, and D.W. Kosik. *Phys. Rev. C*, 54:2515, 1996.

[53] Howard Georgi and H. David Politzer. *Phys. Rev. Lett.*, 36:1281, 1976.

[54] H. Georgi and H.D. Politzer. *Phys. Rev. Lett.*, 37:68, 1976.

[55] L.W. Whitlow et al. *Phys. Lett. B*, 282:475, 1992.

[56] B. Povh, K. Rith, Ch. Scholz, and F. Zetsche. *Particles and Nuclei, An Introduction to the Physical Concepts.* Springer Berlin, 1995.

[57] J.R. Arrington. *Personal Communication.*

[58] A. Airapetian et al. *Phys. Let. B*, 567, 2003.

[59] H.L. Lai et al. *Eur. Phys. J. C*, 12, 2000.

[60] I.R. Afnan et al. *Phys. Lett. B*, 493:36, 2000.